UNIVERSITY OF OKLAHOMA

GRADUATE COLLEGE

INTEGRATED ROLE OF THE URBAN CANOPY ON TURBULENT TRANSFER WITH THE ROUGHNESS SUB-LAYER FROM OBSERVATIONS

A DISSERTATION

SUBMITTED TO THE GRADUATE FACULTY

in partial fulfillment of the requirements for the

Degree of

DOCTOR OF PHILOSOPHY

By

JOSE MANUEL GALVEZ
Norman, Oklahoma
2011

INTEGRATED ROLE OF THE URBAN CANOPY ON TURBULENT TRANSFER WITH THE ROUGHNESS SUB-LAYER: AN OBSERVATIONAL POINT OF VIEW

A DISSERTATION APPROVED FOR THE
SCHOOL OF METEOROLOGY

BY

Dr. Petra Klein, Chair

Dr. Michael Douglas

Dr. Evgeni Fedorovich

Dr. Alan Shapiro

Dr. David Stensrud

Dr. May Yuan

ACKNOWLEDGEMENTS

This work would had not been possible without Petra Klein. I want to acknowledge her excellence as a scientist, teacher, advisor, and friend. These qualities were essential to help me through this learning process. This work was also possible thanks to NSF, via Petra Klein's Career Award ILREUM. I also would like to thank my committee members: Evgeni Fedorovich, Alan Shapiro, Michael Douglas, David Stensrud and May Yuan for their help, patience and detailed revisions targeted to attain the best quality document as possible in the given timeframe. Many thanks to Brian Bridges, Matt Carney and especially Sean Arms for their help but mostly for what I learned from them as scientists and as regular human beings. Great people, great team! Celia and Marcia, you are such great and wise people, and so helpful professionally but also emotionally. Finally I would like to thank all my family for their unconditional support from afar, and those that supported me from nearby: my friends (in random order) Alex, Ricardo, Marisol, Maria, Ellie, Hamish, Melissa, Paulina, David, Wara, Vagner, Daniel, Marcia, Zehra, Jelena, Magdalena, Danny, Dustin, Fabiola, Bryan, Sofia, Alex S., Matt, Melissa, and many, many more that it would take too long to mention. You made this period of my life more than memorable. I will miss you guys! Be always positive, never stop learning and stay true friends forever!

TABLE OF CONTENTS

LIST OF TABLES

LIST OF EQUATIONS

LIST OF FIGURES

LIST OF VARIABLES AND PARAMETERS

A Constant that relates the structure parameters of temperature and refractive index fluctuations over short path lengths ~ 7.887×10^{-1} KPa^{-1}.

A_f Canopy area density for a given model layer.

bw Building width.

C Transfer coefficient.

C_d Drag coefficient for the urban canopy.

C_p Specific heat at constant pressure ~ 1004 J kg^{-1} K^{-1}.

C_n^2 Structure parameter of refractive index fluctuations.

C_T^2 Structure parameter of temperature fluctuations.

C_X^2 Structure parameter of the fluctuations of variable X.

D_X Average of X measurement differences squared.

D Scintillometer aperture diameter.

d Distance between the laser beams in bichromatic scintillometers.

d_0 Zero-plane displacement height.

E Latent heat flux.

f_{urb} Fraction of urban area in each grid cell of the domain.

G Heat flux into the ground.

g Gravitational acceleration ~ 9.8 ms^{-1}.

H Vertical sensible heat flux in the natural coordinate system.

H_K Vertical component of the kinematic flux of heat in the natural coordinate system.

H_{SLS} Scintillometer sensible heat flux.

H_x Zonal component of sensible heat flux.

H_y Meridional component of sensible heat flux.

H_z Vertical component of sensible heat flux.

h Height of the urban canopy.

k Spatial wave number.

k_o Optical wave number.

L Monin-Obukhov length.

L_r Length of the recirculation region inside a canyon.

l_0 Inner scale of turbulence.

M Momentum flux.

M_{SLS} Scintillometer momentum flux.

m Mass.

n Refractive index of air.

Pr Prandtl Number.

P_L Scintillometer path length.

Q_H Sensible heat in [J K^{-1}].

Ri	Richardson number.
R_d	Gas constant for dry air ~ 287 J Kg^{-1} K^{-1}.
R_n	Net radiation.
R_{nc}	Net radiation over urban canyons.
R_{nr}	Net radiation over roofs.
r	Distance between simultaneous measurements.
r_H	Resistance to the transport of heat.
T	Temperature.
U	Velocity vector.
$\bar{U}$	Mean velocity vector.
u	Zonal velocity.
$\bar{u}$	Mean zonal velocity.
u'	Zonal velocity perturbation.
u_R	Along-flow velocity in the natural coordinate system.
$\bar{u}_R$	Mean along-flow velocity in the natural coordinate system.
${u_R}'$	Along-flow velocity perturbation in the natural coordinate system.
u_*	Friction velocity, the surface layer scale for velocity fluctuations.
v	Meridional velocity.
$\bar{v}$	Mean meridional velocity.
v'	Meridional velocity perturbation.
v_R	Normal velocity in the natural coordinate system.
$\bar{v}_R$	Mean normal velocity in the natural coordinate system.
${v_R}'$	Normal velocity perturbation in the natural coordinate system.
W	Canyon width.
w	Vertical velocity.
$\bar{w}$	Mean vertical velocity.
w'	Vertical velocity perturbation.
w_R	Vertical velocity in the natural coordinate system.
w_R	Mean vertical velocity in the natural coordinate system.
${w_R}'$	Vertical velocity perturbation in the natural coordinate system.
X	Random variable.
x	Spatial coordinate.
z	Height above ground.
z_{BL}	Boundary-Layer depth.
z'	Adjusted height above the RSL.
z_{0H}	Roughness length for heat.
z_{0m}	Roughness length for momentum.
Z_F	Fresnel zone radius.
β	Bowen ratio or ratio between latent heat flux and sensible heat flux.
β_1	Obukhov-Corrsin constant ~ 0.86.

ΔH_S	Heat storage term.
ε	Dissipation rate of turbulence kinetic energy.
ζ	Dimensionless height.
η_K	Kolmogorov microscale.
θ	Potential temperature.
θ'	Potential temperature perturbation.
$\bar{\theta}$	Mean potential temperature.
θ_*	Friction temperature.
κ	Von Kármán constant ~ 0.4 .
Λ	Ratio of the storage heat flux in urban structures ~ 0.4.
λ	Optical wavelength.
ν	Kinematic viscosity of air.
ρ	Density of air.
τ	Averaging times for sonic anemometer data in.
$\varphi_{C_T^2}$	Universal function for the structure parameter of temperature.
φ_ε	Universal function for the dissipation of turbulence kinetic energy.
ϕ_n	Universal function for the three-dimensional spectrum of refractive index of air.

ABSTRACT

About 50% of the world population nowadays lives in urban areas. With the fast growing trends of urbanization, understanding meteorological processes in such environments is rapidly gaining importance. A complex process that still needs thorough investigation is turbulent transfer of sensible heat across the urban canopy and the roughness sub-layer. It is particularly important to understand how individual sections of the canopy contribute to its integrated role. In an attempt to address this problem, sonic anemometer and scintillometer measurements were organized in three field campaigns. The first two were designed to evaluate and calibrate the scintillometer. The third and core campaign consisted of a one-year-long experiment carried out in an urban environment. The campaign was prolonged to address temporal representativeness issues present from the briefness of previous campaigns. Spatial representativeness was addressed with scintillometer measurements since they represent path-integrated quantities.

A limitation of scintillometers is their dependence on Monin-Obukhov Similarity Theory, which does not apply in heterogeneous surfaces and non stationary flows. Studies have yet showed good agreement between scintillometer and sonic anemometer sensible heat fluxes over complex environments, attained by modifying empirical coefficients to approximate Monin-Obukhov Similarity quantities. Although this was attempted, it was found that correcting errors in the measurement of the inner scale of turbulence and the structure function of refractive index fluctuations produced much better results. Corrective expressions were thus proposed and the applicability of scintillometers over the highly complex urban environment was then explored.

Urban campaign results revealed several complex interactions present inside the urban canopy. The distribution of sensible heat fluxes was found to exhibit high three-dimensional complexity, and to be mostly regulated by surface properties and their interaction with solar radiation, local advection and turbulent mixing. Sensible heat fluxes in the RSL decrease across street canyons during periods of stronger mixing with low-momentum and low-sensible heat flux in-canyon air.

Scintillometers were found skillful for measuring turbulent heat fluxes over the canopy but only for some wind directions. Problems were identified when measurements were placed within the wake of large roughness elements, which suggest that under some wind directions the measurements were made too close to the surface. Yet, scintillometer measurements in the urban environment depend on a large number of corrections. From these, the most critical is the determination of an appropriate value of zero-plane displacement height, which needs to be considered to account for flow modification by the roughness elements. The dependence on a large number of factors and limitations on the determination of appropriate values of zero-plane displacement height suggest that at this point in time scintillometer measurements made that close to the canopy should be considered with care.

1. INTRODUCTION

This study focuses on two different topics relevant to the field of Boundary-Layer Meteorology. The first one is the role of the urban canopy on the turbulent transfer (TT) of heat in the urban roughness sub-layer (URSL). The second topic explores the reliability of small aperture scintillometers (SAS) as means to measure TT inside the URSL. Scintillometers are instruments that measure variations in the intensity of electromagnetic radiation produced by turbulence in a fluid. In the surface layer (SL), the lowest portion of the atmosphere, they can be used to measure turbulent fluxes of heat and momentum using Monin-Obukhov Similarity (MOS), a theory that allows to express key SL atmospheric variables as functions of dimensionless height. Although MOS was established under the assumptions of homogeneity and stationarity, data measured over heterogeneous surfaces suggest that it can still be applied under certain weather conditions with the aid of corrective expressions. The study thus focuses on TT in the URSL and on the reliability of a SAS in such heterogeneous environment.

The approach was based on observations of sensible heat fluxes and other relevant variables, and was made possible by Petra Klein's NSF Career Award ILREUM: "Innovative Laboratory for the Research and Education in Urban Meteorology" (NSF Proposal 6500235). The measurements were organized in three field campaigns where sensible heat fluxes were measured with a SAS and several sonic anemometers (SA). The first two campaigns were conducted over flat and homogeneous terrain (i.e. where MOS can be considered valid) to evaluate SAS data. Two sets of empirical corrections were proposed based on the evaluation. Once applied to the SAS data, very good agreement with the SA measurements was attained.

The third and core campaign focused on SAS and SA measurements made in two urban street-canyon. The campaign lasted thirteen months to account for temporal representativeness. The SAS was operated over rooftops and across two canyons. The SA (13 instruments) were operated over rooftops and inside the canyon. SA data served as reference measurements and to map the three-dimensional distribution of TT in the urban canopy and in the lowest part of the URSL.

1.1. Motivation.

About 50% of the world population lived in urban areas by 2009. This number was even larger for developed countries and approached 75%. The United Nations (2009) suggested that these percentages were increasing rapidly due to a fast urbanization trend observed during the last six decades (Figure 1.1).

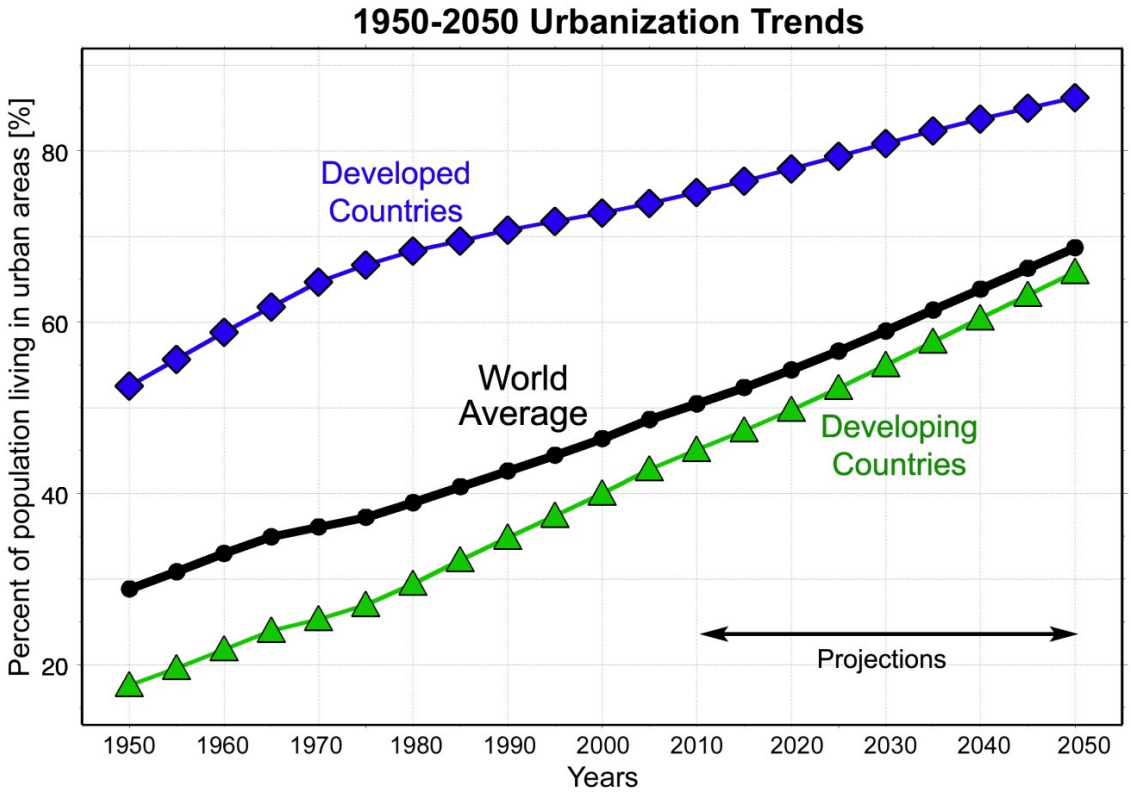

Figure 1.1. 1950-2050 urbanization trends plotted with data provided by the United Nations (2009).

These projections suggest that more people will be likely moving into urban areas during the coming decades and that by 2050 about 70% of the world population will live in such environments. This number approaches 85% for developed countries only. Based on these trends, understanding, simulating and forecasting meteorological processes in urban environments is rapidly gaining importance. The knowledge about urban meteorology is, however, still limited. This is particularly true in the context of TT inside and above the urban canopy, where the number of studies available is small and limited in terms of spatial and temporal representativeness.

Most of the research on TT in the atmospheric boundary-layer has focused over ideal (i.e. flat and homogeneous) terrain located away from urban areas mostly due to limitations associated with the measurements and the collapse of ideal assumptions derived for flat and homogeneous environments. Measurement complications arise from the high cost of instrumentation designed for the measurement of turbulence; limitations on instrument deployment due to complex infrastructures and required permissions from authorities; spatial representativeness limitations due to the large three-dimensional heterogeneity of the urban environment; and the collapse of some simplifying assumptions such as MOS (Barlow and Coceal, 2009). As a result, only a small number of studies have explored TT in the URSL, and most of them have been conducted over periods in the order of only a few weeks. Some examples can be found in Roth and Oke (1993a,b), Rotach (1993, 1995), Oikawa and Meng (1995), Louka et al. (1998, 2000), Feigenwinter et al. (1999, 2005), Grimmond et al. (2004), Longley et al. (2004), Christen (2005), Dobre et al. (2005), Boddy et al. (2005), Eliasson et al. (2006), Kanda et al. (2006), Moriwaki and Kanda (2006), Roth et al. (2006), Christen et al. (2007), Klein and Clark (2007) and Offerle et al. (2007).

But why is this important? Understanding TT in the URSL has applications into several fields, in particular Boundary-Layer Meteorology, Microscale and Mesoscale Meteorology, Urban Meteorology, Air Quality and Scintillometry. The results are discussed primarily in the context of Microscale Meteorology that focuses on scales smaller than two kilometers (Glickman, 2000). They also address means to improve the Harman-Barlow-Belcher model for scalar fluxes from Urban Street Canyons (Harman et al., 2004). Related studies have shown significant positive impacts on model output when urban parameterizations are improved, especially when resolutions tend toward finer mesoscales. Some examples of successful model output improvement from urban parameterizations are available in Uno et al. (1989), Kusaka et al. (2001), Otte et al. (2004) and Dupont and Mestayer (2004, 2006).

The impact of urban areas on mesoscales is sometimes questioned. In the horizontal, mesoscales range from a few to several hundred kilometers (Glickman, 2000). Urban environments are usually perceived as small when viewed from a mesoscale perspective. Is placing efforts on improving the representation of this very small fraction of the surface worthwhile? The answer is yes. Urban areas modify the atmosphere above them and across non-negligible three-dimensional regions located downwind. This is not only important in the context of mesoscale meteorology but in the context of air quality forecasting as well. Air quality at mesoscales is often studied with mesoscale models due to the high non-linearity of the system. Moreover, pollutants emitted in urban areas usually interact with air masses in the mesoscale, where secondary pollutants are formed and dispersed (Martilli et al., 2002). An example is the formation of tropospheric ozone O_3 from nitrogen oxides NOx, carbon monoxide CO and volatile organic compounds VOCs emitted, for the most part, in urban environments. These compounds are exposed

to a series of chemical reactions in which sunlight becomes important, and can lead to high levels of tropospheric ozone in areas sometimes located hundreds of kilometers away. Improving the understanding of TT in urban areas has thus important applications in mesoscale air quality studies as well, aside from those in the fields of urban meteorology and climatology themselves.

The general goals of the study are thus (1) to improve the understanding of TT across the urban canopy and in the lower part of the URSL via observations and validation of the Harman-Barlow-Belcher parameterization; and (2) to explore the reliability of SAS measurements in the URSL. There is a special interest on describing how individual sections of the urban canopy contribute to its integrated role. The analysis was oriented to improve the understanding of the interactions between urban scales, i.e. those in the order of tenths of meters; and small mesoscales, those in the order of a few kilometers; and to provide a background to improve their representation in mesoscale models. They were also targeted to provide a means for future studies to infer the integrated role of the urban canopy based on sparse measurements, which is generally the norm to sample the highly three-dimensionally complex urban atmosphere.

1.2. Dissertation structure.

The dissertation is structured in eight chapters. Chapter 2 introduces essential concepts relevant to the study, discusses current research issues and the approach considered to address them. A general description of the atmospheric boundary layer is first presented, followed by the introduction of important concepts such as sensible heat fluxes, the eddy covariance approach and MOS, amongst other relevant notions. Scintillometers are then discussed with emphasis on the theory behind turbulent flux

calculations from scintillations. The urban boundary layer is then addressed, followed by an introduction to efforts conducted to represent it numerically. The ILREUM project is then addressed, followed by the set of open questions investigated and by the approach and rationale selected to address them.

Chapter 3 discusses the instrumentation used during the ILREUM campaigns, and focuses on sonic anemometers, the scintillometer and the Norman MESONET site.

Chapter 4 focuses on the suburban campaigns. The procedures followed to evaluate scintillometer skill and the empirical corrections needed to attain good agreement with sonic anemometer measurements are described.

Chapter 5 discusses the set up of the ILREUM urban campaign (IUC). The analysis procedures to attain reliability of scintillometer data are described.

Chapter 6 highlights important findings of the IUC. The general characteristics of the flow are first addressed, followed by analysis of sensible heat fluxes. Interesting cases under different reference wind directions are selected, with emphasis on cases measured under southerly flow, the most common wind direction in Central Oklahoma. A more general analysis is then presented, with emphasis on data stratification upon different wind directions, wind speeds and solar radiation regimes.

Chapter 7 provides the summary and conclusions of the dissertation.

2. BACKGROUND, CURRENT ISSUES AND APPROACH.

2.1. The Atmospheric Boundary Layer.

Section 2.1 summarizes overviews of the atmospheric boundary layer (ABL) documented by Oke (1987), Garratt (1992), Kaimal and Finnigan (1994), Arya (1999), Stull (2000), Glickman (2000), Wallace and Hobbs (2006) and Stensrud (2007). A general description of the ABL is first addressed followed by an introduction to sensible heat fluxes, the eddy covariance approach and Monin-Obukhov Similarity theory, a key consideration for the representation of processes in the atmospheric surface layer and for scintillometry.

2.1.1. General description.

The ABL is the lowest part of the troposphere, adjacent to the surface of the earth. ABL flow is highly controlled by the effects of the surface, which are felt directly in timescales of an hour or less. The ABL is dominated by turbulence generated by both thermal (i.e. buoyancy) and mechanical processes (i.e. wind shear). Turbulent fluxes are thus important, and are essential to describe the connection between the surface and the rest of the troposphere or free atmosphere, typically characterized by less turbulence and stable stratification. The TT of sensible heat is of particular interest and will be addressed with more detail in section 2.1.2.

The ABL can be subdivided into several layers. To illustrate this classification, a schematic cross section of the standard daytime atmosphere has been constructed based on Garratt (1992) and Kaimal and Finnigan (1994) and is presented in Figure 2.1. It shows the vertical structure and characteristic thickness of the troposphere, the free troposphere, the ABL, the mixed layer, the surface layer, the inertial sub-layer and the

roughness sub-layer. Height above ground z is indicated in meters and using a logarithmic scale. A few typical features such as roughness elements (i.e. pasture in this case) and an ABL-deep thermal and associated cloud are also indicated. The depth of the ABL z_{BL}, and is generally in the order of one to two kilometers, but can vary largely. The depth of the SL is about one tenth of that of the ABL and the depth of the roughness sub-layer is larger than the roughness length z_0, defined as the height above ground where the mean wind speed becomes zero (Glickman, 2000).

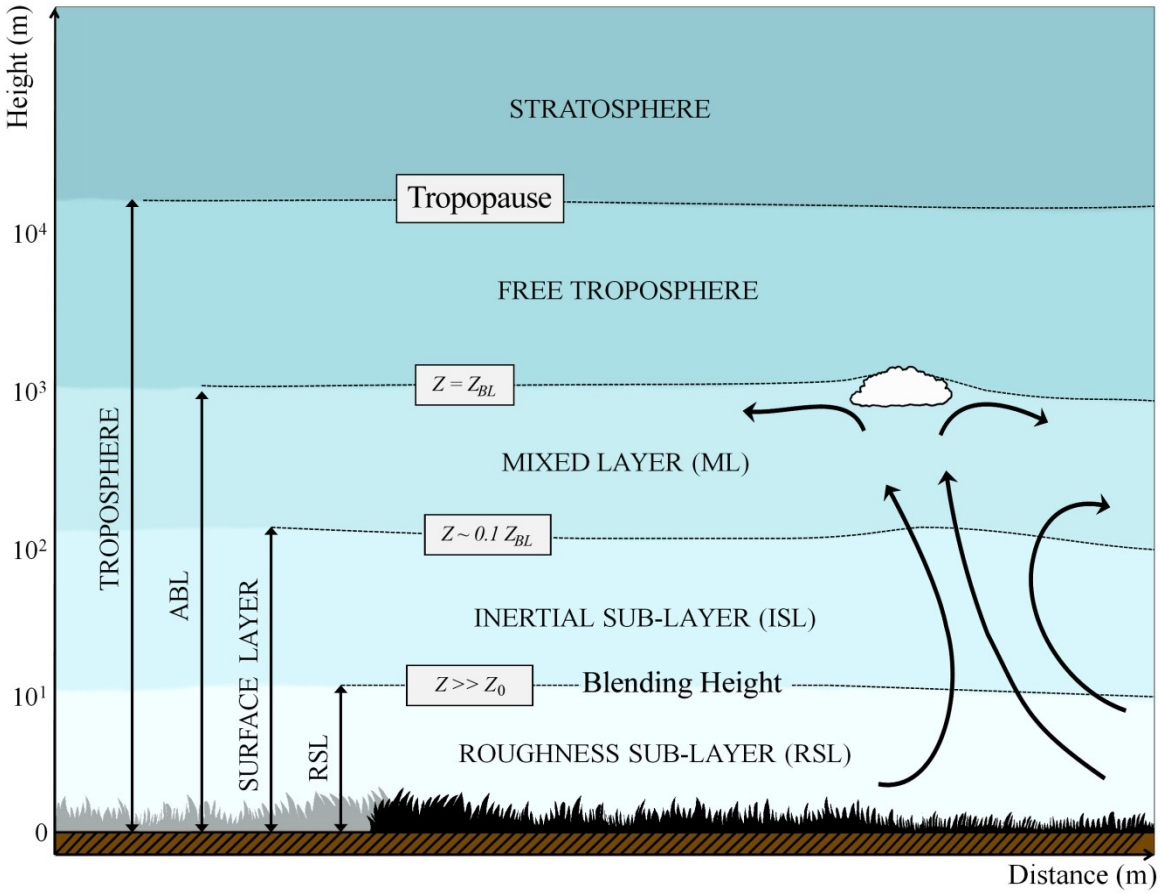

Figure 2.1. Components of the ABL constructed based on Garratt (1992) and Kaimal and Finnigan (1994).

The ABL can be subdivided into two layers: an outer and an inner layer. The outer layer is referred to as the Mixed Layer (ML) and is characterized by thorough

mixing of heat, momentum and scalars. The flow shows little dependence on the nature of the surface and turbulent fluxes tend to decrease with height. The inner layer is known as the Surface Layer (SL). It usually comprises the lowest 10% of the ABL and is characterized by turbulent fluxes that are nearly constant with height. This can sometimes be a rough approximation but, when applicable, it leads to important simplifications such as MOS. The SL itself can be subdivided into two different layers, the Inertial Sub-layer (ISL) and the Roughness Sub-layer (RSL). When roughness elements are small, the latter is usually very shallow. Its vertical extension becomes important in rough environments such as forest canopies and urban areas, as will be addressed in section 2.3. The ISL, located above the RSL, is horizontally homogeneous since the signature of individual elements has been mixed out by turbulence. The RSL, on the other hand, exhibits a fully three-dimensional structure due to the direct influence of the roughness elements on the flow. The effect of individual roughness elements, however, cannot be easily distinguished (Otte et al., 2004) and becomes more subtle with height until it blends out completely by turbulence. This height is defined as the blending height, and represents the division between the ISL and the RSL (Glickman, 2000).

Another view of the ABL is provided in Figure 2.2, a photograph taken from an airplane flying over Central Oklahoma. It shows a cumulus cloud field. As illustrated in Figure 2.1, cloud tops coincide with the top of the ABL where an overlying layer of high stability hinders their vertical development into the free troposphere. If moisture is sufficient, clouds form in the upper region of updrafts while clear skies prevail over downdrafts. The haze observed is characteristic of most ABLs. It is caused by a combination between a large number of aerosols and high relative humidity. It contrasts with the relatively drier and clear air present in the free atmosphere above.

Figure 2.2. Photograph of a partly cloudy ABL looking downwards from an airplane during a spring afternoon in Oklahoma in 2006.

The characteristics of the ABL are determined by the characteristics of the surface, by the atmospheric conditions and by the interactions between these two. The surface of the earth can be described as a collage of features with different physical properties. From these, the ABL is particularly sensitive to variations in roughness, albedo, moisture, and various thermal properties of the surface. Roughness is very important since it modifies the characteristics of turbulence and thus several aspects of the ABL. Increased roughness favors the development and intensification of turbulence and is generally associated with larger vertical extensions of the ABL. Examples are relatively deep ABLs found over forest and urban canopies or mountain ranges when compared against those observed over flat plateaus with otherwise similar physical properties. The effects of albedo soil, moisture and thermal properties are also important, and can be explained in terms of the surface-atmosphere energy balance.

The energy available for ABL processes comes directly or indirectly from the solar radiation. The surface energy balance can be expressed via:

$$R_n = H + E + G + \Delta H_S \quad (2.1)$$

where R_n is the net radiation, E is the vertical flux of latent heat, H is the vertical flux of sensible heat, G is the heat flux into the ground and ΔH_S is the heat storage term and describes the rate of change of internal energy of the layer (Garratt, 1992; Arya, 1999). Positive R_n signifies that energy is available to be redistributed among E, H and G. From these terms, H is responsible for temperature changes in the ABL and is discussed with detail in section 2.1.2.

Net radiation R_n represents the balance between the incoming and outgoing components of electromagnetic radiation at different wavelengths. The principal input of energy into the system occurs in the form of shortwave radiation from the sun, therefore diurnal and annual cycles of solar radiation are essential for ABL processes. As indicated in equation 2.1, part of the energy available at the surface is devoted to warm up the atmosphere via H. Heat is then redistributed throughout the ABL by turbulence. Stronger surface heating can be ultimately associated with deeper ABL. Contrasting examples are the relatively deep ABL observed during daytime/summer versus those observed during nighttime/winter. The constant variation of solar zenith angles also generates complex heating/cooling mechanisms in heterogeneous surfaces such as canopies or over complex terrain such as valleys and mountain slopes in general.

The diurnal cycle of the ABL is largely determined by the diurnal cycle of the surface energy balance, driven by the diurnal cycle of solar radiation. As an example, monthly averages of the components of the energy balance measured in Vancouver, Canada are presented in Figure 2.3 after Oke (1987). The measurements were made over a suburban surface (top) and over a rural surface (bottom). In addition, a characteristic

description of the diurnal cycle of the ABL is summarized in Figure 2.4. after Kaimal and Finnigan (1994). Details are discussed in the following.

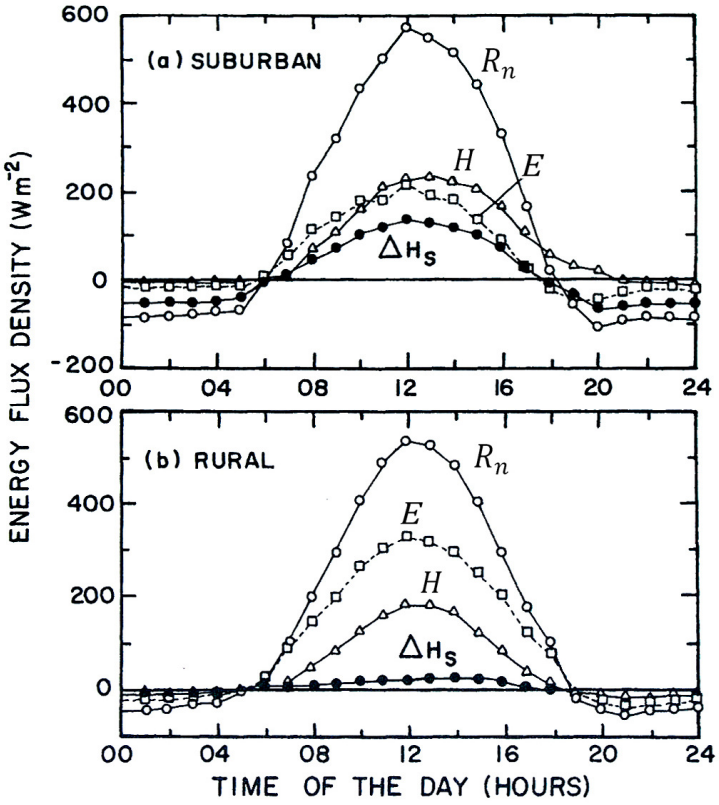

Figure 2.3. Monthly averages of the diurnal cycle of the surface energy balance in Vancouver, Canada after Oke (1987).

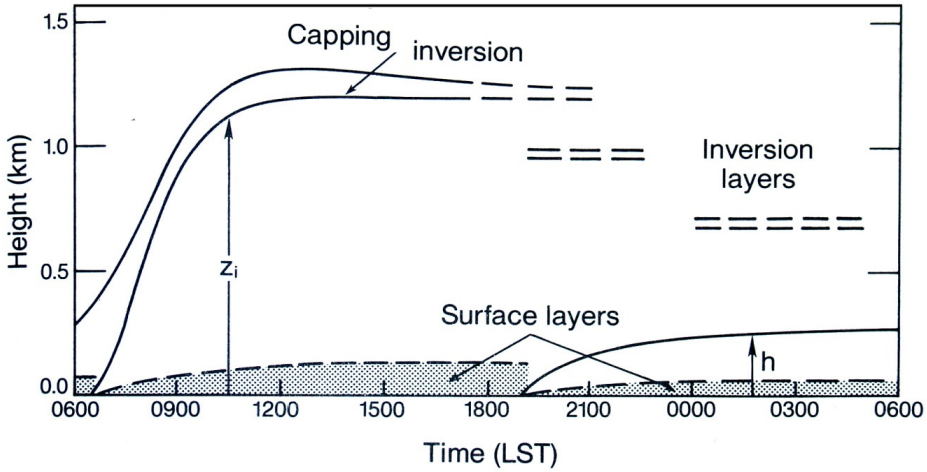

Figure 2.4. Diurnal cycle of the standard ABL after Kaimal and Finnigan (1994).

The ABL grows during daytime driven by positive H that originate at the surface once energy is available from the absorption of solar radiation. H leads to temperature gradients and the development of thermal turbulence which then transports heat and other quantities vertically. Temperature, moisture and momentum thus become well mixed in the vertical. The top of the daytime ABL is defined by a temperature inversion referred to as capping inversion. The strong stability in this layer behaves as a sharp boundary between the turbulent ABL flow and the free atmosphere above.

Once solar radiation decreases after midday sensible heat fluxes start decreasing accordingly. They eventually become negative and heating from the surface stops. In order to balance negative values of R_n, H becomes negative and heat is drawn from the atmosphere into the ground. This process leads to the development of a stable layer near the surface and decoupling with the residual mixed layer above it. The stable layer persists until sometime after sunrise when solar radiation causes R_n to become positive. Once values of R_n become large enough H becomes positive and the mixed layer starts developing again from heating originated at the surface.

The percentage of solar radiation reflected is the albedo. Since the remaining energy is absorbed and becomes available for surface energy processes, albedo is important in ABL development. High albedo leads to low energy availability at the surface. It can be associated with lower H, less thermal turbulence and generally shallower ABL. As an example, surfaces with high albedo such as white sands and salt flats reflect more solar radiation than darker surfaces such as a pine forest canopy or a parking lot paved with asphalt.

Another important variable is soil moisture. It determines which fraction of the energy available at the surface will be devoted to an increase in temperature, i.e. H; and which will be devoted to evaporation, i.e. E (equation 2.1). When soil moisture is scarce most of the energy is ingested into the atmosphere in the form of H and leads to deep ABL. An example can be found over deserts during daytime. Large values of H inland favor the development of deep ABL.

Aside from surface properties, atmospheric conditions determine the environment for the development, growth and collapse of the ABL, and are relevant for several ABL processes. Examples include pollutant advection and dispersion; development or suppression of convection; intensity and extension of mesoscale circulations such as sea, lake or valley breezes; development and intensification of heat waves; and evolution of low-level clouds among others.

Stability is important. It is determined by the vertical gradients of temperature and velocity. Vertical fluxes of heat are directed upwards/downwards under unstable/stable regimes. Unstable ABL occur mostly during daytime and are associated with vigorous turbulence and large vertical extensions. A scheme that shows the structure of a fully-developed mixed ABL present during unstable conditions is presented in Figure 2.5. reformatted after Kaimal and Finnigan (1994).

The ABL in Figure 2.5 is shaded with a dark pattern. Arrows represent the distribution of circulations that organize in thermals of different sizes. The largest updrafts reach the top of the ABL. Interactions with the free atmosphere are in the form of limited mixing due to the generally strong stability present at the ABL top. Free

atmosphere air entrains the ABL top predominantly over broad the regions of sinking motion, downdrafts, that surround large thermals.

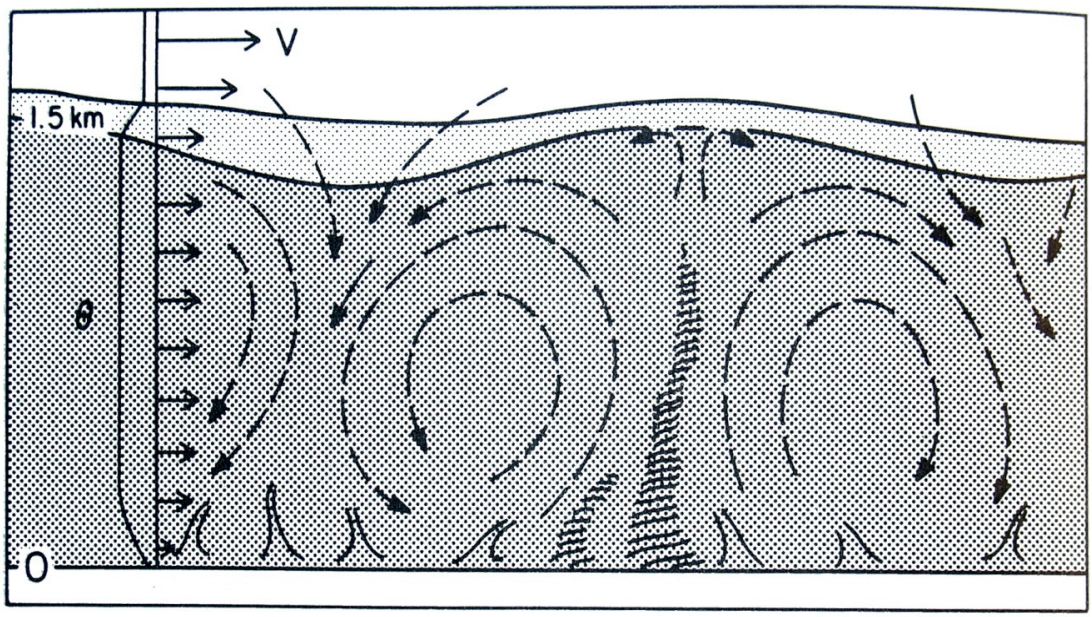

Figure 2.5. Schematic representation of the mixed ABL after Wyngaard (1990).

Wind and potential temperature profiles are sketched to the left. Average potential temperature is nearly constant with height and increases in the top of the ABL defining the capping inversion which divides well mixed ABL air from stable air above. Temperature also increases near the ground in a super-adiabatic layer that forms from intense heating of the surface.

Stable ABL form during nighttime and are associated with weaker turbulence, for the most part mechanical, and intermittent bursts of activity (Hartogensis, 2006). A schematic representation of the stable ABL is presented in Figure 2.6, also after Wyngaard (1990), and is described in the following.

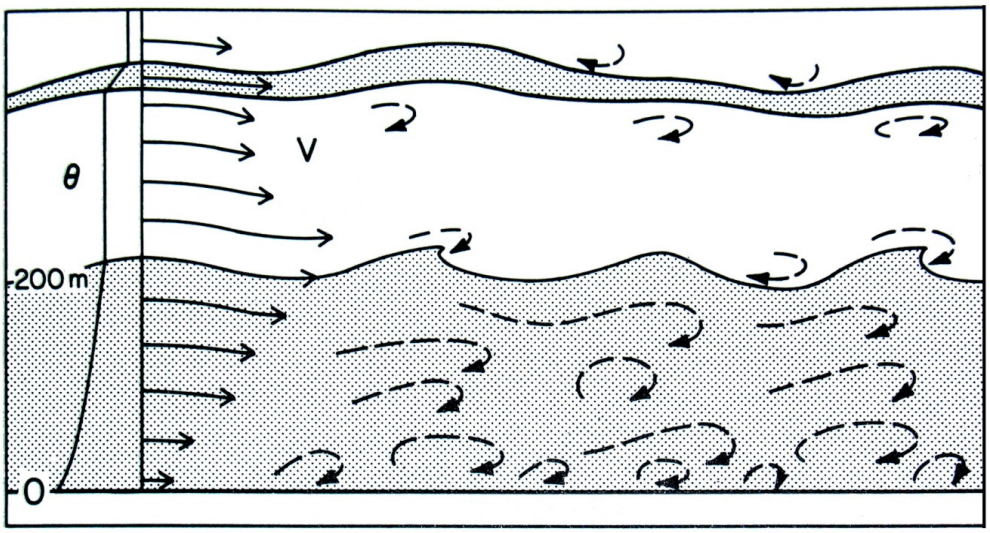

Figure 2.6. Schematic representation of the stable ABL after Wyngaard (1990).

Nocturnal stable ABL exhibit smaller vertical extensions than daytime mixed layers, in response to the absence of strong thermal forcing. They develop from surface cooling and lay underneath the residual layers produced by thorough turbulent mixing during daytime. The stable layer is characterized by temperature and velocities that increase with height and turbulence is produced only mechanically; i.e. by wind shear. As noted in Figure 2.6, velocity and temperature profiles in the stable ABL are not as well mixed when compared to mixed layer profiles. The relatively shallow extension of the stable ABL allows the development of low level jets in the residual layer region. The stability generated close to the ground suppresses vertical motion and dispersion of scalars that originate near the surface.

The vertical extension of the ABL ranges from infinitesimal to up to a few kilometers. The deepest well established ABLs develop over dry and rough terrain during periods of strong solar radiation, i.e. early afternoons during spring or summer. Yet ABL depth locally increases in cumulonimbus clouds. Shallow well established ABL develop in cold-current marine environments, snow-covered surfaces and flat regions under weak

or non-existing solar radiation forcing. Strictly speaking, however, the shallowest ABL in nature occur during transition periods, and since they originate near the surface their minimum depth can be assumed to be infinitesimal.

TT is crucial for ABL processes since heat, momentum and scalars are transported by turbulence except very close to the surface where molecular transfer dominates. Both thermal and mechanical turbulence coexist and their sources are usually difficult to discern. Thermal turbulence originates in regions where temperature gradients occur in response to differential heating and cooling of adjacent surfaces, air parcels and/or advected air masses. Mechanical turbulence is produced by wind shear, which is particularly enhanced in the RSL or/and in transition zones when ABL decoupling occurs. Thermal turbulence dominates during daytime, when solar heating of the surface leads to strong temperature gradients. Mechanical turbulence dominates during nighttime, when turbulence is produced by the interaction of the flow with the roughness elements, and by wind shear that results from the distribution of pressure in the atmosphere. Synoptic forcing also plays a role in the ratio of mechanical versus thermal turbulence. Periods with strong wind shear and low solar radiation favor the development of mechanical turbulence, e.g. passage of frontal systems, outflow boundaries and low-level jets among others. Periods with weak wind shear and strong solar heating favor the development of thermal turbulence, e.g. a sunny day with weak winds.

As described, turbulence is a key process in the ABL and understanding TT is essential to describe, model and forecast ABL processes that eventually will affect the entire troposphere. TT of sensible heat is of particular interest in the present study, thus relevant notions including its calculation using the eddy-covariance approach will be addressed in the following.

2.1.2. Sensible heat flux and the Eddy-Covariance approach.

Sensible heat Q_H is the portion of the total heat associated with a temperature difference (Stull, 2000). It can be expressed via:

$$Q_H = m\, C_p\, \Delta T \tag{2.2}$$

where m is mass, $C_p \sim 1004$ J kg^{-1} K^{-1} is the specific heat of air at constant pressure and ΔT is the temperature difference associated with Q_H. Sensible heat in a fluid is transported by the flow. The flux of Q_H is defined as its transport across a unit area. Q_H in the ABL is transported by turbulence, hence the sensible flux of heat in the ABL can be referred to as turbulent flux of sensible heat. The vertical component of sensible heat flux is of particular interest, as it describes the connection between most surfaces and the atmosphere. Horizontal components gain importance when the contribution of fluxes normal to vertical surfaces becomes non-negligible. This is true in the urban environment where the fluxes from building walls affect TT between the surface and ultimately the RSL (Harman et al., 2004).

The Eddy Covariance or Eddy Correlation (EC) approach computes fluxes using turbulent components of velocities and of the properties being transferred (Kaimal and Finnigan, 1994). It is a direct method since it is does not require the use of empirical constants (Foken, 2006). This method has been used over several decades to calculate sensible heat fluxes. Some examples are available in Raupach (1979), Kaimal and Wyngaard (1990), Rotach (1995), Berger et al. (2001), McAloon (2001), Wilczak et al (2001), Weiss (2002), Baldocchi (2003), Finnigan et al. (2003), Salmond et al. (2003), Van de Wiel et al. (2003), Grimmond et al. (2004), Finnigan (2004), Mestayer et al.

(2005), Foken (2006), Randow et al. (2006), Hoedjes et al. (2007) and Kleissl et al. (2008) among others.

Turbulent components are calculated by subtracting high temporal resolution measurements from a mean state following the Reynolds Decomposition Method (Garratt, 1992; Kaimal and Finnigan, 1994; and Arya 1999):

$$u(t) = \bar{u} + u'(t) \tag{2.3}$$

$$v(t) = \bar{v} + v'(t) \tag{2.4}$$

$$w(t) = \bar{w} + w'(t) \tag{2.5}$$

$$T(t) = \bar{T} + T'(t) \tag{2.6}$$

where $u(t)$ are the observed values of zonal velocity, $\bar{u}$ represents zonal velocities averaged over a period of time τ and $u'(t)$ are the perturbations from the mean state. The same applies for meridional velocity, vertical velocity and temperature respectively. High temporal resolution data are usually obtained using hot wire and sonic anemometers.

Once data becomes available, the definition of a mean state is necessary. The period of time τ used to define the mean state has been a topic of wide discussion. Some authors agree that τ should be in the order of tens of minutes to achieve acceptable significance in the convective ABL, e.g. Wyngaard (1973) and Thiermann and Grassl (1992). Lee et al. (2004) discussed the use of Ogive Plots to depict adequate averaging periods. Ogive Plots integrate under the cospectral curve and thus show the cumulative contribution of eddies of different size to the total transport. Using plots from the Chewawegon tower dataset (Berger et al., 2001), Lee et al. (2004) suggested that a value of τ=30 minutes was sufficiently large to account for stationarity of near-ground data. Finnigan et al. (2003) agreed and indicated that the averaging period increases away from

the ground with the increase of spatial and temporal scales. Based on these studies, τ=30 minutes was used to define the mean state of ILREUM data.

A common practice over flat and homogeneous terrain is to use streamline coordinates, where the *x*-direction is always parallel to the mean flow (Kaimal and Finnigan, 1994), as illustrated on Figure 2.7. The use of this system eliminates problems associated with instrument alignment and allows a simpler interpretation of turbulence properties in terms of along and across-flow components. Averages recalculated for a dataset exposed to a 2-3 rotation become zero for the cross-flow components $\overline{v_R} = 0$ and $\overline{w_R} = 0$. More detailed descriptions of this method can be found in Wilczak (2001), Finnigan (2003), Foken (2003) and Lee et al. (2004).

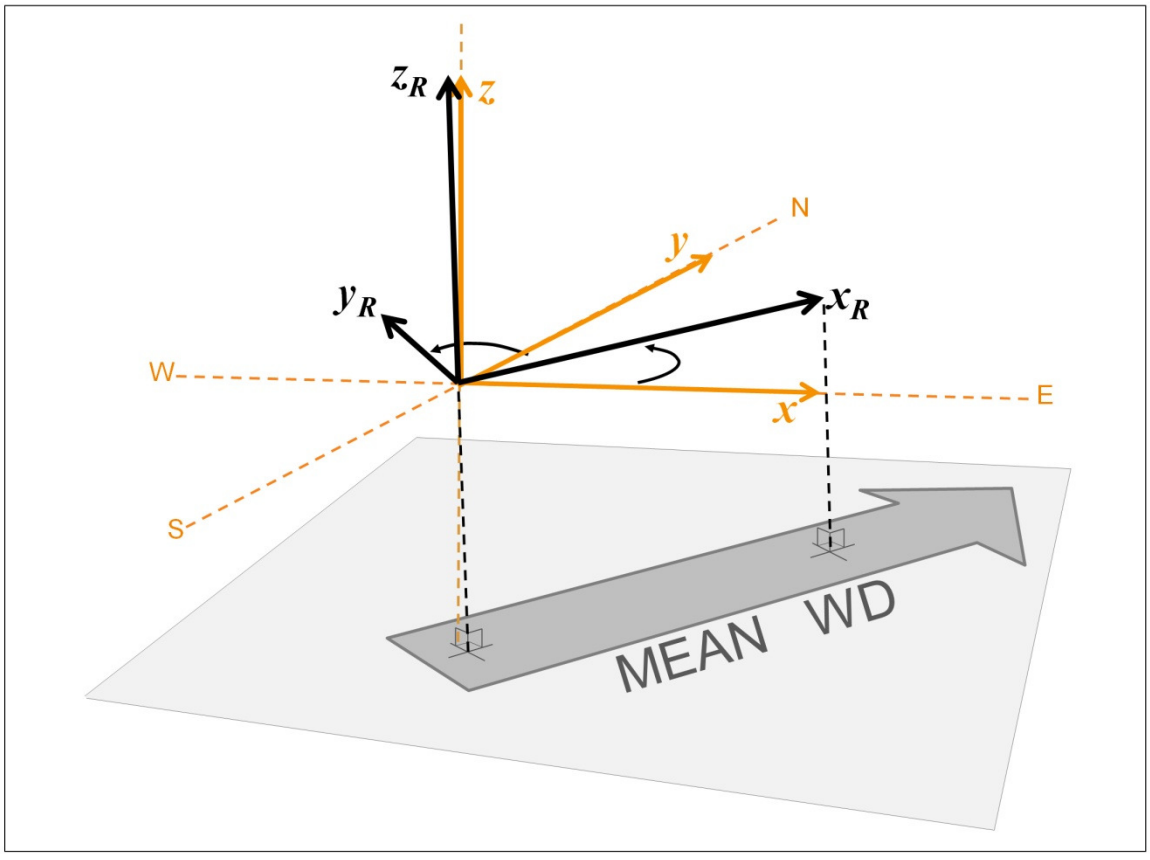

Figure 2.7. Scheme of the 2-3 rotation technique applied to the Cartesian Coordinate system to convert it into the Streamline Coordinate System. Original (rotated) vectors are indicated in orange (black).

Turbulent velocities for the along-flow, $u_R{}'$ and cross-flow components $v_R{}'$ and $w_R{}'$ are calculated using the Reynolds Decomposition Method, which yields:

$$u_R{}' = u_R - \overline{u_R} \tag{2.7}$$

$$v_R{}' = v_R \tag{2.8}$$

$$w_R{}' = w_R \tag{2.9}$$

Covariances can then be calculated by multiplying perturbations and averaging them over τ. If potential temperature measurements are made, the covariance of potential temperature and vertical velocity can be expressed as:

$$H_K = \overline{w_R{}'\theta'} \tag{2.10}$$

where θ' represents potential temperature perturbations. H_K is the kinematic flux of sensible heat and describes the net heat transported by turbulence across a horizontal surface. H_K is expressed in units of Kms^{-1}. Sensible heat fluxes in Wm^{-2} are attained by considering the density of air ρ and C_P via:

$$H = \rho C_P H_K \tag{2.11}$$

Potential temperature θ is preferred since it is conserved during adiabatic processes. It represents the temperature that a parcel would have if it were brought to 1000 hPa adiabatically, and can be expressed as:

$$\theta = T\left(\frac{P_0}{P}\right)^{R_d/C_p} \tag{2.12}$$

where P_0 is 1000 hPa and P is atmospheric pressure and $R_d \sim 287\ \mathrm{J\,kg^{-1}K^{-1}}$ is the gas constant for dry air.

The horizontal components of sensible heat fluxes become important in the urban canopy (see section 2.3) where part of the heat stored by buildings is released into the atmosphere through building walls. When the structure of the flow is complex coordinate rotation is not recommended. Expressions for sensible heat fluxes thus become:

$$H_x = \bar{\rho} C_P \overline{u'\theta'} \tag{2.13}$$

$$H_y = \bar{\rho} C_P \overline{v'\theta'} \tag{2.14}$$

$$H_z = \bar{\rho} C_P \overline{w'\theta'} \tag{2.15}$$

where H_x, H_y and H_z are the zonal, meridional and vertical components of sensible heat flux in Wm^{-2}.

Sensible heat fluxes represent the transport of heat. Positive H_z arise from positive values of $\overline{w'\theta'}$ and indicate that the net transport of heat by turbulence during τ is upwards. Negative H_z indicate that the net transport of heat during τ is downwards. A more clear physical understanding can be attained with the four quadrant analysis explained in Figure 2.8. Fluxes are positive when the warm air is transported upwards or cool air is transported downwards by turbulence. Both situations correspond to cases where unstable stratification prevails. On the other hand, negative fluxes arise from cool air transported upwards or warm air transported downwards, which corresponds to stable stratification.

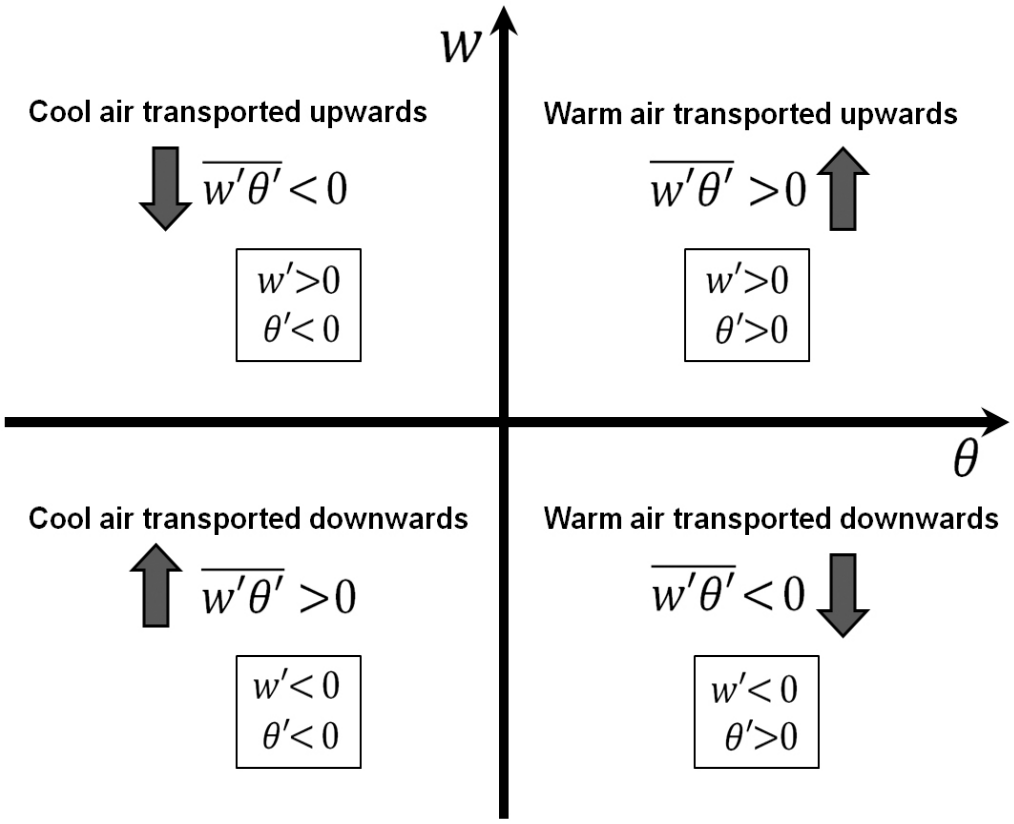

Figure 2.8. Four quadrant analysis of vertical heat fluxes using turbulent velocities and temperatures.

2.1.3. Monin-Obukhov Similarity: a critical consideration.

The Navier-Stokes equations describe atmospheric motions. They can be modified to resolve the effects of turbulence in the ABL via Reynolds Decomposition. This modification, however, results in a larger number of unknowns than equations and cannot be solved analytically without the aid of some kind of parameterization. Although new equations can be derived for the covariance terms, new triple correlation terms appear and the need for either deriving new sets of equations for these, or parameterizing their values arises again. This issue is known as the Turbulence Closure problem (i.e. more information in Garratt, 1992; Arya, 1999; and Glickman, 2000) and implies that the stochastical description of turbulence demands an infinite set of equations. The Turbulence Closure Problem can be successfully addressed inside the SL with the similarity hypothesis proposed by Monin and Obukhov (1954), which is described in the following based mostly on the summary available in Arya (1999).

The Monin-Obukhov Similarity (MOS) hypothesis is a very successful tool to describe the vertical distribution of basic parameters in the SL (Sorbjan, 1989). MOS stipulates that mean gradients and turbulence characteristics of a stratified SL depend only on the height z, the kinematic surface stress τ_0/ρ, the kinematic heat flux H_K and buoyancy parameter g/T (Arya, 1999); where τ_0 is the surface stress and g is the acceleration of gravity. This simplification is very important to establish a connection between the surface and the rest of the ABL. MOS assumes that vertical fluxes of momentum and sensible heat are constants within the SL, generally a good approximation since the decrease with height is usually smaller than 10% throughout the entire layer (Panofsky and Dutton, 1984). It also assumes horizontal homogeneity and stationarity, which limits its applicability.

Four independent scales can be defined: friction velocity u_*, virtual friction temperature θ_{v*}, height above the surface z and the buoyancy length, also known as the Monin-Obukhov or Obukhov length L, where:

$$u_* = \left[\overline{u'w'}^2 + \overline{v'w'}^2\right]^{1/4} = \left[\frac{\tau_0}{\rho}\right]^{1/2} \tag{2.16}$$

$$\theta_{v*} = \frac{-\overline{w'\theta_{v'}}}{u_*} \tag{2.17}$$

$$L = \frac{\overline{\theta_v} {u_*}^2}{g\kappa\theta_{v*}} \tag{2.18}$$

where $\kappa \sim 0.4$ is the Von Kármán constant. $\overline{\theta_v}$ is the virtual potential temperature averaged over τ and the virtual potential temperature θ_v is defined as follows:

$$\theta_v = \theta(1 + 0.61\, r_V) \tag{2.19}$$

where r_V is specific humidity (Stull, 2000). In our case, the effects of moisture were not considered, thus θ_v was replaced by θ in equations 2.17 and 2.18. Monin and Obukhov (1954) also introduced the concept of non-dimensional height ζ that can be used to describe stability in the SL:

$$\zeta = \frac{z}{L} \tag{2.20}$$

ζ is zero/positive/negative under neutral/stable/unstable conditions. Its behavior is similar to that of the Richardson number Ri and expressions that relate them can be found in Arya (1999).

MOS states that vertical gradients of various atmospheric quantities can be normalized by combinations of the scaling parameters, and become universal functions of dimensionless height ζ. The expressions for velocity and potential temperature are:

$$\left(\frac{\kappa z}{u_*}\right)\left(\frac{\partial u}{\partial z}\right) = \varphi_m(\zeta) \tag{2.21}$$

$$\left(\frac{\kappa z}{\theta_*}\right)\left(\frac{\partial \theta}{\partial z}\right) = \varphi_h(\zeta) \tag{2.22}$$

where $\varphi_m(\zeta)$ and $\varphi_h(\zeta)$ are the universal functions of ζ for momentum and heat. The term 'universal' refers to the validity of these functions is SL that fulfill MOS applicability conditions. In reality not all SL assumptions are perfectly fulfilled and these expressions become close approximations.

Equations (2.21) and (2.22) define vertical gradients of wind and temperature over a layer of infinitesimal depth inside the SL. Their integration leads to:

$$\frac{\kappa u(z)}{u_*} = ln\frac{z}{z_0} - \Psi_m(\zeta, \zeta_0) \tag{2.23}$$

$$\frac{\kappa(\theta(z)-\theta_0)}{\theta_*} = ln\frac{z}{z_{0T}} - \Psi_h(\zeta, \zeta_0) \tag{2.24}$$

respectively, where z_{0T} is the thermal roughness length (Garratt, 1992). $\Psi_m(\zeta, \zeta_0)$ and $\Psi_h(\zeta, \zeta_0)$ are stability corrections for profiles in the neutral SL and can be expressed as integral forms of the universal functions for momentum and heat as follows:

$$\Psi_m(\zeta, \zeta_0) = \int_{\zeta_0}^{\zeta}[1 - \varphi_m]d\ln\zeta \tag{2.25}$$

$$\Psi_h(\zeta, \zeta_0) = \int_{\zeta_0}^{\zeta}[1 - \varphi_h]d\ln\zeta \tag{2.26}$$

Once the universal functions are established, vertical profiles of SL quantities and statistics can be reliably sketched by only knowing the values of the four SL scales (Garratt, 1992). The universal functions are thus important and their shapes can be determined empirically via measurements made under conditions where MOS applies. This has already been explored by several authors (e.g. Dyer and Hicks, 1970; Businger et al., 1971; Wyngaard and Coté, 1971; Dyer, 1974; Högström, 1988). There is still some controversy about their exact forms, but amongst all, those suggested by Businger et al. (1971) and Dyer (1974) have been widely accepted by BL researchers. More information about MOS can be found in Monin and Yanglom (1971) and in Panofsky and Dutton (1984).

MOS was not designed for environments where the conditions of homogeneity and stationarity are violated. This is true in the RSL, where horizontal heterogeneity prevails. Since scintillometers depend on MOS, they were not designed to be used inside the heterogeneous environments. Several studies have yet demonstrated good agreement with EC measurements made at different sections of the path. Some examples can be found in Meijninger et al. (2002), Kanda et al. (2002), Salmond et al. (2003), Lemonsu et al (2004), Meijninger et al. (2005) and Roth et al. (2006). Examples of some successful intercomparisons between SLS and EC measurements over heterogeneous environments, especially the RSL, is described with more detail in section 2.2.3. The suggestion that MOS violation is minimal is encouraging to explore the aplicability SLS measurements inside the RSL.

2.2. Scintillometry theory.

Scintillations are fluctuations of intensity of electromagnetic radiation caused by turbulence in a media. Turbulent eddies produce variations in the refractive index of the media, which alters the propagation of electromagnetic radiation. Scintillations occur in the atmosphere, and can sometimes be captured by the human eye. Examples include distorted visibility and sensation of movement over a paved road during a hot and sunny summer day or the twinkling of stars.

Scintillations can be measured with scintillometers. When used in the SL, these instruments sense radiation intensity and translate its fluctuations into turbulent fluxes once wave propagation theory and MOS are considered. Scintillometers consist of a transmitter and a receiver that are separated by path lengths that vary between tens of meters and about ten kilometers. As a result, they measure path-integrated quantities, which is considered one of their major advantages over point-sampling devices. Scintillometer data are also unaltered by mast distortion and horizontal misalignment issues, and represent averages over short intervals while EC data require τ in the order of tens of minutes. Their ability to measure fluxes over short averaging intervals has important applications such as measuring the often non-stationary stable boundary-layer (Hartogensis , 2006).

The transmitter emits electromagnetic radiation at optical or radio wavelengths. SL turbulence affects propagation and produces refractive index scattering that, when integrated over a propagation volume, leads to fluctuations in radiation intensity that are measured by the receiver. Scintillations are defined as the logarithms of the variances of these fluctuations.

Scintillometers are classified into two types based on aperture and associated path length: large-aperture scintillometers (LAS) and small-aperture scintillometers (SAS). LAS emit radio wavelengths that need to transverse distances between 0.5 and 10-km to measure a signal that can be interpreted by the receiver (Wang et al., 1978 and Kleissl et al., 2008). SAS on the other hand require distances in the order of 50 to 200 m. The aperture diameter of LAS is larger than the Fresnel zone (De Bruin, 2002). The Fresnel distance, $Z_F = \sqrt{\lambda P_L}$, describes the size of the most active eddies present along the propagation path, where λ is the optical wavelength and P_L the path length. SAS have smaller apertures and are also referred to as 'laser scintillometers' since they emit radiation at optical wavelengths. SAS can also be bichromatic and emit two radiation beams at once. The beams must have different polarizations so the receiver can recognize them individually. Bichromatic scintillometers have an advantage over LAS: they can calculate the inner scale of turbulence l_0 from the covariance of intensity fluctuations. The measurement of l_0 eliminates the need to introduce additional parameters and variables such as z_0 and u_*, which need to be considered in LAS measurements (Hartogensis, 2006).

2.2.1. Relevant concepts.

An important concept is that of energy spectra, described with more detail in Kaimal and Finnigan, 1994; Arya, 1999 and Hartogensis, 2006. Energy spectra describe how energy is distributed among different scales of motion, and is essential for the study of turbulence. Turbulent kinetic energy (TKE) is produced by buoyancy and shear at larger scales, where it can also be destroyed by buoyancy under stable conditions. Energy available in the largest eddies is transmitted to eddies of smaller size. The range of length

scales in which energy is not produced or destroyed but only redistributed toward smaller scales is known as the inertial range (IR) of energy spectra, and the energy re-distribution process is known as the energy cascade. At scales smaller than those of the IR, energy is dissipated by the viscosity of the flow. The range of scales where viscous dissipation dominates is known as the dissipation range of turbulence spectra (DR). A schematic representation of turbulence spectra is displayed in Figure 2.10.

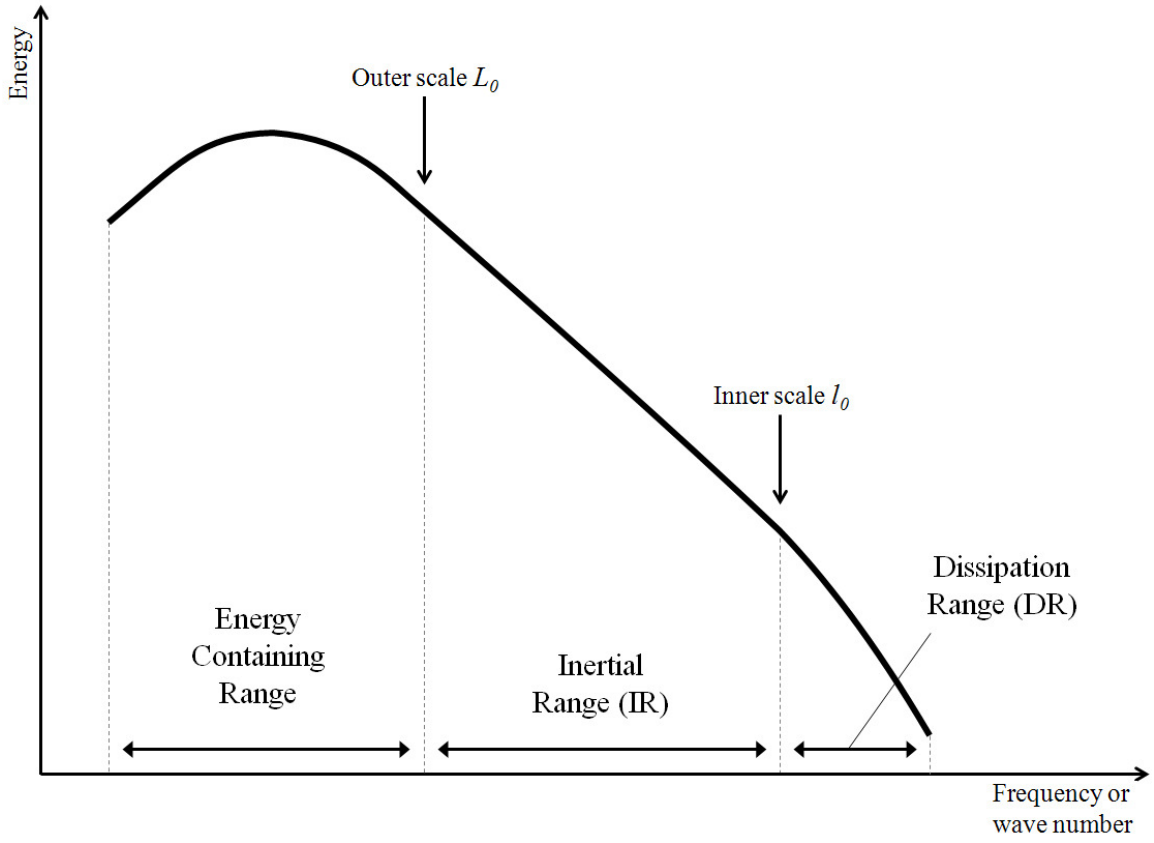

Figure. 2.9. Schematic representation of turbulence spectra.

The smallest eddy size at which turbulence dissipates is described by the Kolmogorov Microscale η_K and is a function of the dissipation rate of TKE ε and the viscosity of air. An expression for η_K is:

$$\eta_K = \left(\frac{\nu^3}{\varepsilon}\right)^{1/4} \tag{2.27}$$

where ν is the kinematic viscosity of air. The length scale used to describe eddy sizes associated with dissipation maxima as well as the boundary between the IR and DR is the inner scale of turbulence l_0. η_K is proportional to l_0 via:

$$l_0 = 7.4\eta_K = 7.4\left(\frac{\nu^3}{\varepsilon}\right)^{1/4} \tag{2.28}$$

where the constant of proportionality 7.4 has been considered by several authors, e.g. Hill (1997), Hartogensis (2006), SCINTEC AG (2006).

The log-covariance of refractive index fluctuations σ_{xy}^2 measured by the scintillometer is modulated by the most active eddies in optical scintillometry. These eddies have sizes in the order of l_0, which allows the establishment of relationships between σ_{xy}^2 and l_0. Covariances decrease as eddy sizes decrease. A graphic example is presented in Figure 2.10. Hartogensis (2006) indicated that when l_0 increases above ~ 20 mm the covariance levels off as eddy sizes increase and not much information is gained with eddy size increase anymore.

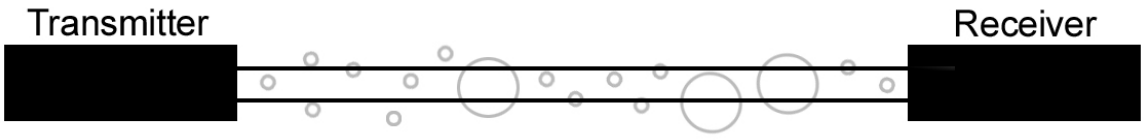

Figure. 2.10. Schematic representation of eddy sizes with respect to scintillometer beam separation. Turbulent eddies are represented with gray circles.

The relation between l_0 and σ_{xy}^2 together with equation 2.28 allows to retrieve ε from measurements of σ_{xy}^2. MOS can then be used to determine values of SL

scales from ε. An expression for non-dimensional dissipation $\varphi_\varepsilon(\zeta)$ can be established using height above the ground z and friction velocity u_* as scaling parameters:

$$\frac{\kappa z}{u_*^3}\varepsilon = \varphi_\varepsilon(\zeta) \tag{2.29}$$

In this case the unknown is the friction velocity u_*. Universal expressions for $\varphi_\varepsilon(\zeta)$ are available in the literature. They have been determined empirically by fitting curves to simultaneous measurements of ε and u_*. Equation 2.29 then allows to determine values of u_* from ε, which shows that σ_{xy}^2 can be ultimately used to determine u_*.

Another concept important in scintillometry is that of structure functions, which can be established in the IR of turbulence spectra where motions can be assumed as random and locally isotropic. The second order structure function for the refractive index of air n, after isotropy is assumed, can be expressed as:

$$D_n(r) = \overline{[n(x) - n(x+r)]^2} \tag{2.30}$$

where x is the spatial coordinate, r is the distance between measurements and D_n represents the second order structure function of n (Kaimal and Finnigan, 1994; and Hartogensis, 2006). Structure function parameters can be obtained from structure functions by considering the distance between simultaneous observations. They represent statistical representations of turbulence and thus are relevant in scintillometry. The structure function parameter of refractive index fluctuations C_n^2 can be expressed via:

$$C_n^2 = \frac{D_n(r)}{r^{2/3}} = \frac{\overline{[n(x)-n(x+r)]^2}}{r^{2/3}} \tag{2.31}$$

(Monin and Yanglom, 1971 and De Bruin et al., 1995) and will be discussed with more detail in section 2.2.2.

2.2.2. Calculation of turbulent fluxes from scintillations.

The beam aperture of the small aperture scintillometer (SAS) lies within the dissipation range of turbulence and is small compared to the Fresnel zone Z_f. This is important to capture the strongest signal and avoid contamination by reflection from adjacent surfaces. Tatarskii (1961) was the first to relate the variance of the logarithm of the amplitude of intensity fluctuations σ_x^2 to C_n^2 and l_0. The approach developed assumed isotropic turbulence and weak scintillations (Thiermann and Grassl, 1992). The last constrain limited scintillometer path length since fluctuation intensity increases with increasing sampling volume. SAS can thus be operated over path lengths shorter than 200 m (Hartogensis, 2006).

This study uses the SLS20 model (hereafter, SLS) manufactured by Scintec AG and used by Thiermann and Grassl (1992) and Hartogensis (2006). Details about the instrument can be found in Scintec AG (2006). The SLS uses two parallel light beams at a wave length of $\lambda = 670$ nm. The beams are displaced by a distance of $d = 2.7$ mm and have orthogonal polarizations. The SLS measures both σ_x^2 and σ_{xy}^2, which can be used to calculate C_n^2 and l_0, which can in term be used to calculate SL scales and turbulent fluxes of sensible heat and momentum.

A summary of the process is presented in Figure 2.11, which will be frequently addressed to describe the process in the rest of this section. Input variables and parameters are shown with blue boxes, calculations with green boxes, calculated variables with purple boxes and the final output with orange boxes. Thick black arrows indicate the flow of the main algorithm. Gray arrows indicate the places where values of parameters and variables enter the algorithm. The region near the end of the algorithm shaded in light gray indicates MOS expressions.

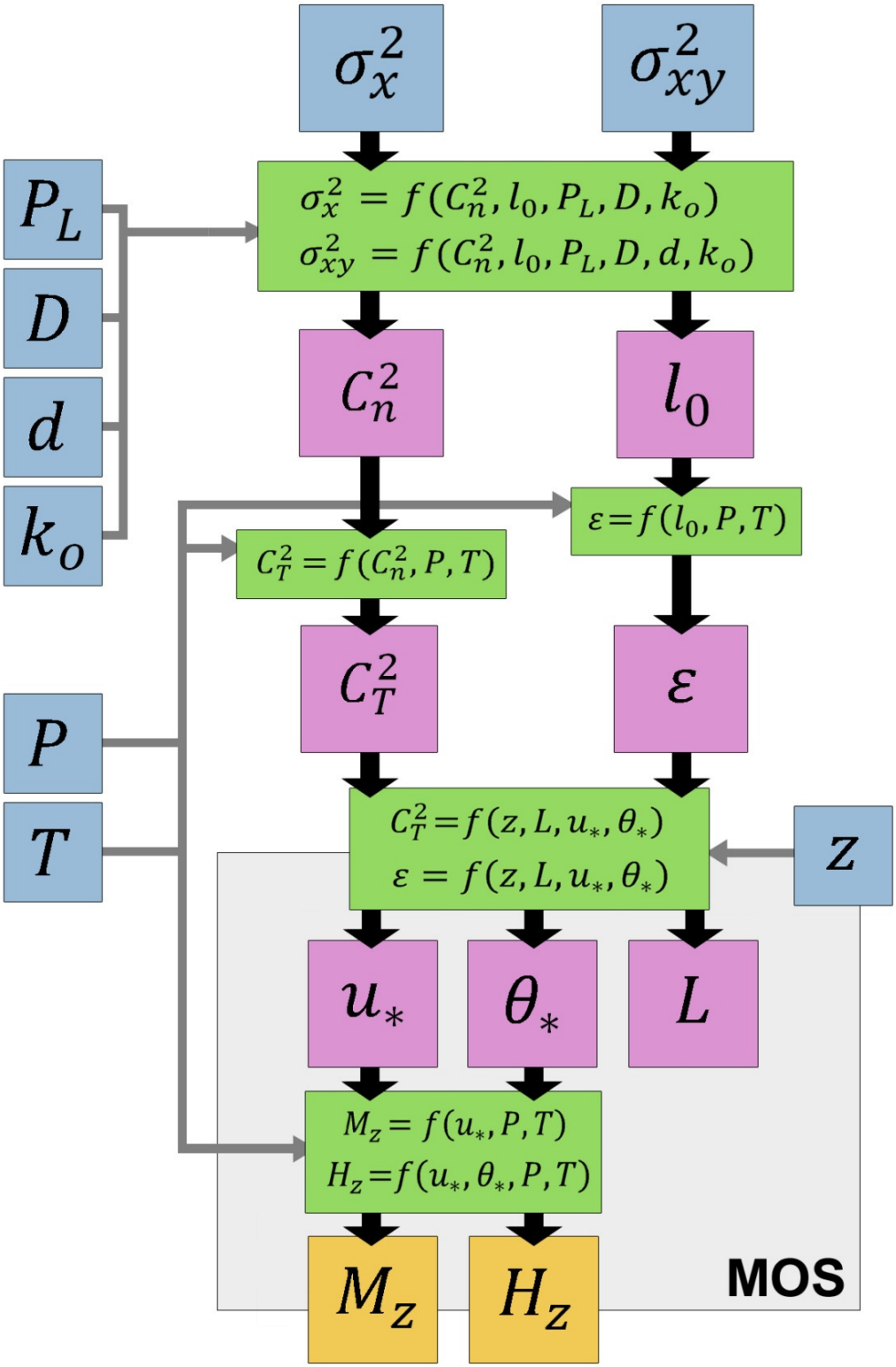

Figure. 2.11. SLS algorithm to retrieve fluxes from scintillations. Input variables and functions are indicated in blue. Output variables are indicated in orange. Calculated variables are indicated in purple and mathematical expressions are in green.

Hill and Lataitis (1989) presented the following expression to describe the log-covariance of amplitude of refractive index fluctuations σ_{xy}^2 also used by Thiermann and Grassl (1992), Weiss (2002) and Scintec, AG (2006):

$$\sigma_{xy}^2 = 4\pi^2 {k_o}^2 \int_0^{P_L} \int_0^{\infty} k\phi_n(k, l_0, C_n^2) J_0(kd) \sin^2\left(\frac{k^2 x(P_L - x)}{2k_o P_L}\right) \left[\frac{4J_1^2\left(\frac{kDx}{2P_L}\right)}{\left(\frac{kDx}{2P_L}\right)^2}\right] dk\, dx \qquad (2.32)$$

In this equation x is the spatial coordinate along the propagation path length P_L, k is the spatial wave number, and k_o is the optical wave number. ϕ_n is the three-dimensional refractive index spectra, which is a function of the spatial wave number k, l_0 and C_n^2. J_0 and J_1 are Bessel functions of the first kind. d is the distance between both radiation beams and D is the aperture diameter. If saturation is present, the covariance measured becomes smaller than that predicted by equation (2.32). The variance of refractive index fluctuations can be expressed as:

$$\sigma_x^2 = 4\pi^2 {k_o}^2 \int_0^{P_L} \int_0^{\infty} k\phi_n(k) \sin^2\left(\frac{k^2 x(P_L - x)}{2k_o P_L}\right) dk\, dx \qquad (2.33)$$

(Weiss, 2002). The three-dimensional refractive index spectra has the form of

$$\phi_n(k, l_0, C_n^2) = 0.033 C_n^2 k^{-\frac{11}{3}} f_{\phi_n}(k, l_0) \qquad (2.34)$$

where the first three terms describe refractive index spectra in the inertial range and $f_{\phi_n}(k, l_0)$ describes refractive index spectra in the dissipation range (Hill, 1978 and 1992). An approximation for $f_{\phi_n}(k, l_0)$ was first developed by Tatarskii (1971), who based his work upon a formula for velocity spectra suggested by Novikov (1961). The largest limitations of the Tatarskii approximation were in the dissipation range. The approximation proposed by Hill (1978) led to some improvement. Hill's expression,

however, is still limited in accuracy due to the difficulty of measuring refractive index spectra in the dissipation range, which requires accurate high frequency measurements. An example of different refractive index spectra was plotted by Weiss (2002) and is presented in Figure 2.12. Figure 2.13 compares scaled versions of the Tatarskii and the Hill spectra.

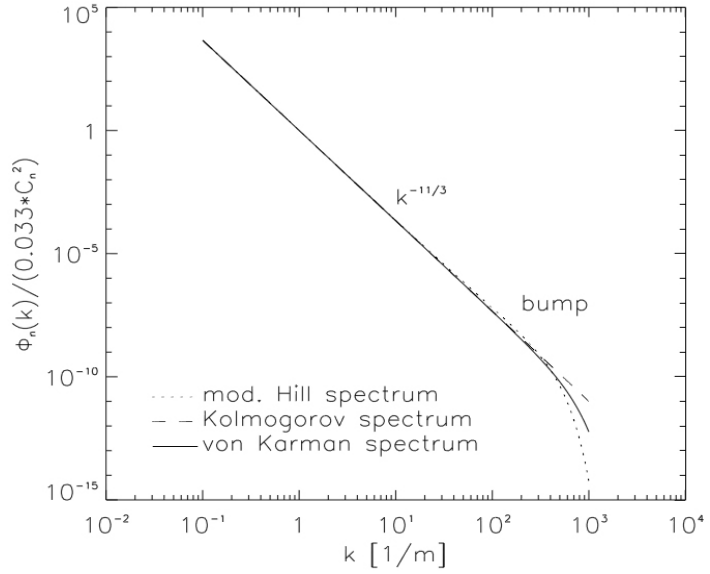

Figure. 2.12. Comparison of different representations of refractive index spectra plotted by Weiss (2002).

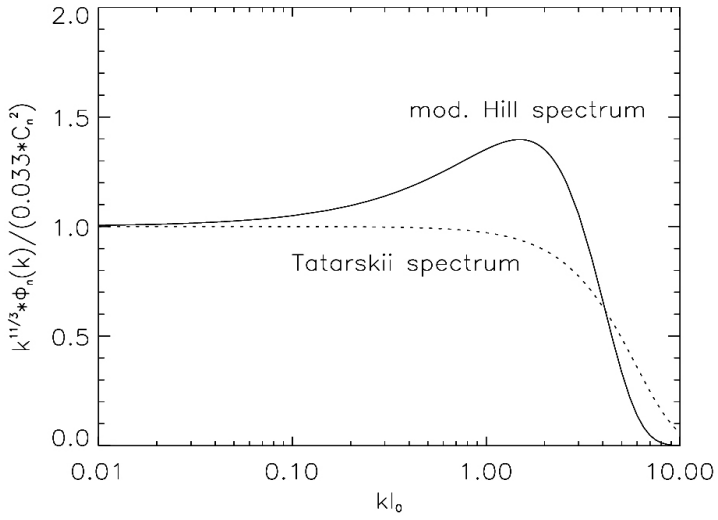

Figure. 2.13. Comparison of scaled versions of the Tatarskii Spectrum (dotted line) and Hill Spectrum (solid line) Weiss (2002).

The differences are larger in the dissipation range and in the high wave number end of the inertial range. The replacement of the Tatarskii Spectrum with that of Hill lead to significant improvement in the calculation of sensible heat fluxes from scintillations (Thiermann and Azoulay, 1989). Yet, some problems are still present and arise from limitations on the representation of the dissipation range. More information about the Hill spectrum can be found in Hill (1978), Thiermann and Azoulay (1989), Thiermann and Grassl (1992), Weiss (2002) and Hartogensis (2006).

Once C_n^2 and l_0 become available from scintillations they can be used to calculate C_T^2 and ε. C_n^2 is affected by temperature, moisture and pressure. Hartogensis (2006) indicated that the effects of pressure variations are so small that they can be neglected. The effects of moisture variations are negligible only for scintillometers that operate in the visible or near-infrared region. This is the case of displaced beam small aperture scintillometers such as the SCINTEC SLS20 model. C_T^2 can be related to C_n^2 via:

$$C_T^2 = C_n^2 \frac{T^4}{AP^2}\left[1 + \frac{0.03}{\beta}\right] \tag{2.35}$$

where T is air temperature in K, P is air pressure in Pa and $\beta = H/E$ is the Bowen Ratio or latent heat flux divided by sensible heat flux (SCINTEC AG, 2006). The constant A is a function of wavelength and for $\lambda = 670$ nm, $A = 7.887 \times 10^{-1}$ KPa^{-1} (Meijninger et al. 2002, Hartogensis, 2006 and SCINTEC AG, 2006).

On the other hand, ε is calculated using equation 2.28. The kinematic viscosity of air ν can be calculated from temperature and pressure measurements via:

$$\nu = \frac{R_d T}{P}\left[1.7 + 4.9 \times 10^{-3}\, T\right] \times 10^{-5} \tag{2.36}$$

where T can be expressed in Celsius and P in hPa (SCINTEC AG, 2006). $R_d = 287$ J Kg^{-1} K^{-1} is the gas constant for dry air.

Once C_T^2 and ε are available, MOS can be used to retrieve turbulent fluxes of heat and momentum. As shown in section 2.1.3, MOS allows to non-dimensionalize SL quantities using SL scales and non-dimensional variables can be expressed in terms of empirical approximations that are functions of dimensionless height ζ. A non-dimensional expression for C_T^2 is

$$\frac{z^{-2/3}}{\theta_*^2} C_T^2 = \varphi_{C_T^2}(\zeta) \tag{2.37}$$

and the one for ε is described in 2.29. From the different empirical approximations to $\varphi_{C_T^2}(\zeta)$ and $\varphi_\varepsilon(\zeta)$ available in the literature, those considered by Thiermann and Grassl (1992) and SCINTEC AG (2006) were tested and produced satisfactory results. The sensitivity of sensible heat fluxes to alternative approximations to $\varphi_\varepsilon(\zeta)$ was explored and was found to be very small. A more detailed description is presented in Appendix 1.

The forms of $\varphi_{C_T^2}(\zeta)$ and $\varphi_\varepsilon(\zeta)$ are different upon stratification. The expressions considered have the following forms for $\varphi_{C_T^2}(\zeta)$:

$$\varphi_{C_T^2}(\zeta) = 4\beta_1 \left[1 - 7\zeta + 75\zeta^2\right] \qquad \text{for } \zeta < 0 \tag{2.38}$$

$$\varphi_{C_T^2}(\zeta) = 4\beta_1 \left[1 + 7\zeta + 20\zeta^2\right] \qquad \text{for } \zeta > 0 \tag{2.39}$$

and for $\varphi_\varepsilon(\zeta)$:

$$\varphi_\varepsilon(\zeta) = [1 - 3\zeta]^{-1} - \zeta \qquad \text{for } \zeta < 0 \tag{2.40}$$

$$\varphi_\varepsilon(\zeta) = \left[1 + 4\zeta + 16\zeta^2\right]^{-1/2} \qquad \text{for } \zeta > 0 \tag{2.41}$$

where $\beta_1 \sim .86$ is the Obukhov-Corrsin constant (SCINTEC AG, 2006). Solving equations 2.38 through 2.41 requires an iteration scheme and leads to the calculation of three SL scales: u_*, θ_* and L.

The calculated SL scales can then be used to calculate turbulent fluxes of heat H_{SLS} and momentum M_{SLS} via:

$$H_{SLS} = -\bar{\rho} C_p u_* \theta_* \tag{2.42}$$

and

$$M_{SLS} = -\bar{\rho} u_*^2 \tag{2.43}$$

One important limitation is that stability cannot be determined by the scintillometer. It needs to be calculated using a complementary platform. An approach to the problem is to use sonic anemometers placed along the scintillometer path and was considered in this study.

2.2.3. Applicability.

Several studies have measured turbulent fluxes with scintillometers. Examples can be found in Wesely (1976), Hill et al. (1992, 1997), Azoulay et al. (1988), Thiermann and Grassl (1992), Green et al. (1994), De Bruin et al. (1995) and Chehbouni et al. (1999) among others. Most of these have focused on the homogeneous and stationary SL due to MOS validity requirements. Their results showed good agreement when compared against sonic anemometer measurements. The discrepancies found were below 20%, e.g. 10-20% (Thiermann and Grassl, 1992), ~ 7% (Green et al., 1994), lower than 10% and ~10% (Chehbouni et al., 1999).

Reasonable values of agreement prompted some studies to investigate the applicability of MOS over heterogeneous surfaces including urban areas. Surprisingly, they found that MOS violation was generally small and that the measurements could be adapted by modifying the empirical approximations to non-dimensional MOS functions. An example is the study of Meijninger et al. (2005) who explored the relationship between scintillometer and EC sensible heat fluxes over forests, grasslands and cereals in Northern Germany. They found reasonable agreement with discrepancies were in the order of 20%. Another example can be found in Meijninger et al. (2002) who found discrepancies smaller than 8% for scintillometer and EC measurements made over different crops.

Studies of scintillometer applicability in the urban environment include those of Kanda et al. (1997) where measurements were made over a densely built-up district of Tokyo, followed by observations made over densely built-up neighborhood (Kanda et al., 2002). They found modified versions of MOS equations that led to good agreement with EC heat fluxes measured at the same height and location. Disagreement values were lower than 10%.

Mestayer et al. (2005) and Lagouarde et al. (2006) described the use of large-aperture scintillometers over Marseille as part of the ESCOMPTE project. The instruments were operated over the city center and along three different paths. They used friction velocities u_* determined from a co-located EC system. Sensible heat flux inter-comparisons were successful with disagreement lower than 10%.

Another example is the study of Salmond et al. (2003), who developed a modified version of MOS equations based upon the environmental characteristics of the city of

Basel, Switzerland. This was done as part of the Urban Boundary Layer Experiment (BUBBLE) conducted in the summer of 2002. This work was later detailed in Roth et al. (2006). Empirical fits were developed by comparing SAS data against sonic anemometer measurements over rooftop and across the top of a canyon. The process is based on comparing dissipation rate calculations given that they provide a means of comparison that is independent from MOS. As expected, better agreement was found over rooftops with variability in the order of 10% whereas over the canyon top the variability was in the order of 40%. They highlighted that larger disagreement over the canyon top was possibly caused by contributions from canyon walls that EC instruments were unable to capture.

These results are encouraging. With the exception of the canyon top measurements documented by Roth et al. (2006), all these examples fall within the 10-20% range of agreement found by Thiermann and Grassl (1992) over a homogeneous surface. They indicate that scintillometer measurements are indeed possible in the urban environment under certain weather conditions and after some considerations that include the modification of MOS expressions.

2.3. The Urban Boundary Layer.

2.3.1. General description.

Urban environments are areas of the surface of the earth modified by humans, and are characterized by very large values of roughness due to the presence of large and complex structures. Roughness elements are organized in the form of varied arrangements of buildings, open areas and vegetation. Land-surface properties are highly heterogeneous. Surface types include asphalt, concrete, dirt, metal, and varied vegetated surfaces among others. Heterogeneities that result from the combination of different morphological and physical properties usually peak in the vicinity of downtown areas and tend to decrease away from them. Nevertheless, this can vary largely among urban areas and is not always the case. Together, the large heterogeneity that results from varied morphological and physical properties distinguish urban areas from the relatively flat and homogeneous environments that surround them.

The intricate morphologies and surface types lead to large complexities in atmospheric flows and TT. Variables relevant in the BL that are the most affected include solar radiation and its balance; wind direction and speed; fluxes of heat, momentum and scalars; heat storage/release and in a general sense the heterogeneous distribution of sources and sinks of scalars (Roth, 2000). Three-dimensional gradients become important and the structure of the ABL becomes significantly different when compared to its rural counterpart. It is also important to keep in mind that these modifications do not apply to the urban environment itself but to areas located downwind. Understanding Urban Boundary-Layer (UBL) processes thus has implications in regions that are not only constrained urban areas.

The vertical structure of the ABL over urban areas differs in some aspects with that of the standard ABL. Oke (1976) was the first to propose a simple classification that consisted of the urban canopy (UC) and the UBL itself. A concise description is available in Roth (2000). The UBL itself can be subdivided in the urban RSL (URSL), the urban ISL (UISL) and the urban ML (UML). A visual description of the layers that describe the UBL is detailed in Figure 2.14.

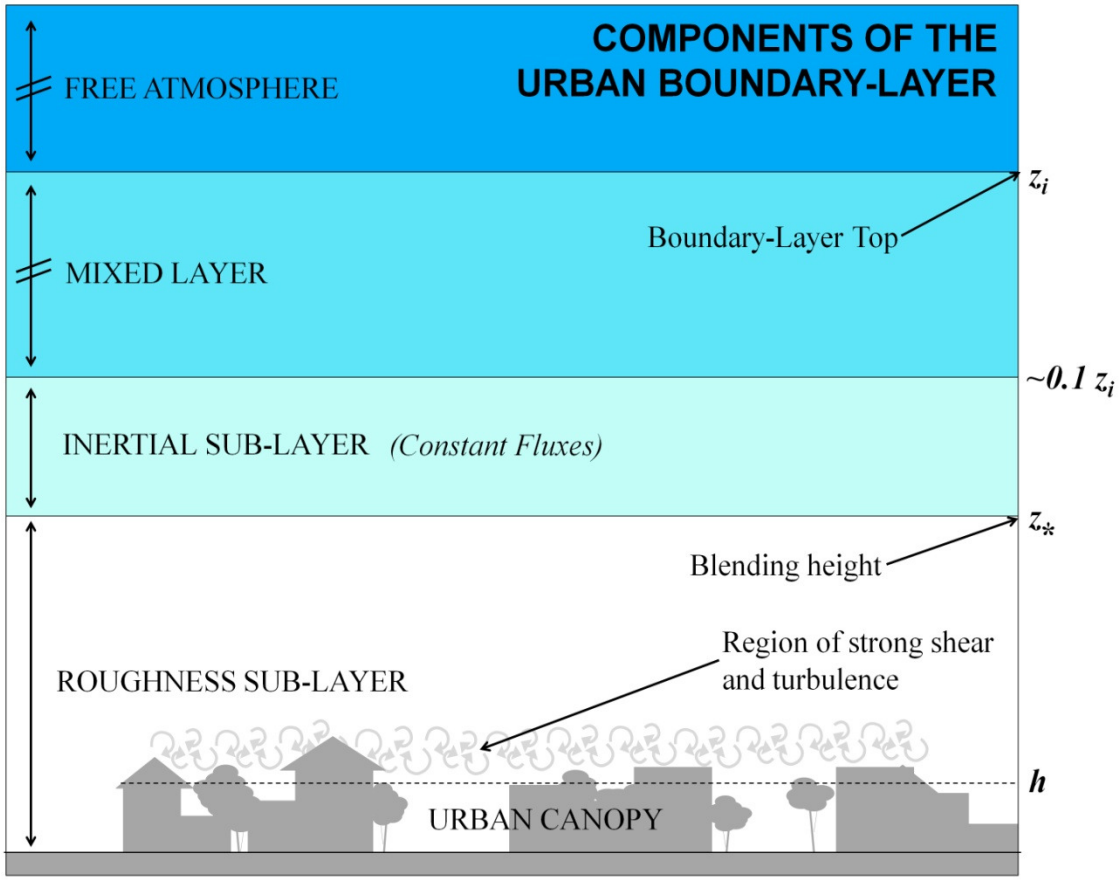

Figure. 2.14 Components of the Urban Boundary Layer after Roth (2000).

The Urban Canopy (UC) is the lowest section of the UBL system. It is defined as the layer of air located at and below the mean height of the buildings and trees h (Glickman, 2000). Its climate is dictated by dynamic and thermal processes highly

affected by the immediate surroundings (Roth, 2000). The most remarkable processes can be summarized into form drag, wake diffusion and the development of highly heterogeneous sources and sinks of heat and momentum. All three processes are determined by building morphology and by surface properties, i.e. building orientation, albedo, emissivity, thermal properties and others. Form drag represents pressure differences across individual roughness elements, and dominates momentum transfer into the surface. Wake diffusion represents mixing generated by turbulent wakes behind individual elements. It mixes heat, momentum and other scalars in an efficient manner (Roth, 2000). The heterogeneous distribution of sources and sinks of heat and momentum is a product of differential heating/cooling of sunlit/shaded surfaces, as well as the diverse distribution of surface types and surface moisture. The top of the UC is characterized by a strong shear layer where the mean kinetic energy available above the canopy is converted into turbulence kinetic energy (TKE) and leads to strong turbulence intensities (Roth, 2000).

The URSL includes the UC and extends from the ground to the blending height z_*. Influenced by individual roughness elements, flow inside the URSL has a fully three-dimensional structure. This leads to dissimilar TT of heat and momentum (Roth and Oke, 1995) and local-scale advection is important (Roth, 2000). The depth of the URSL z_* typically extends over several tens of meters in the vertical (Rotach, 1999). It can be estimated based on the height of the buildings h and usually varies between $2h$ in closely spaced canopies and $5h$ over rough vegetated canopies (Roth, 2000). It can be also estimated with the roughness length z_0 (Tennekes, 1973) and in some cases with the zero-plane displacement height d_0 (Garratt, 1980 and Raupach and Legg, 1984); where d_0 is a length introduced in rough environments to account for the vertical displacement

of the logarithmic wind profile due to the effects of canopies detailed in section 2.3.2. The blending height is also a function of stability and becomes larger during unstable stratification (Garratt, 1980). The horizontally-homogeneous UISL or Constant-Flux Layer (CFL) lays above the URSL. It is similar to the standard SL and therefore MOS is applicable.

Three different scales can be identified when studying an urban environment. A sketch showing these scales is available in Figure 2.15, after Grimmond (2006).

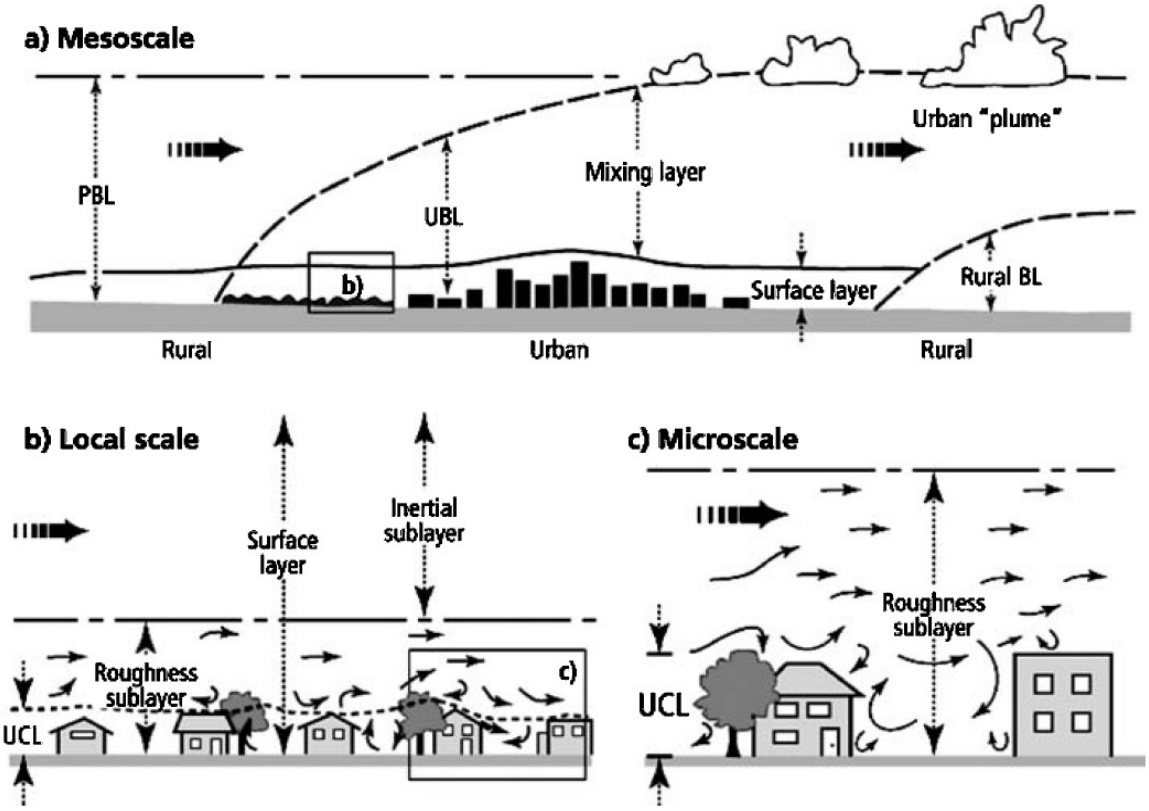

Figure. 2.15. Three different scales used to study the urban atmosphere (Grimmond, 2006).

The largest scale in Figure 2.15. is the mesoscale, where urban areas appear as an increase in roughness, different thermal properties and sources of pollutants. These

differences produce changes in the structure of the ABL that are advected downwind, thus urban areas affect regions in the mesoscale that are several times larger than the urban area itself, depending on the characteristics of the flow and stability.

On the local scale, three-dimensional structures become important. The distribution of houses and vegetation determine the complex circulations that occur around them. Interactions between the UC, URSL and between the URSL and the ISL become important. Local scales also consider the ISL but focus on the UC.

The microscale is the smallest scale and where the present analysis concentrates. This scale permits to investigate the UC and the shear layer near its top. The three-dimensional representation of the UC and its circulations become essential.

The research here presented focuses on the microscale but with applications on the mesoscale in mind. It investigates TT of heat in the UC and across the overlying shear layer. It is of particular interest to understand the role of discrete sections of the UC in the TT of sensible heat and how they relate to the integrated role of the UC.

2.3.2. Assumptions that fail in the Urban Roughness Sub-layer.

The URSL is characterized by high heterogeneity, which limits the applicability of well-established relationships derived for the flat and homogeneous SL (Roth, 2000). The ISL, where fluxes are constant and MOS applies, sits above the blending height and is usually located too far from the surface. Below the UISL, the three-dimensional structure of the environment rarely allows to establish a homogeneous fetch. This has motivated the development of footprint models to determine the source of turbulent fluxes (Schmid and Oke, 1990; Schmid, 1994 and Schmid, 2002). These models are

usually functions of stability, wind speed, lateral dispersion, surface roughness and height (Grimmond, 2006).

Local advection is important in the URSL as the sources and sinks of heat, momentum and scalars have complex distributions. Stationarity can be hard to attain (Roth et al., 2006). The presence of a shear layer over the UC produces large turbulence intensities and transient sweeps and ejections that modulate TT (Roth, 2000). Together, these limitations hinder the applicability of micrometeorological theories such as profile methods (Oke 1987) and MOS (Monin and Obukhov, 1954). It should be noted, however, that data calculated using MOS has shown reasonable agreement with reliable measurements made in urban environments under certain conditions (see section 2.2.3). This is the case of some scintillometer studies

Another consideration is the vertical displacement of the logarithmic wind profile. In canopies where roughness elements are packed together (e.g. some urban and forest canopies) they act like a displaced ground surface (Stensrud, 2007). A new parameter, the zero-plane displacement height d_0, is usually introduced to account for this displacement. The use of d_0 allows the establishment of an effective height z' that allows the application of SL theories such as MOS above the canopy when possible, where:

$$z' = z - d_0 \tag{2.44}$$

The effects of d_0 on the SL logarithmic wind profile are illustrated in Figure 2.16. Wind vectors are indicated with red arrows. Velocities are represented with arrow length. Surface features are indicated with gray shading.

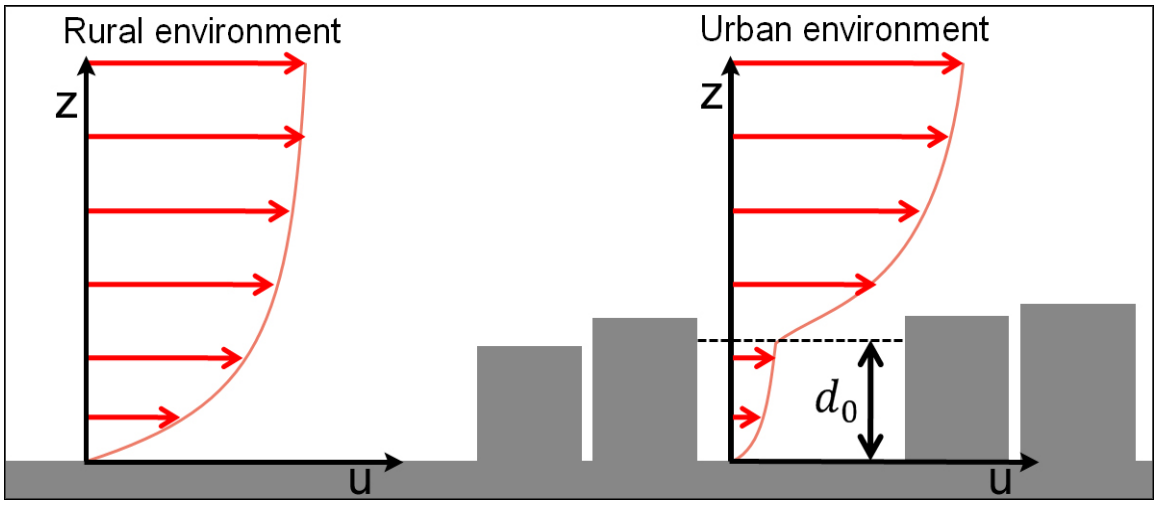

Figure 2.16. Schematic example of wind profiles over a flat rural environment (left) and over an urban environment (right). d_0 is describes the vertical displacement of the base of the logarithmic wind profile.

Kaimal and Finnigan (1994) suggested that a rough approximation to $\frac{d_0}{h} \sim 0.25$. This is valid in homogeneous canopies but can vary largely in the complex urban environment. Grimmond and Oke (1999) consider $\frac{d_0}{h} \sim 0.7$ as appropriate.

The determination of values for d_0 in the urban environment is a complex task. It depends on the characteristics of the urban canopy structure (Grimmond and Oke, 1999; Roth, 2000), and is generally attained via morphometric methods (detailed in Chapter 5). Appropriate determination of d_0 is of great importance since MOS (i.e. when applicable) relies on functions of z'/L. Lagouarde et al (2006) showed that the determination of d_0 and its variability along the optical path is indeed crucial to attain reliable scintillometer measurements in the URSL.

2.4. Numerical representation of the Urban Boundary Layer.

Stensrud (2007) presents a comprehensive overview of Numerical Weather Prediction (NWP) models and the various types of parameterizations used to represent physical processes. From these, Urban Canopy Models (UCM) are of special interest here. Unfortunately, most NWP models that operate on the mesoscale represent urban areas in very simple ways (Craig and Bornstein, 2002; Rotach et al., 2005), partly due to computational limitations but also due to limited knowledge of atmospheric processes in urban environment and a limited number of urban models available. This section introduces the approaches used to model urban areas and then focuses on the Harman-Barlow-Belcher parameterization (Harman et al. 2004), analyzed in the context of the urban campaign results in Chapter 6.

A NWP model is a numerical algorithm designed to resolve the conservation equations numerically over limited periods of time. They are excellent tools for short and medium range forecasts, but also for climate studies. NWP models require initial and lateral conditions provided by grids constructed using in situ data and fields derived from remote sensing platforms. Since all atmospheric processes cannot be resolved explicitly, some need to be represented with parameterizations, which are simplified and idealized representation of complex physical processes. Yet simple, they are designed to retain the essence of the processes represented. They are important because they strongly affect model output through indirect interactions via changes in model variables (Stensrud, 2007). The types available in NWP models usually resolve processes such as radiation, land-surface-atmosphere interactions, soil interactions, the ABL, turbulence, convection, microphysics and orographic drag (Stensrud, 2007). The parameterization of TT in the SL is of special interest, since it establishes the connection between the surface and the

atmosphere, and the physical processes behind this connection differ between standard SL and those over urban areas.

2.4.1. The urban street canyon.

The urban street canyon or urban canyon is considered as the generic unit of an urban surface (Núñez and Oke, 1977) and has been used as the basis for several studies (e.g. Johnson et al., 1991; Mills, 1993; Sakakibara, 1996; Arnfield and Gimmond, 1998; Masson, 2000; Kusaka et al., 2001; Martilli et al., 2002; Barlow et al., 2004; Harman et al., 2004, among others). An urban canyon is the space between two elongated buildings. Four facets are usually considered to represent and urban canyon: the ground or street, the two walls from the buildings and the roof of one of the buildings. This is, of course, a simple representation of an urban area. In reality urban areas have very complex morphologies. An illustration of an urban street canyon is provided in Figure 2.17 after Núñez and Oke (1977). This concept is essential in the modeling of urban areas and will be addressed several times in the following.

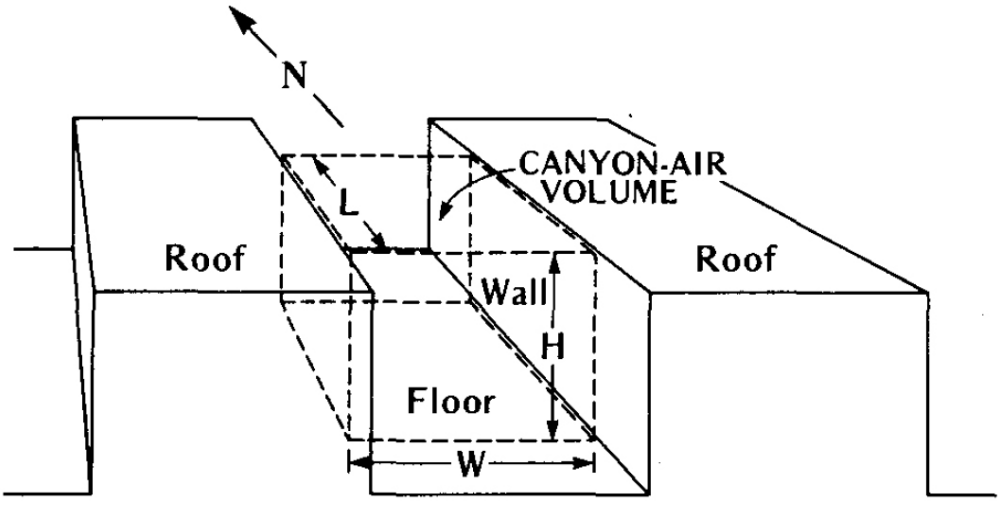

Figure 2.17. Structure of an urban canyon after Núñez and Oke (1977). Note that the north does not necesarilly points along the canyon. In this study the north pointed across it.

2.4.2. Urban modeling approaches.

The way urban areas are represented in mesoscale models can be organized into three approaches listed in order of increasing complexity: Slab Models, Single-Layer Models and Multi-Layer Models (Dupont et al. 2004, 2006). Figure 2.18 describes these approaches and the main components of their land-surface models and input parameters.

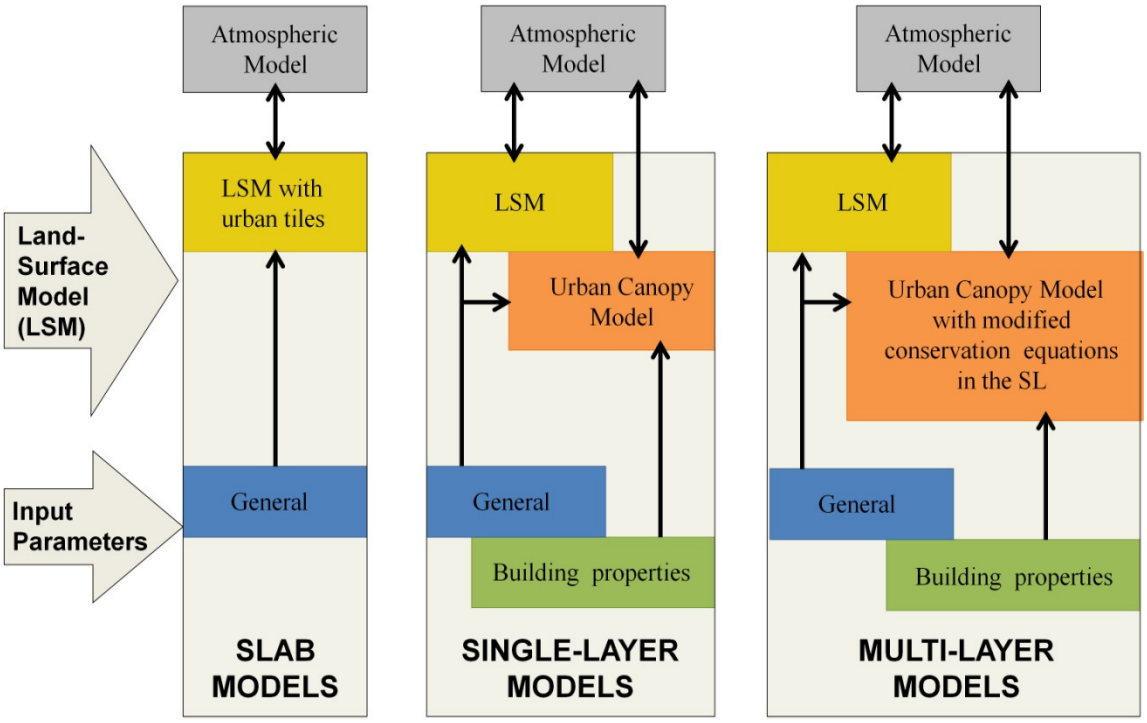

Figure. 2.18. Classification of urban parameterization approaches used in mesoscale models.

A schematic representation of the differences between the three types of approaches is provided in Figure 2.19 in which TT transfer is represented using resistance networks (Stensrud, 2007) after Kuzaka et al. (2001).

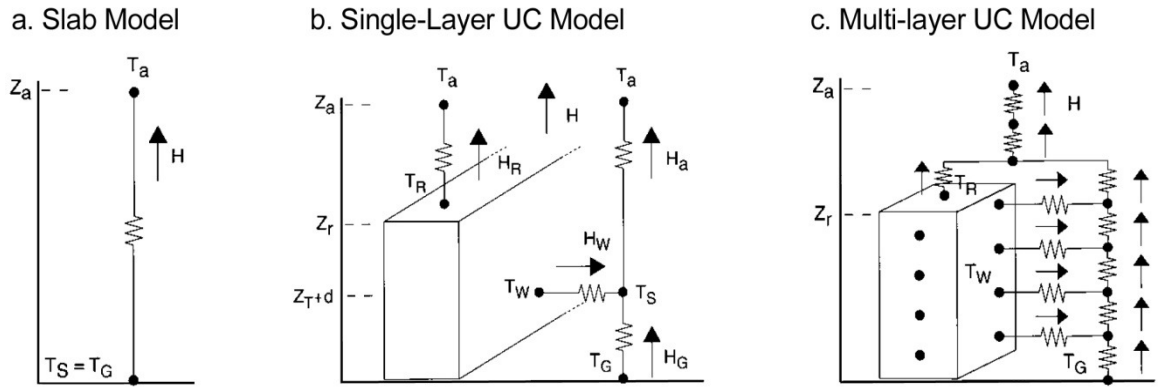

Figure. 2.19. Example of the parameterization of the TT of heat in the urban canopy via three different approaches, reformatted after Kuzaka et al. (2001).

Slab Models are the most popular due to their simplicity and low computational cost. They are thus used in many atmospheric models to represent land-surface-atmosphere interactions (Seaman et al., 1989; Menut, 1997; Chen and Dudhia, 2001; Kusaka et al., 2001, Masson, 2000). Slab Model descriptions are available in Martilli et al., 2002, Dupont et al., 2004 and Dupont et al., 2006. Urban areas in Slab Models are described as soil types with high values of roughness (i.e. one to a few meters, Wieringa, 1993 and Petersen, 1997) and reduced vegetation cover. TT in the SL of the models is described with MOS, which is sometimes a very coarse approximation since constant fluxes, stationarity and homogeneity cannot be usually assumed close to the urban surface. These limitations in the representation of urban areas gain importance with the use of higher resolution models. Negative effects include failure in the reproduction of the vertical structure of turbulent fluxes and limitations on the reproduction of the urban heat island effect. The major source of problems is that the sink of momentum is the ground instead of the upper canopy and that modifications of the radiative balance by the UC are ignored (Martilli et al., 2002). Improvements in the representation of urban areas without adding too much computational cost have been made. Some represent urban areas as solid canopies of concrete (Best, 2005). Roughness length parameterization

(Rotach, 1999) and exploitation of the concept of thermal roughness length have also been discussed (De Ridder and Schayes, 1997) but still, important limitations remain (Dupont and Mestayer, 2006).

Single-layer models are next in order of complexity. They provide the atmospheric model with values that represent the entire influence of the UC. Building characteristics such as building height, area densities and ratios are considered. These models parameterize physical processes such as the surface energy balance and turbulent transfer in the UC and provide the atmospheric model with quantities that represent the integrated effect of the canopy. Limitations arise when fine grids (i.e. spacing smaller than 1 kilometer) are used, since three-dimensional gradients become important (Dupont and Mestayer, 2006). Furthermore, problems associated with MOS violation are not resolved. Some examples of Single-Layer Models can be found in Masson (2000), Kusaka et al. (2001), Ca et al. (2002), Martilli et al. (2002), Dupont et al. (2004) and Otte et al. (2004). These models are particularly relevant to this study due to the focus on the integrated role of the UC in terms of TT. Accordingly, a couple of examples are provided in the following: the models presented by Masson (2000) and Kusaka et al. (2001).

Masson (2000) presented the Town Energy Budget (TEB) scheme, a single-layer urban parameterization. The scheme made as general as possible to increase its applicability into different urban environments around the world. Being a single-layer model, the TEB provides the atmospheric model with information from a constant flux layer in the lowest boundary. Energy budgets are considered for roofs, roads and walls and assumes an isotropic array of surfaces. TT is parameterized using the bulk aerodynamic approach (Garratt, 1992) and the concept of resistances (Stensrud, 2007). A summary is presented in Figure 2.20.

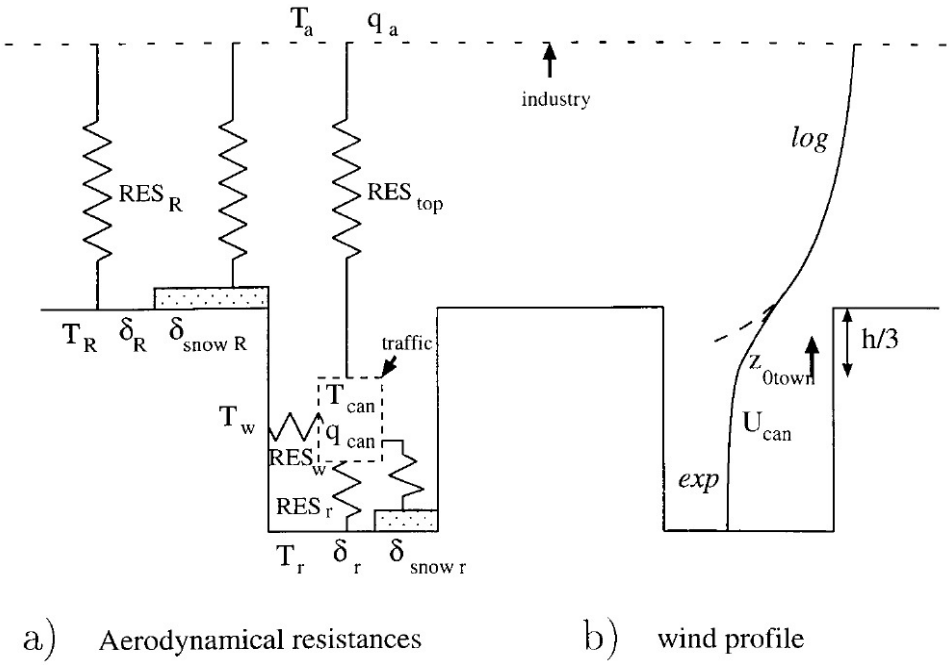

Figure. 2.20. Parameterization of the TT the urban canopy from Masson (2000) showing aerodynamic resistances and wind profiles.

Exchange coefficients are calculated with empirical parameterizations. Turbulent fluxes of sensible heat from rooftops and canyon tops are obtained using classical ABL laws. Inside the canyon, the model also considers the effects from sensible and latent heat fluxes produced by building walls, traffic and industry. Resistances are calculated based on Mascart et al. (1995).

Another good example of a single-layer approach is the model developed by Kusaka et al. (2001). In this model, the influence of urban geometry is considered via a parameterization of the influence of street canyons, where the surface temperature and heat fluxes from roofs, walls and roads is estimated. It also includes the effects of shadowing from buildings and reflection of radiation. The authors compared the model against multi-layer and slab models. Their simulations agreed well with observations and results from the multi-layer model. They agreed in that the rooftops were the hottest

surfaces during daytime and the coolest after midnight, and both models produced similar diurnal cycles of the energy budget.

Multi-layer models are the most accurate in the representation of TT inside urban areas. Yet computationally expensive, these models are suitable and recommended for fine resolutions. Multi-layer models divide the UC into several layers. Fluxes of heat, momentum and moisture are explicitly resolved using modified versions of the conservation equations. These contain extra terms that describe the sources and sinks associated with buildings and vegetated areas, and the surface energy balance is usually modified (Martilli et al, 2002). Implementation of multi-layer models in mesoscale models has resulted in improved model output. Dupont et al. (2004, 2006) demonstrated that better agreement was attained between model results and observations once an urbanized version of MM5 was used. Specific areas of improvement included the representation of the nocturnal heat island; the representation of the effects of individual elements on flow characteristics; the representation of a decrease in wind velocities over the UC; and the development of a layer of cool air inside the canopy during daytime from the shading effects of buildings and trees. Urbanized mesoscale models also tend to produce deeper boundary layers, which is observed in reality. Some examples can be found in Uno et al. (1989), Brown (2000), Ca et al. (2002), Martilli et al. (2002), Lacser and Otte (2004), Dupont et al. (2004) and Dupont and Mestayer (2006).

An example of a multi-layer model is the Urban Canopy Parameterization (UCP) implemented into MM5 by Otte et al. (2004), and tested over Philadelphia, Pennsylvania. Their results showed closer agreement with observations when compared against single-layer simulations. The use of several layers in the UC accounts for the dynamic effects of the urban environment. Since the lowest level of the atmospheric model corresponds to

the ground, d_0 does not need to be parameterized. TKE equations were modified to account for the area-averaged effects of the urban elements and were oriented for an ABL parameterization scheme that considers a prognostic equation for TKE. They used the Gayno-Seaman ABL Parameterization scheme (e.g. Shafran et al., 2000). The fraction of urban area in a grid cell is partitioned into the total area represented by canyons (i.e. street level between buildings) and roofs. It is assumed that buildings affect the flow and that they do not take any volume within the grid cell. The treatment of the thermodynamics was more simple and consisted of using simplified approximations in the temperature tendency equations and in the ground surface energy budget. Different approximations were used for in-canopy layers versus those located above it.

An example of the representation of the UC within a grid cell is presented in Figure 2.21 after Brown and Williams (1998), followed by an example of the representation of physical interactions in the UC in Figure 2.22. The latter was constructed based on the SMU-2 Canopy Parameterization implemented in the MM5 model (Dupont et al., 2004).

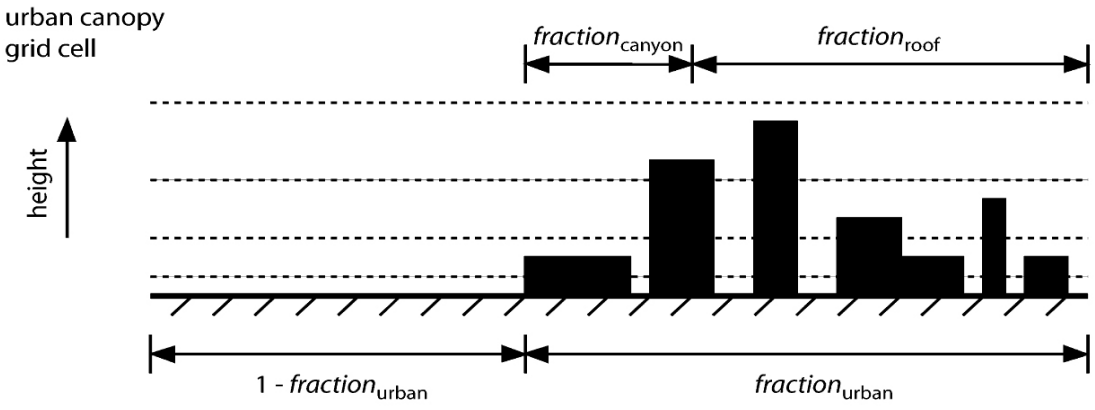

Figure. 2.21. Schematic illustration of the side view of an urban grid cell adapted from Brown and Williams (1998).

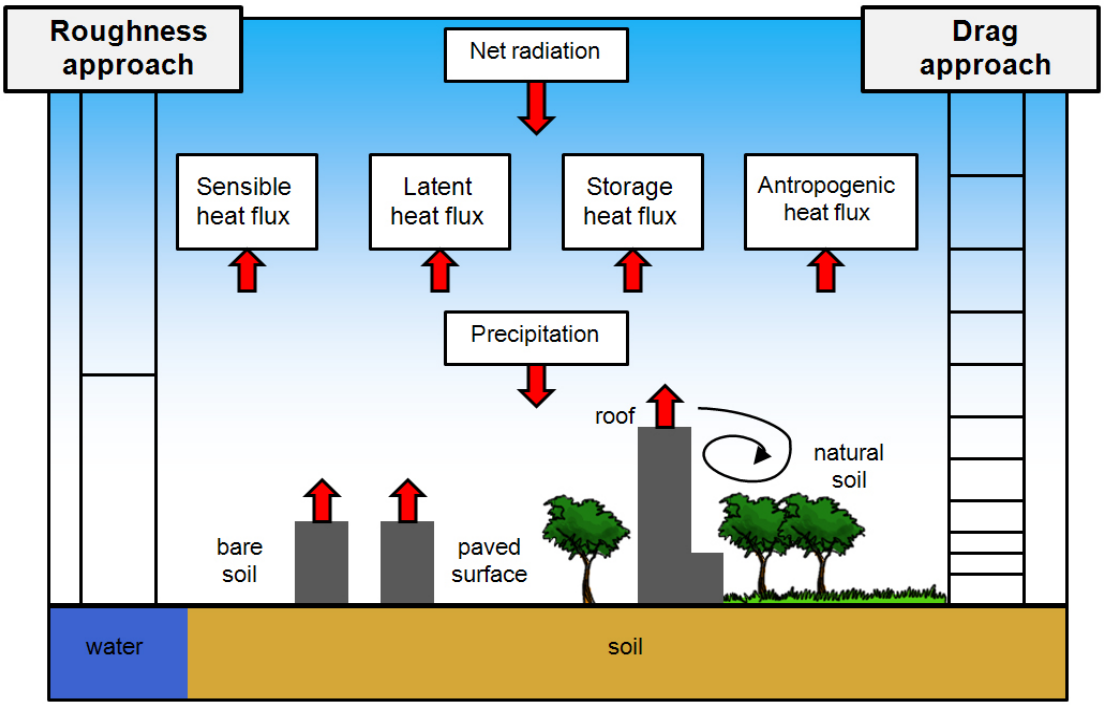

Figure. 2.22. Schematic comparison of the Simple-layer (Roughness approach) and Multi-layer (Drag approach) models, reformatted after Dupont et al. (2004).

One of the most recent comprehensive efforts to represent urban areas in mesoscale models is available in Chen et al. (2011). The authors developed an urban modeling system coupled with the Weather Research and Forecasting model (WRF). The coupling was made through the parameter urban fraction. For a given grid cell, the Noah LSM (Chen et al., 1996; Chen and Dudhia, 2001) provides surface fluxes and temperature for the vegetated components of urban areas and the UCM for the anthropogenic components. The authors also incorporated the three available approaches: a slab model, the single-layer UCM developed by Kusaka et al. (2001) and Kusaka and Kimura (2004); and a multi-layer UCM presented by Martilli et al. (2002).

Some additional examples of efforts on the development and/or validation of urban parameterizations include the work of Taha (1999), Taha and Bornstein (1999),

Dupont et al. (2004), Harman et al. (2004), Roulet et al. (2005), Dupont et al. (2006), Lemonsu et al. (2006), Liu et al. (2006), Holt and Pullen (2007), Lee and Park (2008), Taha (2008a,b) and Porson and Harman (2009).

It is evident that an increase in complexity and in the representation of physical processes in urban parameterizations improves mesoscale model results. Yet, these parameterizations are computationally expensive. Even when there is still large room for improvement, it is essential to work on finding a balance between accuracy and computational requirements. From the parameterizations presented, the Harman-Barlow-Belcher Model for scalar fluxes (Harman et al., 2004) is described with more detail in the following and inter-compared with the data collected during the ILREUM urban campaign in Chapter 6. This parameterization was selected based on the geometrical resemblance with the geometry of the ILREUM measurement site.

2.4.3. The Harman-Barlow-Belcher Model.

Harman et al. (2004) developed a model that parameterizes the TT of scalars in urban street canyons. The model was validated with data collected in wind tunnel experiments (Barlow et al. 2004) and good agreement was found. This particular model was of special interest due to the geometrical resemblance between one of the studied cases and the urban canyon measured in this study (i.e. $h/W = 0.25$). Model output is compared with the results from the urban campaign in Chapter 6.

The Harman-Barlow-Belcher model emphasizes the geometrical dependence of TT under cross-canopy flow conditions. The model considers the urban area as a series of infinitely long canyons oriented normally to the reference flow $\overline{U}$. Building height is

considered uniform and the roofs flat. TT transfer is represented two-dimensionally where a canyon cross-section is divided into four components or facets: upstream wall, ground, downstream wall and downstream roof as shown in Figure 2.23.

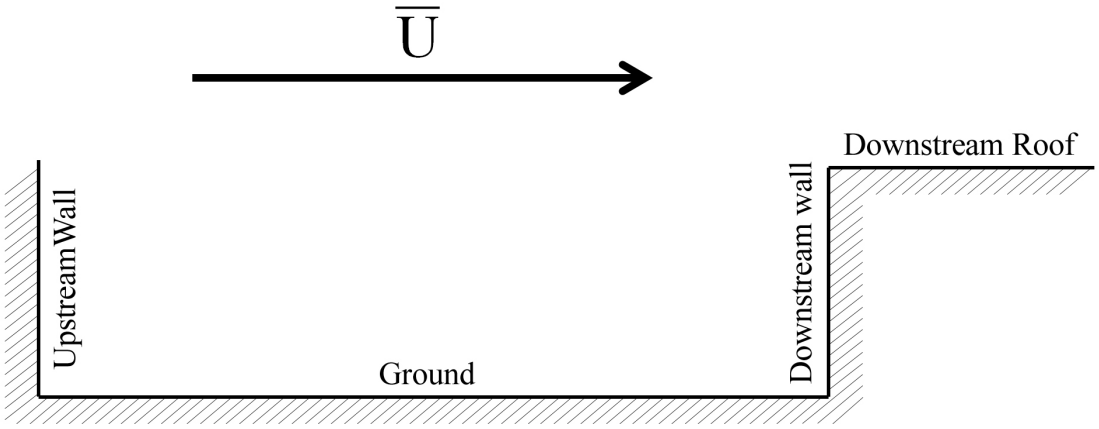

Figure 2.23. Schematic representation of the street canyon modeled by Harman et al. (2004).

The model represents different canyon height-to-width ratios h/W and was tested for four geometries that ranged from narrow $(h/W = 2)$ to wide $(h/W = 0.25)$ canyons. The latter coincides to the geometry of the ILREUM urban campaign site (Chapter 5). Flow and TT is urban canyons highly sensitive to canyon width W. The size of the recirculation region L_r that forms in urban canyons under normal flow conditions matters, especially how it relates to W. The relationship between L_r and W leads to the identification of three different flow regimes in urban canyons. These are summarized in Figure 2.24 after Oke (1987) and Harman et al. (2004). The isolated roughness regime prevails in canyons where $L_r < W$ (Figure 2.24a). It is characterized by a region of ventilation in the downwind end of the canyon that reaches the canyon floor. The wake interference flow regime occurs when $L_r/2 < W < L_r$ (Figure 2.24b) and is characterized by a ventilation region that does not reach the ground. When the buildings

are too close together the skimming flow regime occurs (Figure 2.24c). In this case in-canyon flow is mostly decoupled from above-canyon flow, and ventilation near canyon top is small.

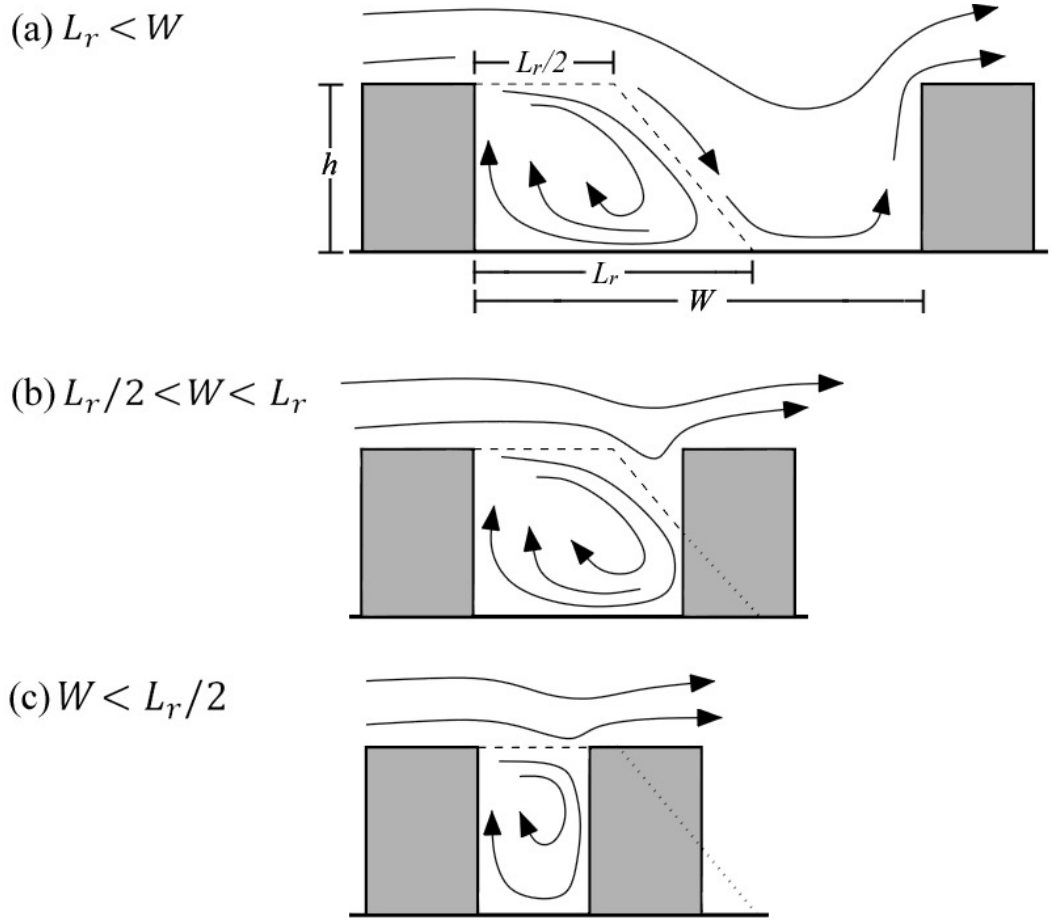

Figure 2.24. Schematics of the streamlines for three flow regimes: (a) isolated roughness, (b) wake interference and (c) skimming flow, reformatted after Oke (1987) and Harman et al. (2004).

L_r can be related to building height h. Studies have found that L_r varies between $2h$ and $3.5h$ (Oke, 1987; Castro and Robins, 1977 and Okamoto et al., 1993). Data from the urban campaign agreed with those of Okamoto et al., 1993 in that L_r is closest to $3.5h$, but even larger values were observed.

As detailed in Stensrud (2007), a common approach to represent TT in the SL is to parameterize it in terms of resistance networks. Harman et al. (2004) divided the parameterization into two cases: one for a canyon with ventilation (Figure 2.25a) and one for a canyon with skimming flow (Figure 2.25b).

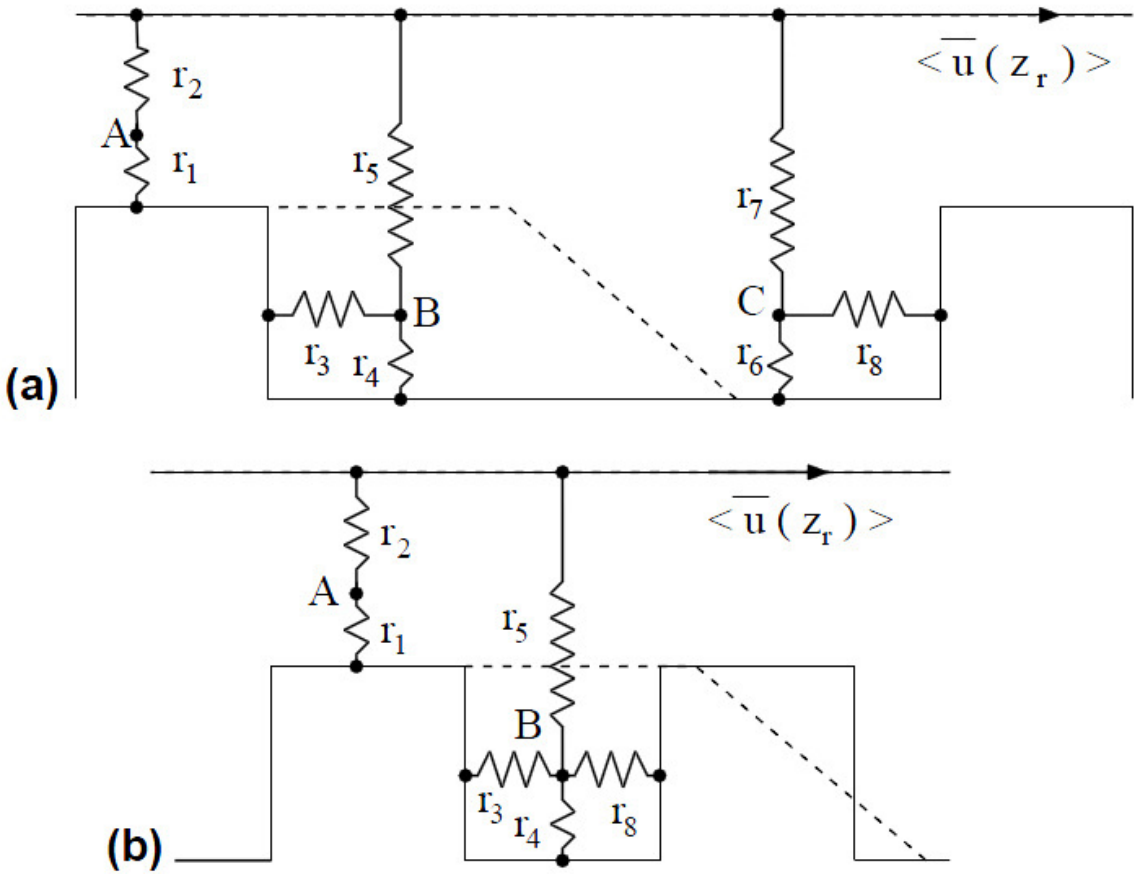

Figure 2.25. Resistance network used to parameterize SHFX Harman et al. (2004) in two different canyons.

2.5. Context of the study.

2.5.1. Open questions.

There are two sets of general questions given the two topics of interest. Regarding TT in the urban environment, the main questions are "*What is the integrated role of the UC on the TT of heat with the URSL?*", "*What are the roles of the individual components of the UC*" and "*How do the individual components tie to the integrated role"*? On the other hand, the main questions regarding the use of scintillometers over the highly heterogeneous urban canopy are "*Are scintillometer reliable means to sample the highly heterogeneous urban canopy? Are scintillometer skill evaluation campaigns always necessary before using one of these instruments for data collection? Can a pragmatical approach to correct scintillometer fluxes be developed? What approach can be used and what are the details behind it?*"

2.5.2. ILREUM: the opportunity.

The NSF Career Award 'Innovative Laboratory for the Research and Education in Urban Meteorology' (ILREUM) was initiated in 2007. This project was motivated, among other goals, by an interest in understanding the integrated effects of the urban canopy on the turbulent exchange of heat and momentum. One specific interest of ILREUM was to measure turbulence properties within the urban RSL by the means of a comprehensive and prolonged observational campaign. Long-lasting measurements were planned strategically with the goal of addressing temporal representativeness limitations on data available that exist from the briefness of previous urban campaigns. Available results are also limited in space due to the highly heterogeneous nature of urban areas, which poses a spatial representativeness issue. Overcoming this issue is, however, a

different and more complex problem. One of the possible solutions considered in ILREUM, was to complement strategically positioned sonic anemometer measurements with those from a platform designed to provide quantities integrated in space. It was here that the idea of using scintillometers emerged. Given their documented skill when operated over heterogeneous surfaces, scintillometers were considered as plausible means to collect spatially-integrated TT data and thus address the spatial representativeness issue. Since discrepancies regarding scintillometer skill over heterogeneous surfaces has been described in some studies, it was also considered necessary to evaluate scintillometer skill under such level of heterogeneity. Given the motivation overlap and opportunity, the present work arose as an excellent means to address some these two topics, and was thus carried out with the support of ILREUM.

2.5.3. Approach and rationale.

The approach to attain the research objectives was based on observations. Turbulent fluxes of heat were measured using several sonic anemometers and a small aperture scintillometer. Sonic anemometers were placed at strategic locations to measure the behavior of TT in different sections of the sampling domains. The scintillometer was used to measure the integrated role of the domain in terms of TT.

The measurements were organized in three field campaigns. The core urban campaign was carried out in and above the UC, but data were also collected over a flat and homogeneous environment (i.e. or also referred to as 'suburban' campaigns, see Chapter 4 for details) to evaluate and calibrate the performance of the scintillometer under conditions where MOS applies. The distance between the core urban campaign and the suburban ones was only six kilometers. The distance was kept short to collect

measurements in regions characterized by similar climates and whose differences could be attributed mostly to urban effects. The main goal of these campaigns was, however, to evaluate and calibrate the measurements made with the scintillometer so they could be relied on once made over the urban environment. These campaigns were also planned to explore alternative methods to calibrate scintillometer data, and were successful in the determination of a novel calibration approach that should increase the confidence in future scintillometer measurements.

The core campaign was carried out in and over an urban street canyon located in the campus of the University of Oklahoma, in the city of Norman, Oklahoma. The campaign lasted a little over 13 months. The prolonged duration was planned to address temporal representativeness limitations that arose from the briefness of previous campaigns. Spatial representativeness issues were addressed by measuring the integrated role of the canopy on TT with the scintillometer. Comparisons between sonic anemometer and scintillometer measurements was planned to establish the connections between the role of individual sections of the canopy on the integrated effect in terms of turbulent transfer between the urban canopy and the RSL. An additional goal of the campaign was to evaluate the performance of the scintillometer in the heterogeneous RSL, and to gain more insight regarding the conditions in which the data can be relied upon when the instrument is operated inside the RSL.

3. INSTRUMENTATION.

The core of ILREUM measurements were made with the SCINTEC SLS20 displaced-beam small aperture scintillometer (SLS) and with several RMYoung-81000 and CSAT3 Campbell Scientific SA. Additional measurements considered for the analysis included data from the Norman MESONET site. General information about these platforms is provided in the following.

3.1. The sonic anemometers.

SA are electronic instruments designed to measure high-resolution velocities based on deviation from the theoretical speed of sound in a media. They calculate the time that it takes a sound wave to travel from an emitter to a receiver that are generally separated by a few centimeters. Observations are generally made at frequencies in the order of 10 and 20 Hz, but can be as high as 60 Hz (Campbell Scientific, 2010). The high measurement frequency makes the use of data loggers a requirement.

SA can be two- and three-dimensional. The latter are of particular interest when investigating the vertical transfer of heat. Three-dimensional SA consist of three emitters and three receivers that allow to measure three orthogonal wind components. Temperature can also be retrieved, yet the instruments are precise on measuring temperature fluctuations but not the value of temperature itself: the accuracy for temperature is $\pm 2°C$ for wind speeds that range between 0 and 30 ms^{-1} (R. M. Young Company, 2011). Complementary temperature sensors are recommended if temperature measurements need to be made simultaneously.

Two types of sonic anemometers were used as part of ILREUM. The CSAT3 sonic anemometers were manufactured by Campbell Scientific Inc. (Campbell Scientific,

2010). They operate under wind speeds < 30 ms^{-1} and have offset errors in the order of .02 ms^{-1} for horizontal velocities, .04 ms^{-1} for vertical velocities and 0.025°C for temperature. This anemometer model has the advantage of having reasonable exposure to vertical velocities. Mast interference can be important over a narrow range of angles in the order of ±10°. An photograph of the instrument is presented in Figure 3.1.

Figure 3.1. CSAT3 sonic anemometer. A cup anemometer can be seen in the background.

The RMYoung-81000 Model (R.M. Young Company, 2011) operates under wind speeds < 40 ms^{-1}. It exhibits wind speed errors in the order of ±1% under wind speeds < 30 ms^{-1}. These increase to ±3% as wind speeds increase to 40 ms^{-1}. A limitation of this instrument is the possible mast interference of the instrument shaft with the flow, which is primarily a concern for the vertical velocity. Nevertheless, comparisons against CSAT3

data (Chapter 4) suggest that differences between platforms are small. A photograph of RMYoung is presented in Figure 3.2.

Figure 3.2. RMYoung sonic anemometers, Model 81000, being tested at the School of Meteorology (SoM - OU) Instrumentation Laboratory before the core ILREUM campaign.

3.2. The scintillometer.

The scintillometer used in ILREUM was a displaced-beam small aperture scintillometer manufactured by SCINTEC (SCINTEC AG, 2006). The model used was the SLS20. Figure 3.3. shows a photograph of the receiver operating during a lightning storm. The red laser reflection on the tripod is remarkable. Figure 3.4. shows a photograph of both transmitter and receiver while operated during the core ILREUM campaign. Details are available in sections 2.2.1. and 2.2.2.

Figure 3.3. ILREUM SLS receiver during a lightning storm. April 2010.

Figure 3.4. SLS transmitter (background) and receiver (foreground) collecting data during the core ILREUM campaign.

3.3. The Norman MESONET site.

The Oklahoma MESONET is a network of environmental monitoring stations distributed throughout the state of Oklahoma. It consists of 120 automated stations Mc Pherson et al. (2007). Each site is characterized by sets of instruments located on or near 10-meter-tall towers. The measurements are provided to the public as 5-minute averages. Variables measured at the Norman MESONET site include battery voltage, atmospheric pressure, rainfall since midnight, relative humidity at 1.5 meters, solar radiation, air temperature at 9 and 1.5 meters, wind direction at 10 meters and wind speed at 2 and 10 meters. Soil temperatures under bare soil and under native vegetation are also provided at time as 15-minute averages. A more detailed description of the variables measured is presented in Table 3.1, from McPherson et al. (2007).

Table 3.1. Oklahoma MESONET instrumentation summary from Mc Pherson et al. (2007).

Variable measured	Measurement height	Primary sensor	No. of stations
Relative humidity	1.5 m	Vaisala HMP45C	116
Air temperature	1.5 m	Thermometrics UIM DC95	116
Rainfall	0.6 m	MetOne 380C	116
Pressure	0.75 m	Vaisala PTB202/PTB220	116
Solar radiation	1.5 m	LI-COR LI-200	116
Wind speed and direction	10 m	R. M. Young 5103	116
Soil temperatures under both bare soil and native sod	−10 cm	BetaTHERM 10K3D410	116
Variable measured	**Measurement height**	**Secondary sensor**	**No. of stations**
Air temperature	9.0 m	Thermometrics UIM DC95	100
Wind speed	2.0 m	R. M. Young 3101	116
Soil temperature under bare soil	−5 cm	BetaTHERM 10K3D410	111
Soil temperature under native sod	−5 cm	BetaTHERM 10K3D410	107
Soil temperature under native sod	−30 cm	BetaTHERM 10K3D410	106
Soil moisture	−5 cm	Campbell Scientific 229-L	103
Soil moisture	−25 cm	Campbell Scientific 229-L	101
Soil moisture	−60 cm	Campbell Scientific 229-L	76
Soil moisture	−75 cm*	Campbell Scientific 229-L	37
Variable measured	**Measurement height**	**Experimental sensor**	**No. of stations**
Wind speed	9.0 m	R. M. Young 3101	2
Wind speed	3.5 m	R. M. Young 3101	2
Net radiation	1.5 m	Kipp & Zonen NR LITE	74
Soil heat flux	−5 cm	REBS HFT 3.1	2
Integrated soil temperature	0 to −5 cm	REBS STP	2
Skin temperature	1.5 m	Apogee IRT-P	74
Four-component radiation	1.5 m	Kipp & Zonen CNR1	2
Three-dimensional wind speed	4 m	Campbell Scientific CSAT3	2

MESONET data were used as reference for the analysis of several ILREUM datasets. A photo of the Norman MESONET site is presented in Figure 3.5. A more detailed information about the MESONET can be found in Brock et al. (1995) and Mc Pherson et al. (2007).

Figure 3.5. Norman MESONET site.

4. SCINTILLOMETER SKILL EVALUATION

4.1 Goal and approach.

Several studies have investigated the skill of SLS on the measurement of turbulent fluxes and most have encountered reasonable agreement with simultaneous measurements made using reliable platforms such as SA (see section 2.2.3). Still, differences that require improvement have also been found. In the past, these have been mostly attributed to the MOS empirical approximations used in the SLS algorithm. While proven to be sources of uncertainty, the findings from this study confirmed recent findings described by SLS researchers (Bram Van Kesteren, personal communication, 2011) in that the Hill Refractive Index Spectrum (Hill, 1978) seems to be the largest source of disagreement and ultimately affects calculation of the inner scale of turbulence l_0. Chapter 4 explores the sources of these discrepancies, but focuses on the establishment of a pragmatic approach to correct them. The goal of Chapter 4 is then to present a new method of corrections that improves the measurement of SLS sensible heat fluxes (SHFX) determined upon data from the suburban campaigns and later use them to correct the SLS measurements made in the urban environment, which are addressed in Chapter 5.

The corrections were determined based on SA measurements made near SLS path center (see sections 2.1.2, 3.1 and 3.2). Data were collected in an ideal environment (i.e. flat and homogeneous to fulfill MOS assumptions) and during two three-month long periods. The set of corrections proposed were also tested with the data. Findings suggest that SLS SHFX - and momentum fluxes as well - can be improved by correcting SLS measurements of l_0 and also C_n^2 using polynomial fits. The methodology, findings, corrections and their impact on SLS data are presented in this chapter.

4.2. ILREUM suburban campaigns.

4.2.1. General description.

Two field campaigns were made in a flat and homogeneous environment covered by ten to fifteen-centimeter tall prairie grasses. The site was located only 100 meters away from the Norman MESONET (35°14'10'' N, 97°27'47'' W and 357 mASL) and ~200 km south of the site where the Kansas experiments were carried out (Kaimal and Wyngaard, 1990). The placement was encouraging in terms of inter-comparisons using some MESONET data and in terms of MOS applicability. One limitation, however, was the closeness to the Norman, Oklahoma urban area, which justifies the use of the term 'sub-urban' instead of 'rural'. The closeness to an urban environment could lead to slight deviations from MOS that introduce some uncertainty into the inter-comparison exercise.

The campaigns were conducted during the summers of 2007 (22 June - 13 September) and 2008 (22 May - 5 September). Relatively prolonged campaigns were planned to measure under a broad spectrum of flow and stability regimes. The SLS (section 3.2) was operated over a 100-meter-long east-west oriented path and at two meters above the ground. Several SA were operated along the path: one RMYoung SA during 2007; and one RMYoung and four CSAT-3 SA during 2008. SLS data was recorded at 1-minute intervals whereas sonic anemometer data was recorded at a frequency of 10 Hz. The SLS was powered by a 12V power source and the data were transmitted by cable. SA were powered via solar panels and a battery, and their data were transmitted wirelessly. A map that shows instrument distribution is presented in Figure 4.1, and a photograph of some of the instruments on Figure 4.2.

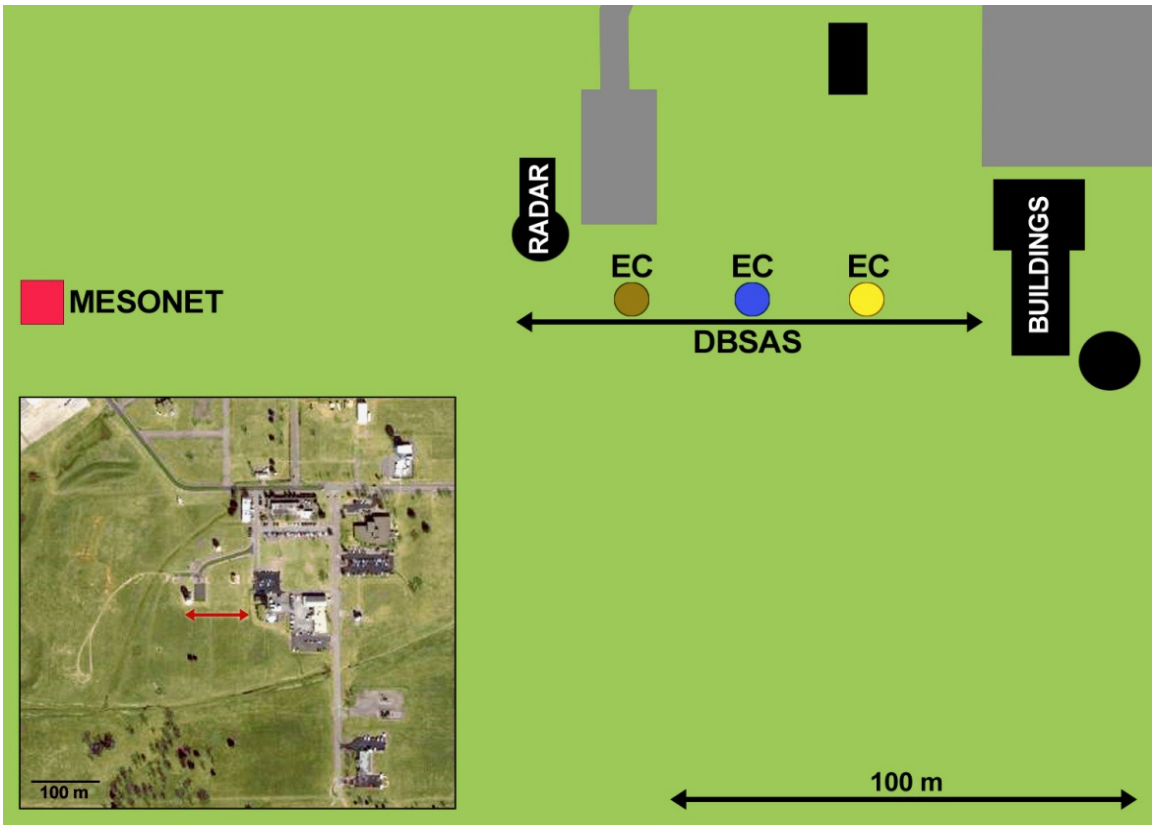

Figure 4.1. Map of the site were both ILREUM sub-urban campaigns were carried out.

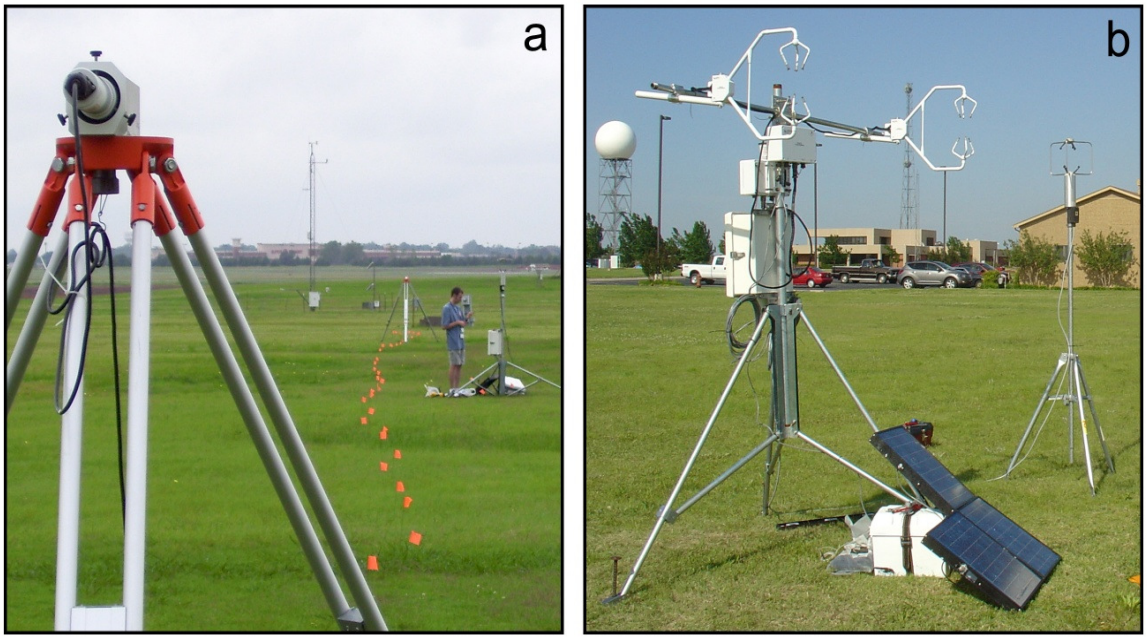

Figure 4.2. Photographs showing some of the instruments operated during the 2007 and 2008 campaigns.

Figure 4.1 shows the location of the SA (colored circles) and the SLS (black arrow). The MESONET is indicated with a red square, buildings in black and paved surfaces in gray. Some remarkable obstacles were located to the east, northeast and northwest of the path, with the best fetch located to the south-southeast. A photograph showing some instrumentation is presented in Figure 4.2. Panel (a), looking west, shows the SLS receiver in the foreground, the RMYoung SA being installed near the center of the path, the SLS transmitter at the end of the path and the MESONET in the background. Panel (b), looking northeast, shows the RMYoung and two CSAT3 SA operated near path center during 2008.

4.2.2. Data and processing.

Datasets available include SLS and SA measurements, and 5-minute averages of different variables collected at the Norman MESONET site. The SLS system provided several variables, some of which consisted of calculations from different parts of the algorithm designed to retrieve turbulent fluxes from scintillations (section 2.2). Turbulent fluxes were calculated for 15-minute intervals using the EC approach (section 2.1.2), so inter-comparisons were made in term of 15-minute averages.

Inter-comparisons were established in terms of l_0 and C_n^2. The goal of comparing data high up the algorithm was to avoid errors associated with MOS. Yet the SLS algorithm (Figure 2.12) was applied backwards to obtain SA C_T^2 and ε from SA measurements u_* and SA θ_* via expressions 2.16, 2.17, 2.29, 2.36 and 2.38 through 2.41. l_0 and C_n^2 were then calculated using 2.28 and 2.35.

4.2.3. Stratification upon wind direction.

Data were stratified upon wind direction WD due to the presence of some obstacles around the measurement site. Obstacle effects on the data were explored by comparing SA WD and WS against 10 m MESONET data. The latter were selected as reference values due to the platform location away from obstacles. Inter-comparison showed that the largest differences occur at angle sectors consistent with the presence of buildings. This is illustrated in Figure 4.3 and backed up by Figure 4.1.

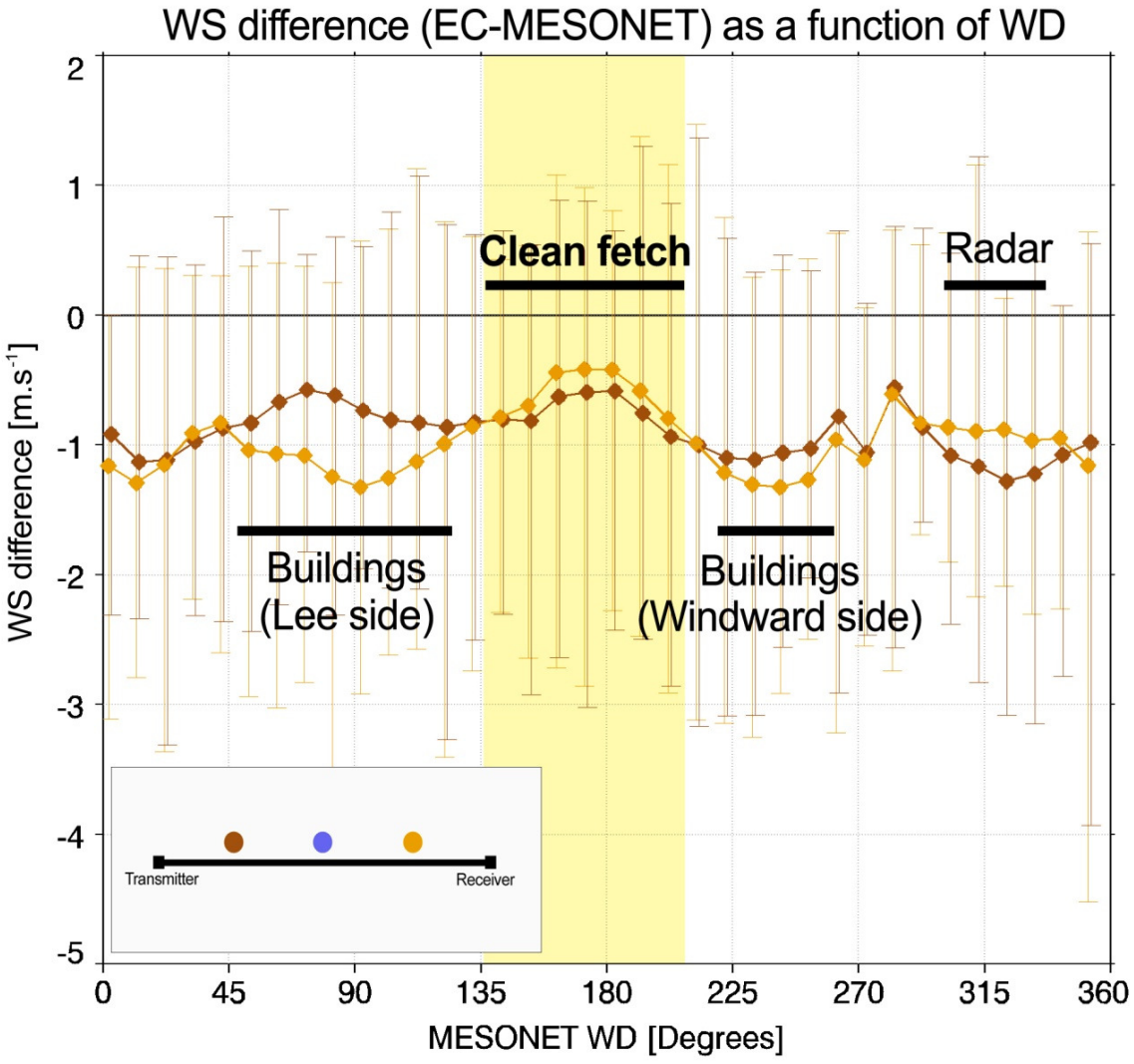

Figure 4.3. WS differences between ILREUM SA and the 10-m MESONET data.

Figure 4.3 shows WS differences ($\mathrm{WS_{SA}} - \mathrm{WS_{MESONET}}$) averaged over 10-degree sectors for two CSAT3 SA located at 25% and 75% of the path. CS3 (yellow) and CS4 (brown) correspond to the easternmost and westernmost locations respectively. Figure 4.3 clearly shows that the smallest WS differences occur during periods with southerly flow. This is consistent with the region characterized by the largest fetch with flat and homogeneous conditions (Figure 4.1). The largest differences are found on the easternmost SA for WD from 50° to 110°. These differences occur when CS3 is located at the lee side of the building complex located to the east-northeast. A second signal is evident for WD between 220° and 260°, consistent with the location of CS3 at the windward side of the complex. A third difference signal can be found on CS4 between 300° and 340°, when the platform is located on the lee of a meteorological radar.

Given the need to concentrate the analysis on conditions close to those ideal for MOS to apply, only measurements that correspond to the cleanest fetch were considered. Any data outside from the 140° to 210° range was excluded.

4.3. Findings.

4.3.1. Selected diurnal cycles.

Diurnal cycles of selected days are presented in Figures 4.4 through 4.10. Top panels indicate sensible heat fluxes (hereafter SHFX) from the SLS (red) and EC (blue). Lines indicate fluxes scaled by WS, faint asterisks indicate non-scaled fluxes. The ratio between SLS and SA SHFX was calculated via:

$$\mathrm{RATIO} = \frac{\mathrm{SHFX_{SLS}}}{\mathrm{SHFX_{SA}}} \times 100\ \% \qquad (4.1)$$

The second panel from the top shows WS in ms^{-1} (light green bars) and WD in degrees (dark green). The third panel from the top shows solar radiation in Wm^{-2} (yellow bars), stability in terms of z/L (black dots) and periods in which rainfall was present (blue bars on top), yet rainfall amounts are not shown. MESONET temperatures in °C are presented in the bottom panel. Soil temperatures at 5 cm under sod are shown in brown, air temperature at 1.5 m in light blue and air temperature at 9 m in dark blue. Vertical temperature differences ($T_{1.5}$-T_9) are shown with a black line and dots. Remarks about some interesting features from these selected cases are discussed in the following.

Figure 4.4 shows a typical day characterized by clear skies and winds slightly weaker than the average (July 26, 2008).

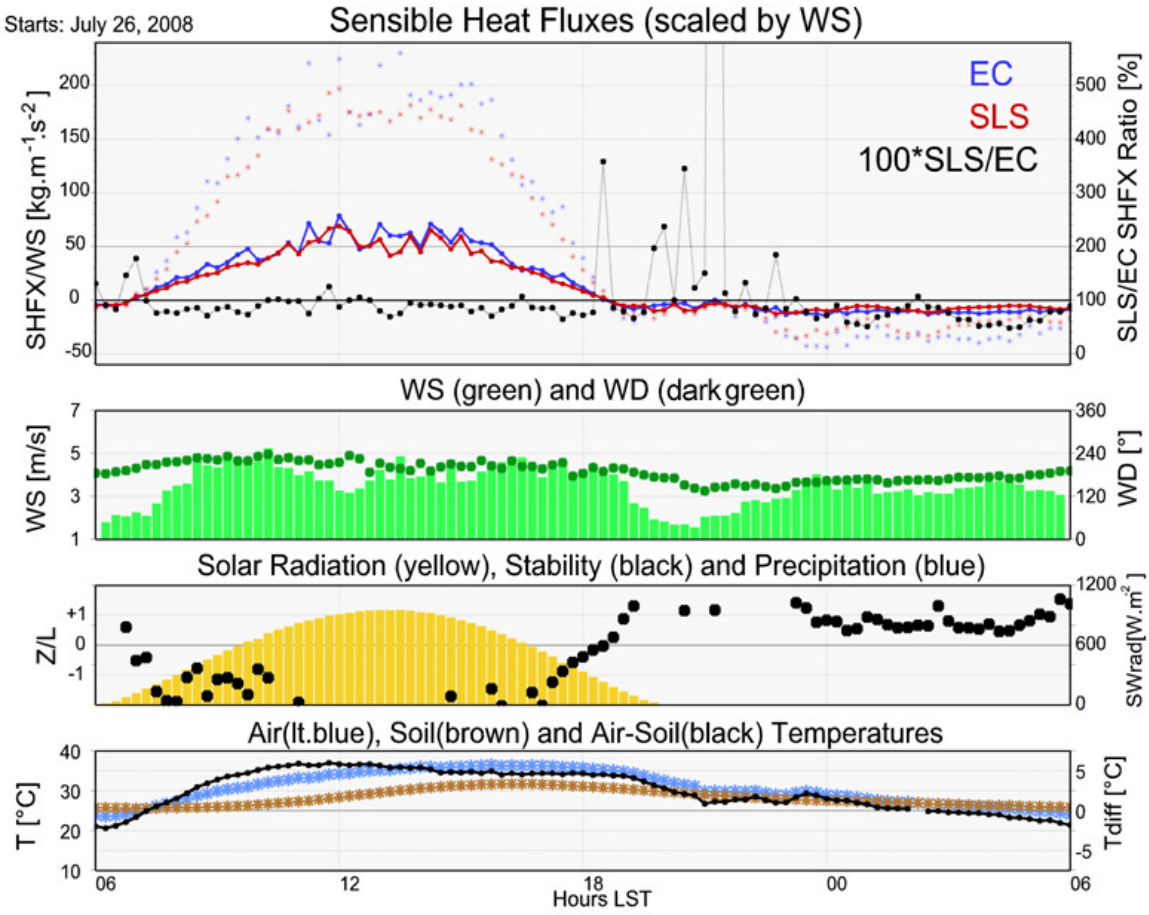

Figure 4.4. July 26, 2008: Typical day with clear skies and relatively weak winds.

The diurnal cycle of SHFX is quite close to the overall average, which will be shown and discussed later on. The SLS underestimated the fluxes over most of the period with some exceptions. The underestimation was slightly below the average, which suggests that the SLS functions better under weaker winds. Overestimation constrained to transition periods due to problems near neutral conditions when scintillations become weak. Another period of overestimation was present during the early night, when high stability and very weak winds were present. Once winds increased in magnitude after 23 LST the SLS underestimated SHFX again. Daytime underestimation was smaller than 20% during this day whereas nighttime underestimation was sometimes as large as 50%. Overestimation can be pretty large (over 400%) but is generally short lived and constrained to periods with weak winds and high stability.

A contrasting case is presented in Figure 4.5 (August 17, 2008), when thick clouds were frequently present. WS were also below the average during most of the period. The SLS did a better job measuring SHFX partly due to the weak winds. During daytime, SLS SHFX were close to SA SHFX and ranged from underestimation in the order of 30% to overestimation in the order of 30%. Underestimation was more frequent. Overestimation during stability transition periods was also present, but more dramatic during the early morning, associated with very weak winds. Fluxes during nighttime were weak and in good agreement between both platforms.

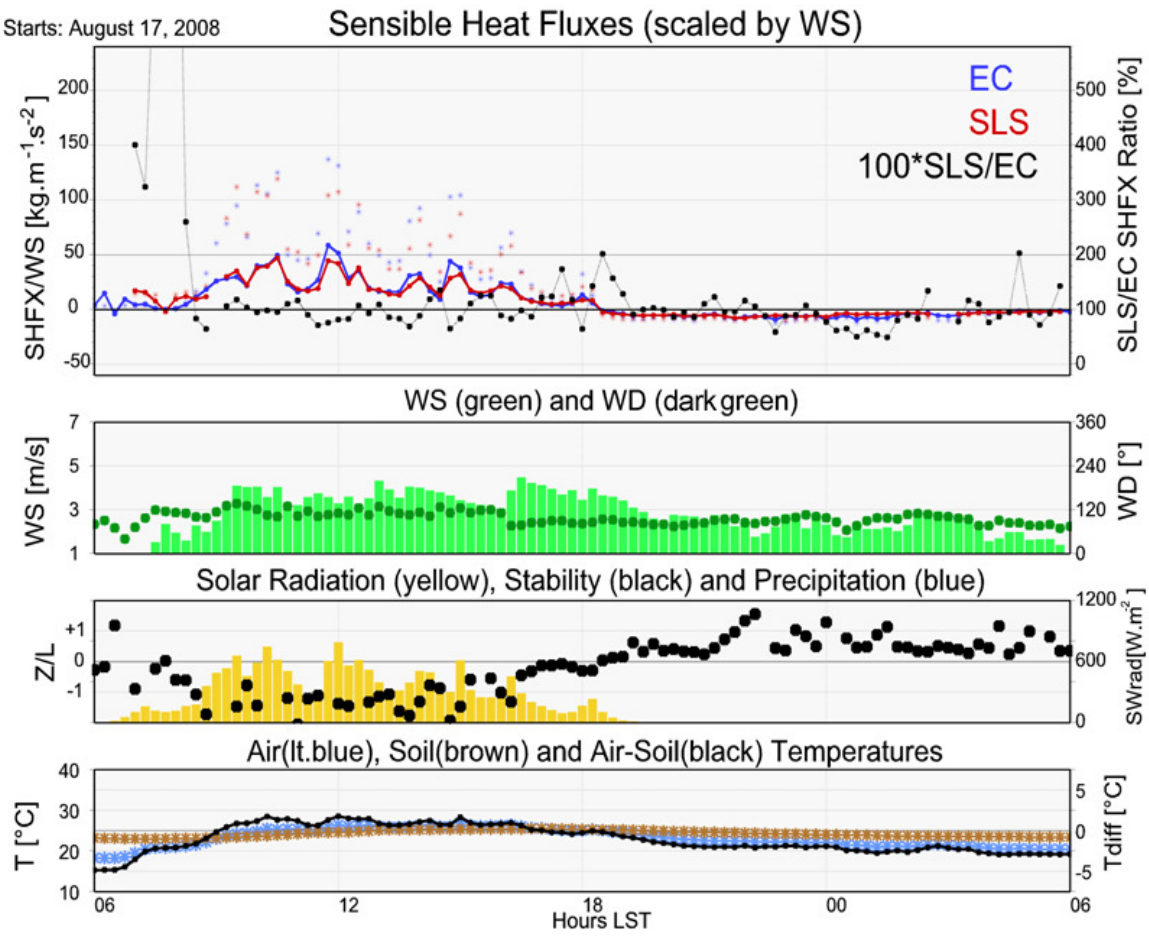

Figure 4.5. August 17, 2008: Cloudy skies and weak winds.

Figure 4.6 shows an interesting case (June 27, 2008), since it illustrates a period in which winds were strong but the cloudiness decreased dramatically around local noon. Although the behavior between SLS and SA SHFX was similar, the SLS underestimated fluxes largely (20-50%) and consistently. Underestimation was more dramatic during nighttime. This figures illustrates that underestimation increases as wind speed increases. Brief overestimation was present again during stability transition periods, but the values were smaller than in the other cases due to the strong winds. An interesting feature was the good agreement found during a brief period with thick clouds present before noon. The agreement can only be attributed to the decrease in SHFX associated with a sharp

decrease in solar radiation. This supports the statement that underestimation decreases towards neutral conditions.

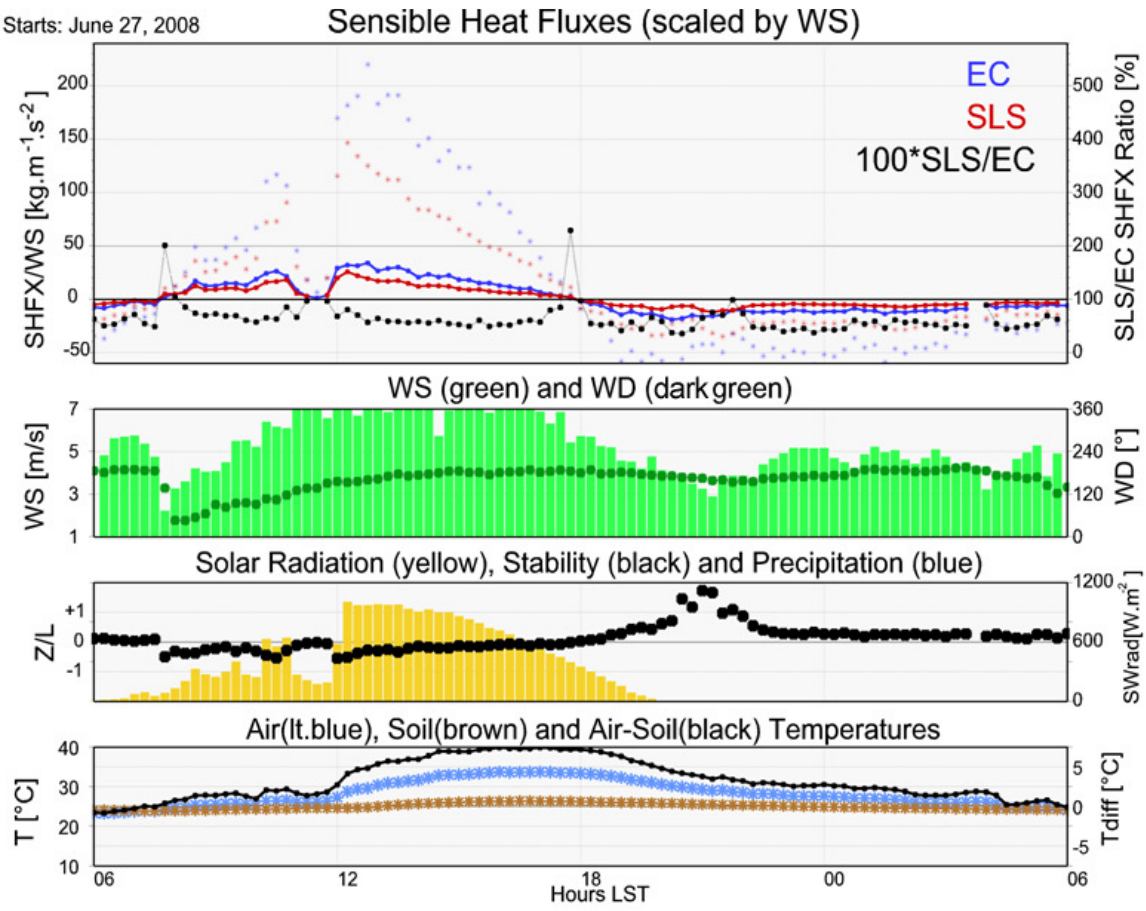

Figure 4.6. June 27, 2008: Strong winds under cloudy and clear skies.

A similar behavior was present during the previous day (June 26, 2008) and is shown in Figure 4.7. The main difference was the weaker winds. Consequently, underestimation was present but reduced in magnitude and overestimation during stability transitions increased significantly. Another interesting feature to point out is the more smooth nature of the behavior of SLS SHFX when compared against EC ones, which has been widely discussed in the literature. This behavior is associated to the fact that SLS fluxes represent path-averaged quantities.

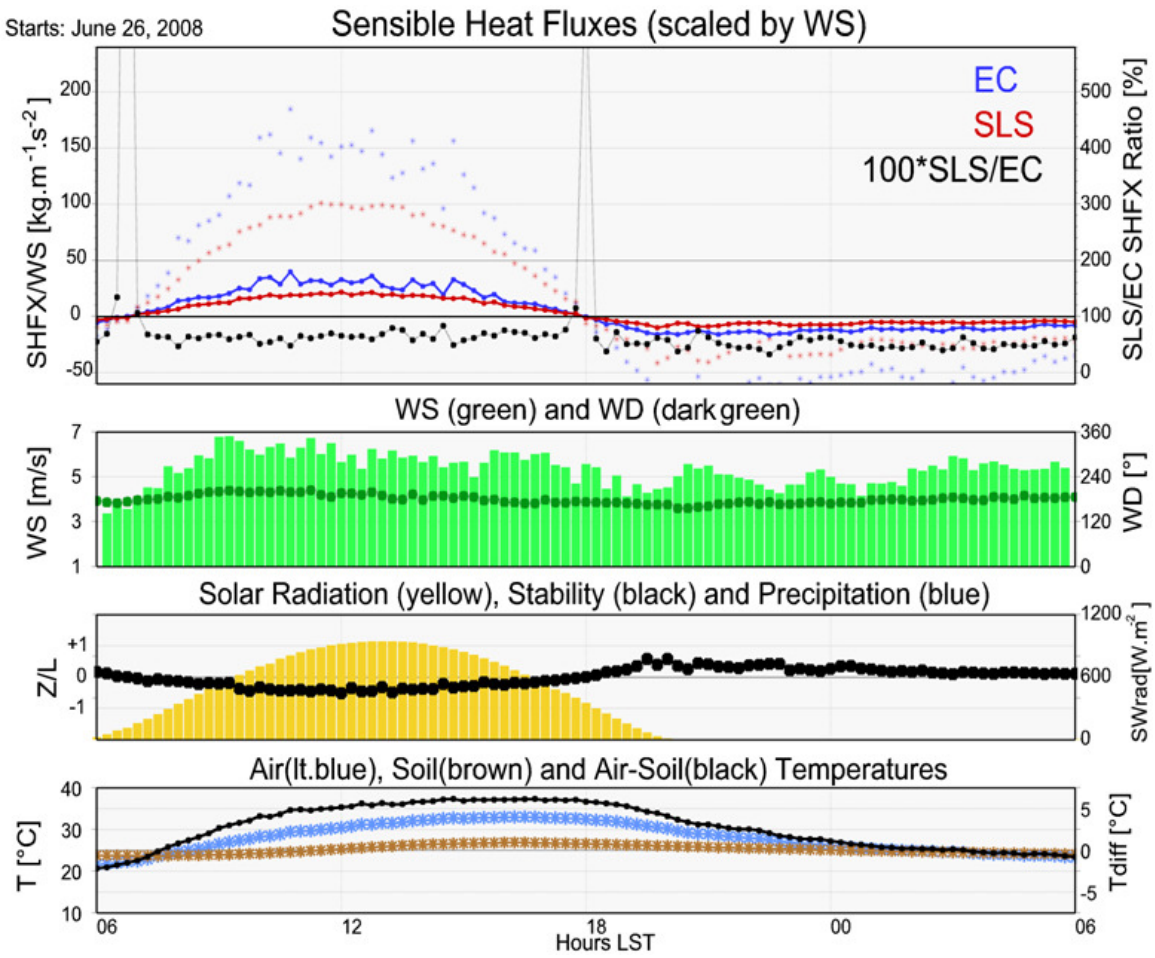

Figure 4.7. June 26, 2008: Strong winds under cloudy and clear skies.

Figure 4.8 illustrates the common response of SLS to rainfall. During rainfall events, scintillations are distorted by water droplets and the SLS cannot measure correct quantities. It is observed, however, that sometimes when heavy rainfall occurs the SLS takes some time to recover. This seems to be caused by water entering the transmitter and receiver windows and taking some time to evaporate. When rainfall is light the SLS only has problems measuring during the event itself.

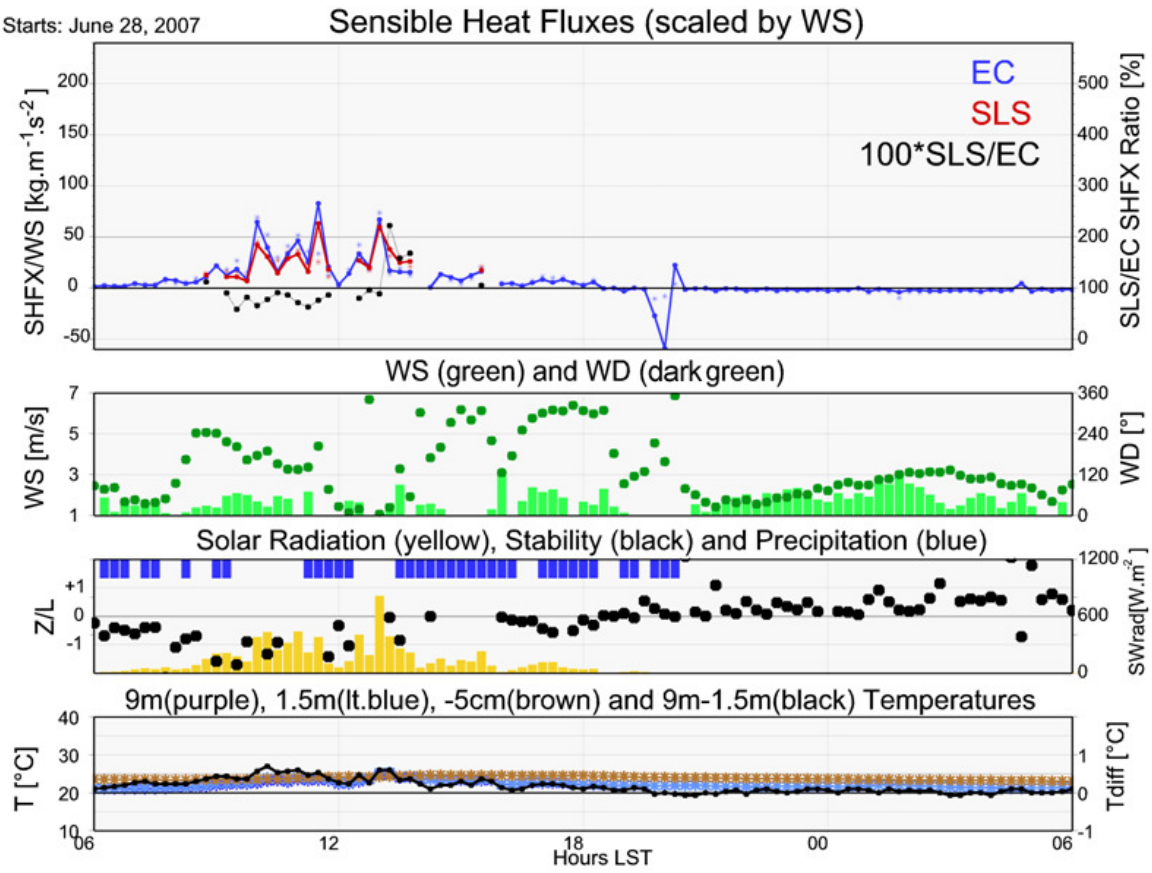

Figure 4.8. June 28, 2007: Effects of rainfall on measurements.

4.3.2. Average diurnal cycles.

Average diurnal cycles of sensible heat fluxes are illustrated in Figure 4.9. Blue is used for EC sensible heat fluxes and red for the SLS. The scatter represents individual observations and the lines the average diurnal cycles. The average SHFX ratio (SLS*100/EC) is plotted with a black line. Time is expressed in local standard time (LST). As expected, the behavior of SHFX is almost perfectly sinusoidal during daytime in response to the diurnal cycle of incoming solar radiation. During nighttime, larger SHFX are found before midnight due to stronger wind speeds that decrease as the night progresses. Transition periods occur around 19 LST during the evening and around 7:30 LST during the early morning or about one hour after sunrise and one hour before sunset.

Given that the measurements were carried during the summer, sunrise and sunset times did not change largely during this period but some effect of day length is definitely present. The largest SHFX occur around 13 LST which coincides with the time of the day with the largest incoming solar radiation, since daylight savings were present.

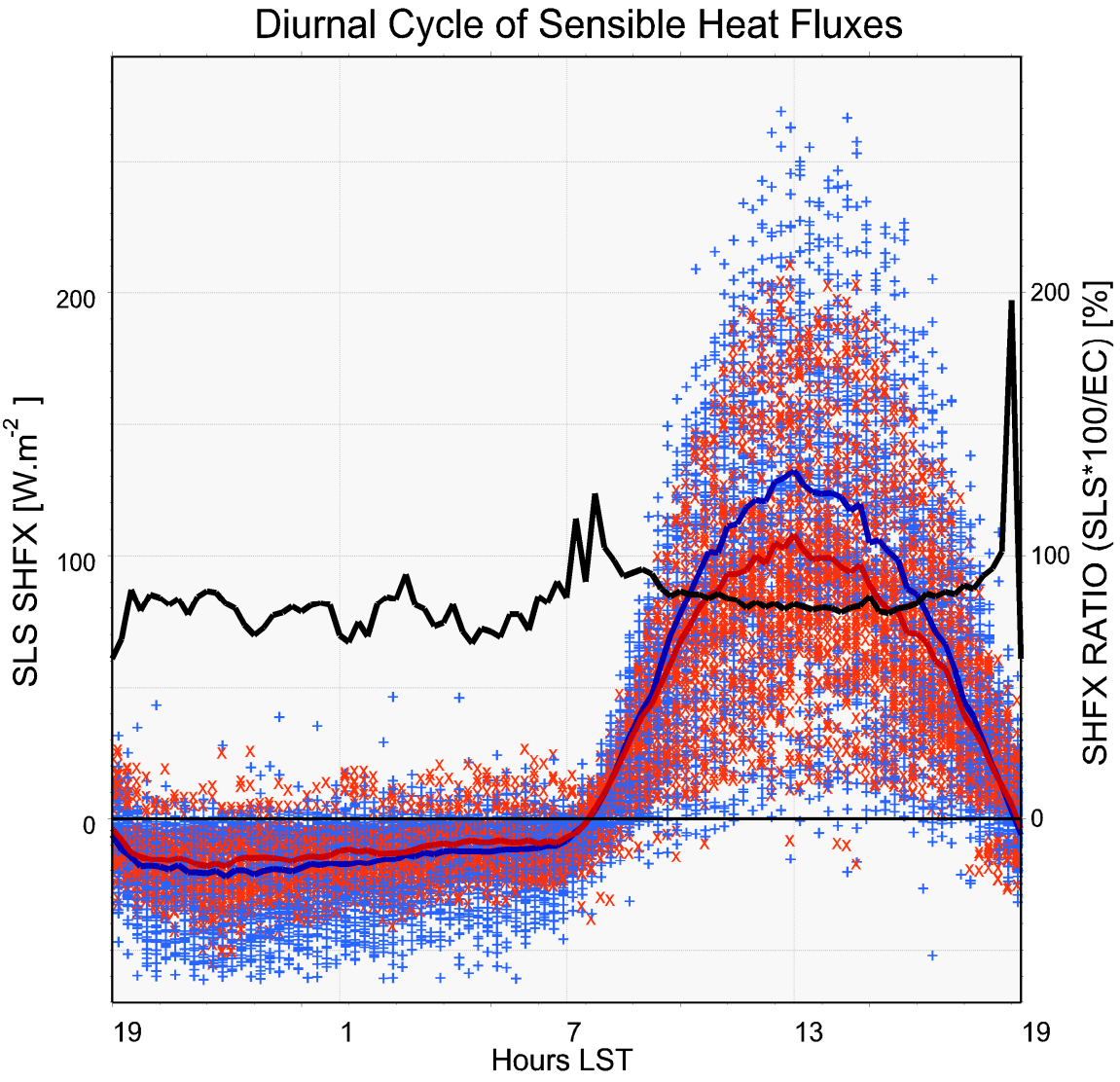

Figure 4.9. Average diurnal cycle of sensible heat fluxes for both 2007 and 2008, measured with the RMYoung SA.

SHFX magnitudes vary between -60 and +5 $W.m^{-2}$ during nighttime, and between -5 and +280 $W.m^{-2}$ during daytime. This figure confirms that the SLS underestimates SHFX most of the time with the exception of stability transition periods (i.e. neutral conditions), when problems due to weak scintillations lead to overestimation. The inability of the SLS to determine the sign of the fluxes takes a toll very close to neutrality: EC SHFX are close to zero it is not certain whether SLS fluxes are positive or negative since they represent path-averaged quantities instead of a point measurement. Nighttime underestimation ranges between 10 and 40%, and is larger than during daytime when it varies between 0 and 25% on the average sense. The behavior of the ratio is also dependent of stability. Nighttime ratios exhibit more variability which responds to a wider scatter in SHFX during this period. Daytime ratios have a sinusoidal behavior which indicates that underestimation is larger when SHFX are larger.

The effects of WS on the diurnal cycle of SHFX ratio are explored in Figure 4.10. It shows that there is a clear WS dependence with increased underestimation under stronger winds. The scatter is much smaller during daytime. During nighttime, wide scatter occurs when winds are weak (wind speed < 4 $m.s^{-1}$). This indicates that periods with weak winds under stable conditions lead generally to SHFX overestimation, but the scatter is quite large. Observations with large underestimation (50-90%) are also present during this period, but they are few. The scatter is also large near transition periods when neutral conditions prevail, and in this case the effects of wind speed are less important.

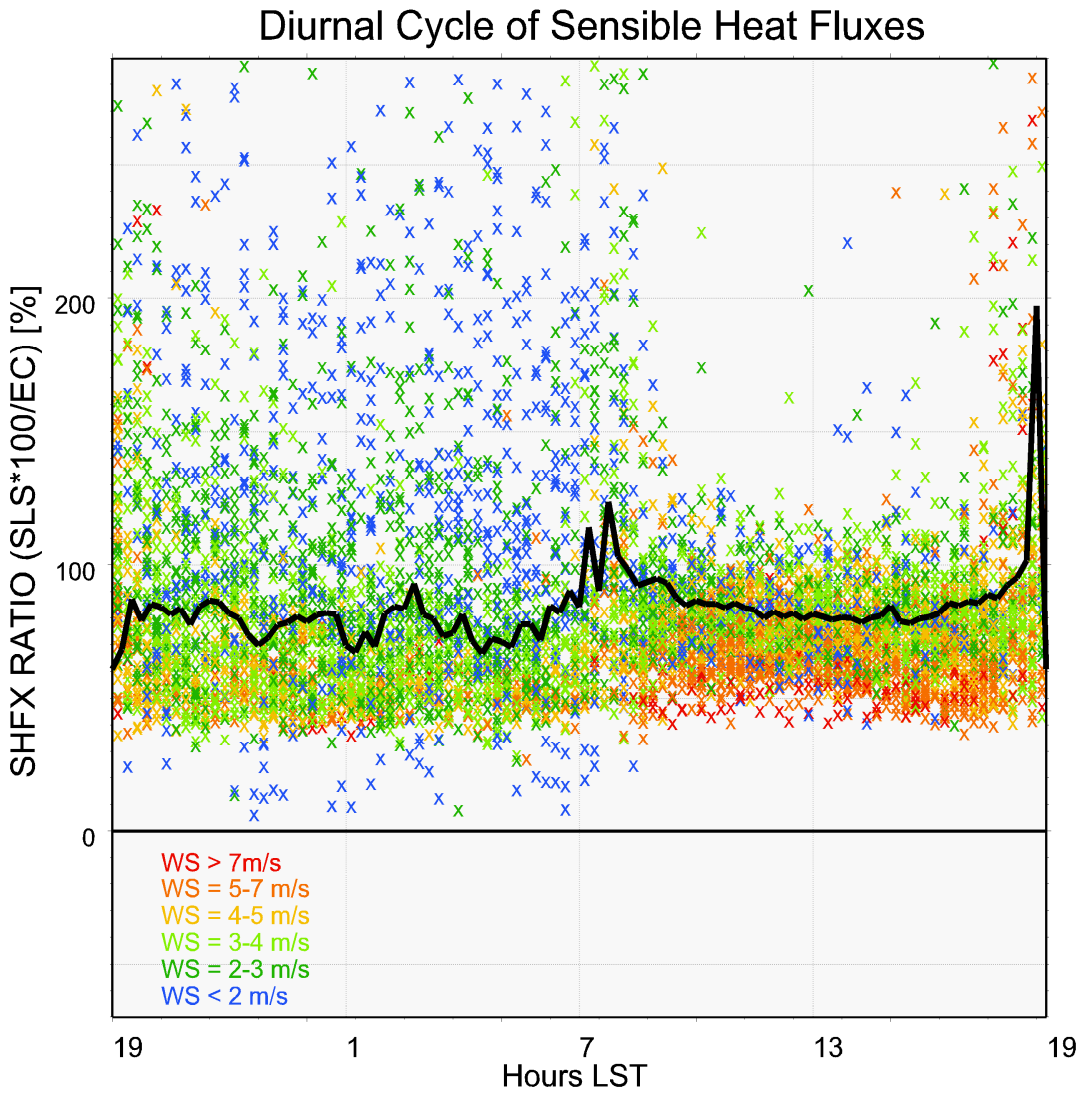

Figure 4.10. Average diurnal cycle of sensible heat flux ratio.

4.3.3. Sensible heat flux scatter plot.

The next step was to explore the SHFX scatter plot, which is presented in Figure 4.11. The fluxes are plotted as a function of WS. Flux ratios and standard deviation of the flux ratios are included with black lines. The data were organized in 10 Wm^{-2} bins and bin statistics were calculated. Figure 4.11 shows that SHFX compare relatively well. The

scatter is smaller under unstable conditions when r^2~0.9. Under stable conditions the scatter is larger with r^2~0.7. The slope of linear fits are also different. It should be noticed, however, that the trend is not perfectly linear, especially under unstable conditions. Underestimation is large under stable conditions and increases with increasing WS (slope ~ 0.48). Under unstable conditions underestimation is less.

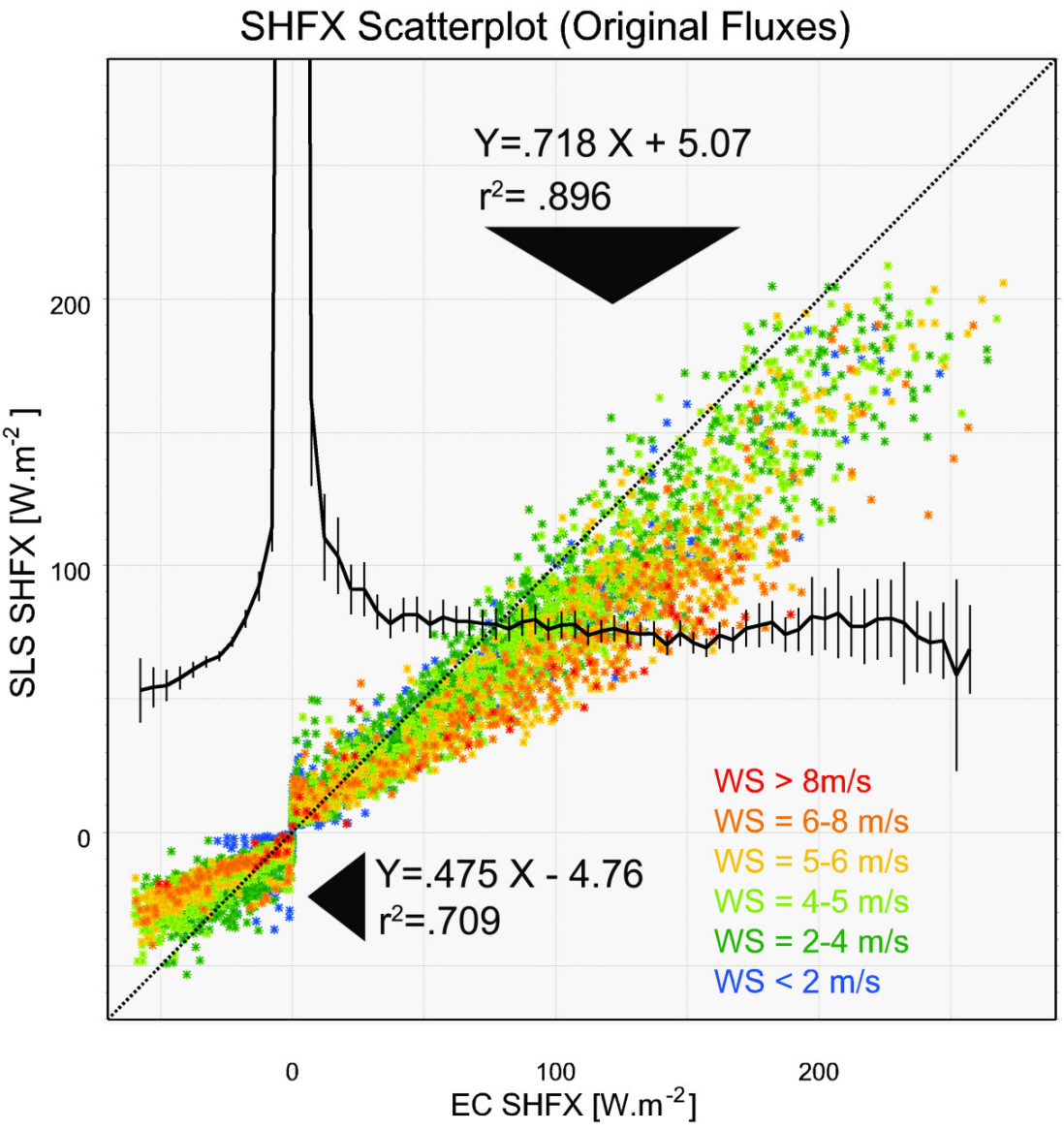

Figure 4.11. SHFX scatter plot and ratio.

Since the relationship between the SLS and the SA SHFX is not perfectly linear, it becomes more appropriate to explore the ratios and their standard deviation. Except near neutral conditions when large overestimation occurs, SHFX underestimation is present everywhere. Under unstable conditions the ratio is almost constant for SHFX larger than 40 W.m^{-2} with some variability. The standard deviation increases for fluxes larger than 200 W.m^{-2}, partly in response to a smaller number of observations. Under stable conditions ratios decrease almost linearly as a function of increasing SHFX magnitude. The standard deviation also increases accordingly.

4.3.4. Effects of wind speed and stability.

The results so far indicate that there is both a dependence on WS and stability, and significant SHFX underestimation which requires further investigation. SHFX ratios were thus plotted as a function of stability (z/L) and WS in Figure 4.12. Friction temperature θ_* and friction velocity u_* ratios were also plotted to partition the effects of WS and stability based on equation 4.2:

$$SHFX = -\rho C_p \theta_* u_* \qquad (4.2)$$

It should be noted that these values are not independent of each other, and the implications will be discussed accordingly. The results are colored for different stabilities just with the aim of improving visualization.

The effects of u_* dominate closer to neutrality since their values are larger than those of θ_* while the opposite occurs away from neutrality. When stratified by stability, these effects balance out for the most part, leading to a general slight underestimation except when high stability is present (i.e. associated with weak winds). On the other

hand, the results confirm again that there is clear dependence on WS with underestimation under strong winds, when u_* is largely underestimated.

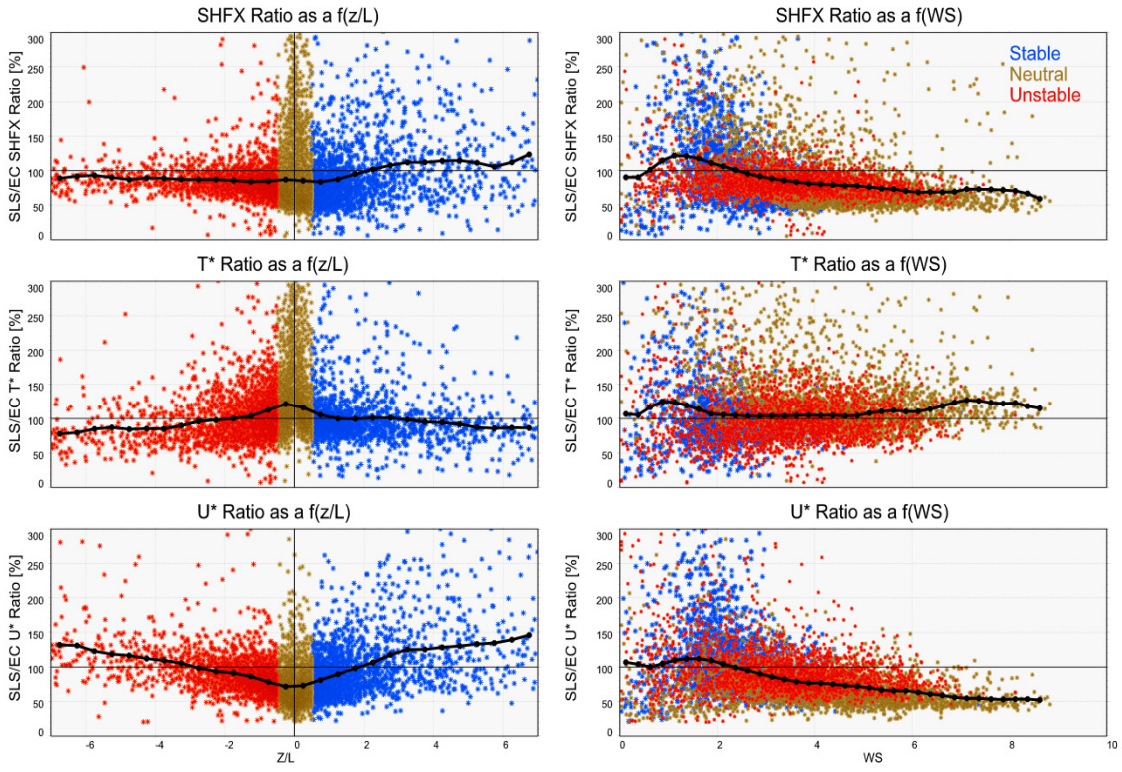

Figure 4.12. SHFX ratio as a function of stability (left) and wind speed (right).

4.3.5. Corrections to scintillometer measurements.

The positive implications of improving MOS empirical approximations to φ_ϵ and φ_{CT2} (section 2.2.3), geared the initial analysis towards the evaluation and adjustment of SLS φ_ϵ with SA φ_ϵ derived from turbulence spectra. It was found, however, that the impact of the new expressions was not the main source of the discrepancies found on the SLS data. The analysis was then oriented to establish inter-comparisons in other sections of the algorithm which is detailed in the following. A summary of the initial analysis that focused on MOS is summarized in Appendix 1.

After further investigation, it was found that largest source of discrepancies arises from the measurement of l_0 and C_n^2. These results coincide with those described by a few SLS researchers (Bram Van Kesteren, personal communication, 2011; Oscar Hartogensis, personal communication, 2011) who also argue that these discrepancies are systematic so there is room for correction. In the case of l_0, problems arise from inaccuracies present in the dissipation range of the Hill Spectrum for Refractive Index Fluctuations (Hill, 1978). These discrepancies are not easy to overcome due to the need of measurements with very high temporal resolution.

It is important to highlight that C_n^2 and l_0 are interconnected via the Hill Spectrum (see section 2.2). Yet small, l_0 has an effect on the calculation of C_n^2. An ideal approach to correct SLS measurements would be to evaluate SLS l_0 and σ_x^2 using SA data. Yet, a more practical and applicable approach for future researchers and SLS users is to correct l_0 and C_n^2 instead.

Errors in l_0 and C_n^2 can be tied to those found in u_* and θ_* via the SLS algorithm (Figure 2.12). Yet when u_* and θ_* are connected, u_* is tightly linked to φ_ϵ, ϵ and l_0; whereas θ_* is closely related to φ_{CT2}, C_T^2 and C_n^2. In the case of l_0, the SLS overestimates it and this overestimation increases under stronger WS. Accordingly, the effects of WS were accounted in the determination of corrections for l_0 by scaling it by WS before fitting polynomials. Normalization was done in terms of WS instead of u_* because WS information is usually easier to obtain than u_* data.

SLS-SA l_0/WS inter-comparison and the polynomial fits are summarized in Figure 4.13. The data is shown for stable (left) and unstable conditions (right). The data used was only that of 2007.

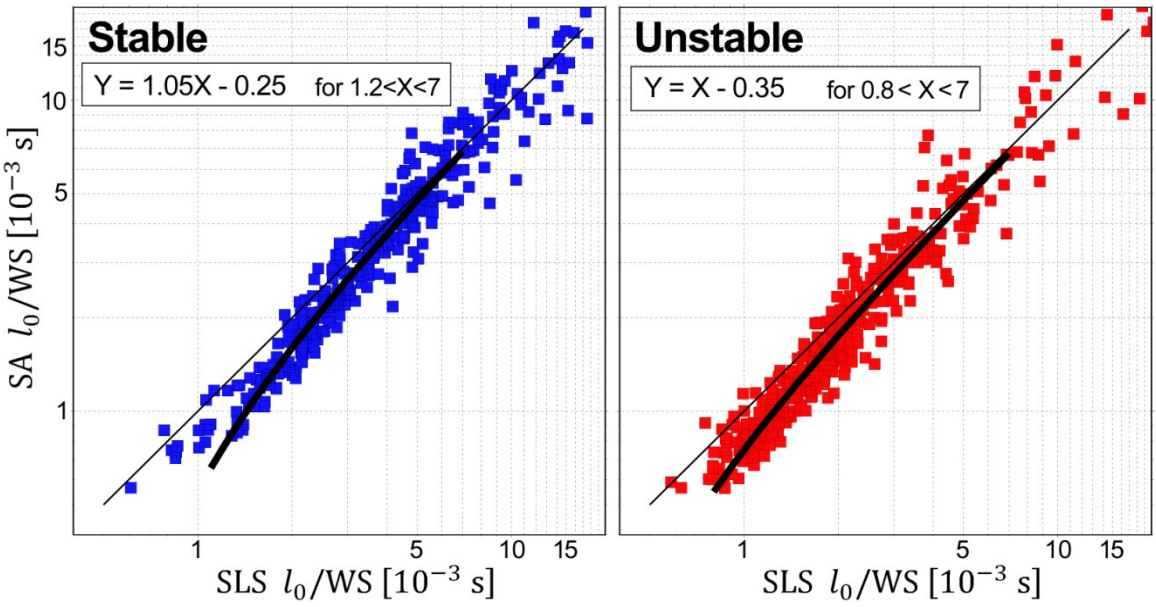

Figure 4.13. l_0/WS scatter plots under stable (left) and unstable (right) conditions.

The proposed corrections to l_0/WS are the polynomial fits indicated with thick black curves. The polynomial expressions that produced the optimal results for are:

$$\frac{l_{0\_new}}{WS} = 1.05\frac{l_0}{WS} - 0.25\ \text{s} \qquad \text{for } \frac{z}{L} > 0\ ;\ \ 1.2\times10^{-3}\ \text{s} < \frac{l_0}{WS} < 7\times10^{-3}\text{s} \qquad (4.3)$$

$$\frac{l_{0\_new}}{WS} = \frac{l_0}{WS} - 0.35\ \text{s} \qquad \text{for } \frac{z}{L} < 0\ ;\ \ 0.8\times10^{-3}\ \text{s} < \frac{l_0}{WS} < 7\times10^{-3}\text{s} \qquad (4.4)$$

where l_0 is in 10^{-3} m and WS is in ms^{-1}.

The corrections were tested in ILREUM data. Their impact was positive for 2007 data, and also for 2008 data, which suggests that the expressions can be generalized. Figure 4.14 compares SA and SLS SHFX and ratio before corrections (left) and after the corrections were applied (right). Data for 2007 is indicated with red (top) and that of 2008 with yellow (bottom). The figure suggests that the application of the corrective expressions was successful for these datasets collected using different SA. Small differences between the 2007 and 2008 data can yet be depicted due to variability that

can be attributed to the SA used. These differences can however be improved by minimal adjustments to the coefficients determined for expressions 4.3 and 4.4, but the proposed expressions are sufficiently general.

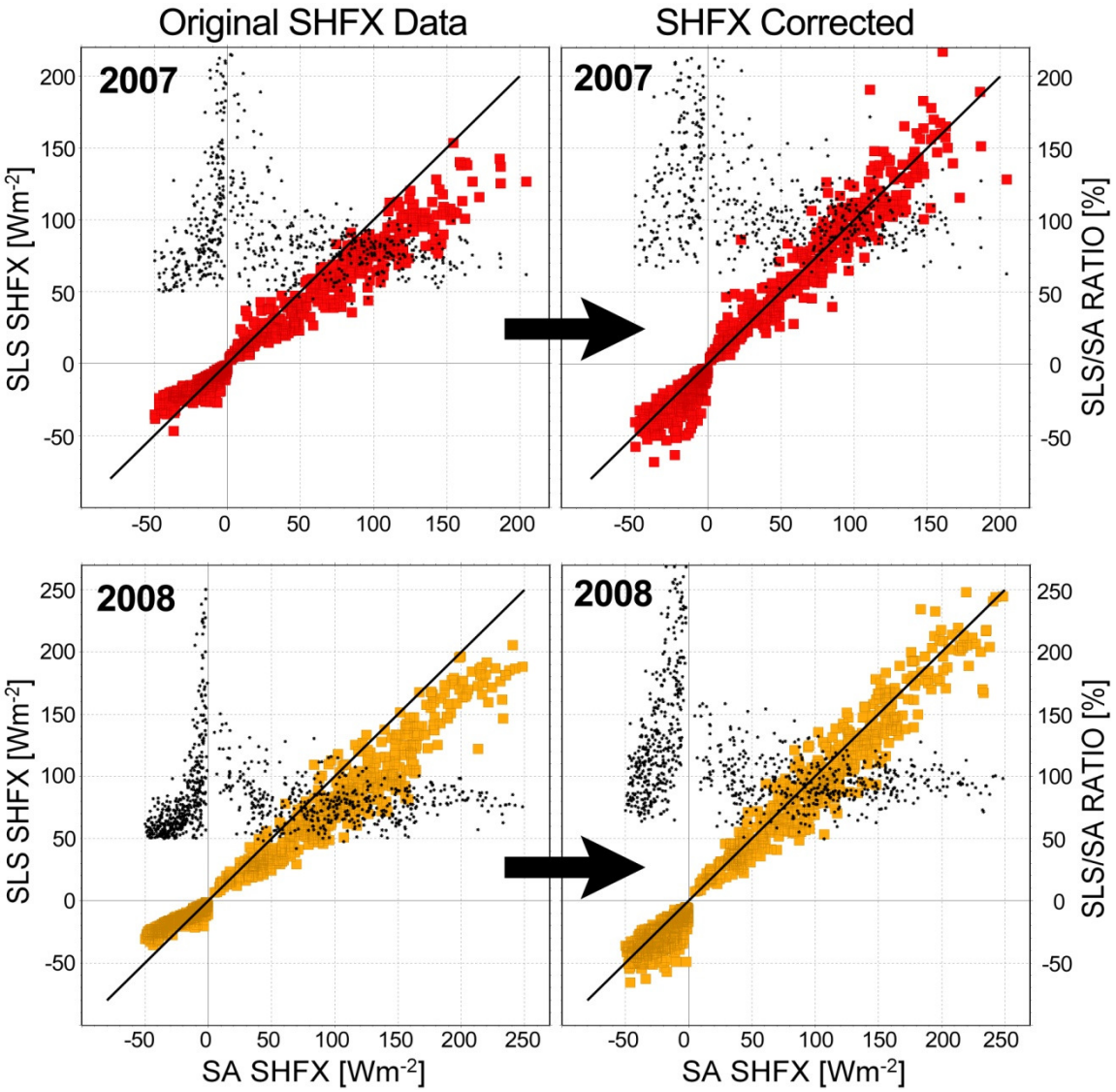

Figure 4.14. Effect of corrections when applied to SLS l_0.

Figure 4.14 shows that better agreement after the corrections were applied. Ratios that ranged from ~50-90% under stable conditions and 70-90% under unstable conditions improved to ~90-100% under unstable conditions. Under stable conditions SHFX

improved for stronger negative fluxes, yet ratios increased too much closer to neutrality on the stable side, which is explored in the following.

The impact of the corrections on the diurnal cycle of SHFX is presented in Figure 4.15. Individual observations are indicated with light blue rectangles for SA and red rectangles for SLS data. Averages are indicated with a dashed line for SA and a solid thick line for the SLS. Ratios are indicated with asterisks.

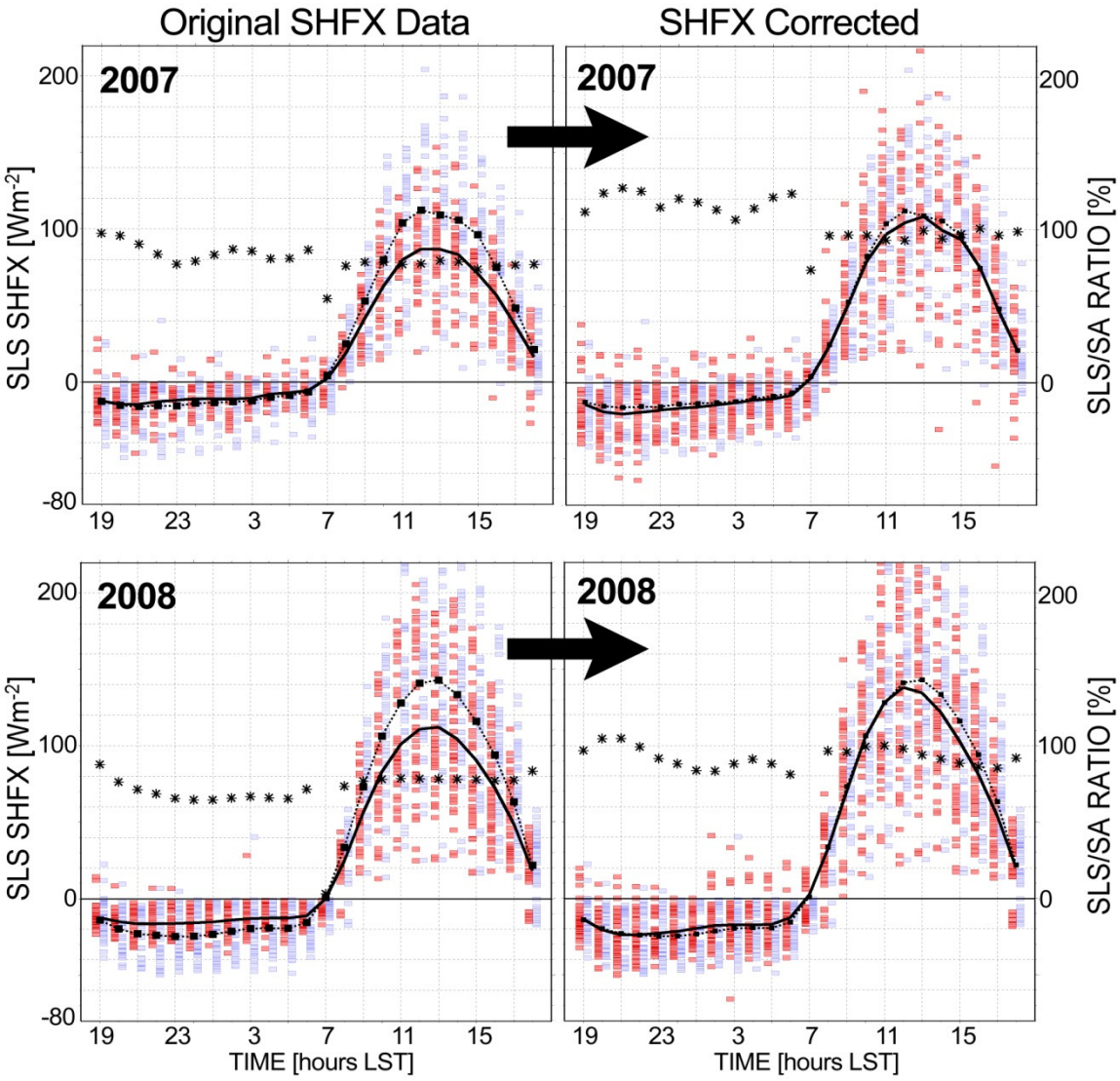

Figure 4.15. Diurnal cycle of SA SHFX (light blue squares and dashed line), SLS SHFX (red squares and thick line) and SHFX ratio (asterisks) before and after l_0 corrections were applied.

To address the overestimation close to neutrality, especially in the stable side, the behavior of SLS C_n^2 in terms of SA C_n^2 was investigated. Limitations arise from a difficulty of the SLS on the measurements of scintillations that are too weak. A scatter plot that inter-compares C_n^2 from SA and the SLS is presented in Figure 4.16. Since the corrections were not linear in this case, it was necessary to establish them based on non-dimensional quantities. Accordingly, the inter-comparison exercise was established in terms of $C_n^2 z^{2/3}$, and is valid for $z = 2$ m.

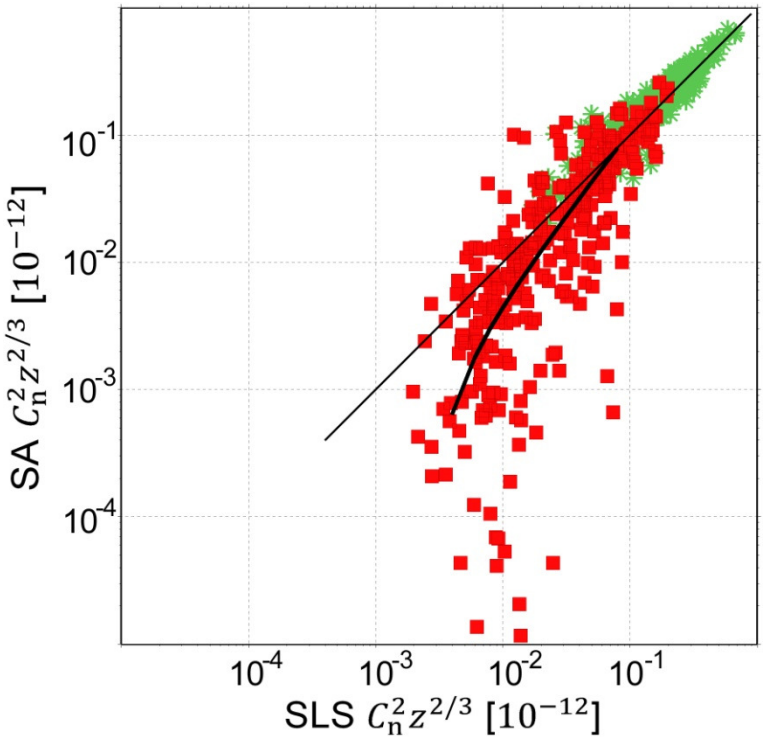

Figure 4.16. C_n^2 scatter plot with polynomial fit.

Red squares represent the data measured under SHFX in the -30 to +30 Wm^{-2} range, and green asterisks for the remaining data. SLS C_n^2 overestimation is evident. The correction expression proposed is:

$$C_{n\_new}^2 z^{2/3} = \left(1.8 C_n^2 z^{2/3}\right)^{1.3} - .001 \qquad \text{for } .004 < C_n^2 z^{2/3} < .09 \qquad (4.5)$$

Where C_n^2 is in 10^{-12} $m^{-2/3}$ and z is in m. The application of equation 4.5 on SLS SHFX produced better agreement with SA SHFX. A scatter plot similar to that of Figure 4.14 is presented in Figure 4.17, but the right panels show the data after both corrections were applied (equations 4.3 through 4.5).

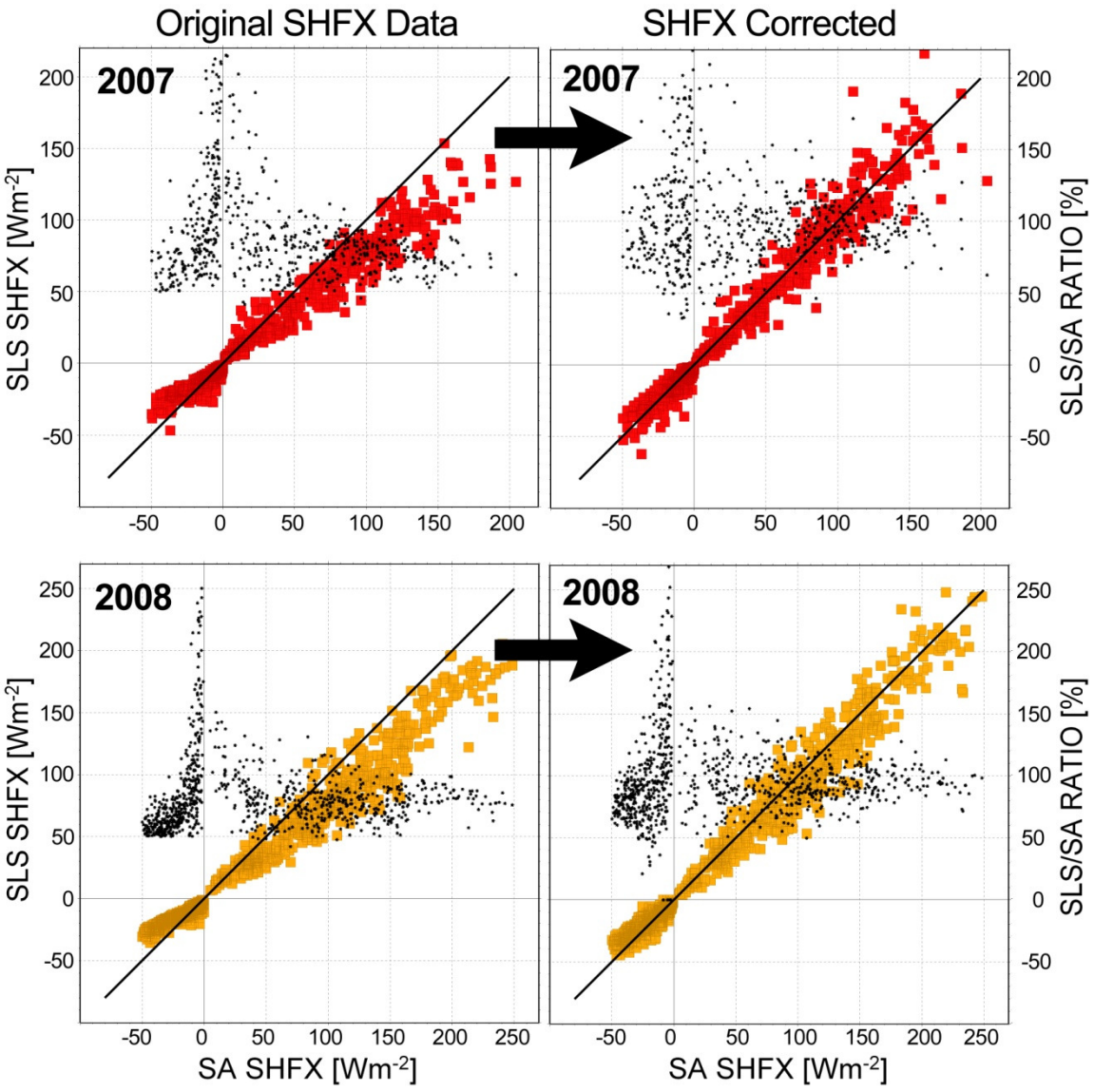

Figure 4.17. Effect of corrections when applied to SLS l_0 and SLS C_n^2.

The effects on the diurnal cycle of SHFX is presented in Figure 4.18.

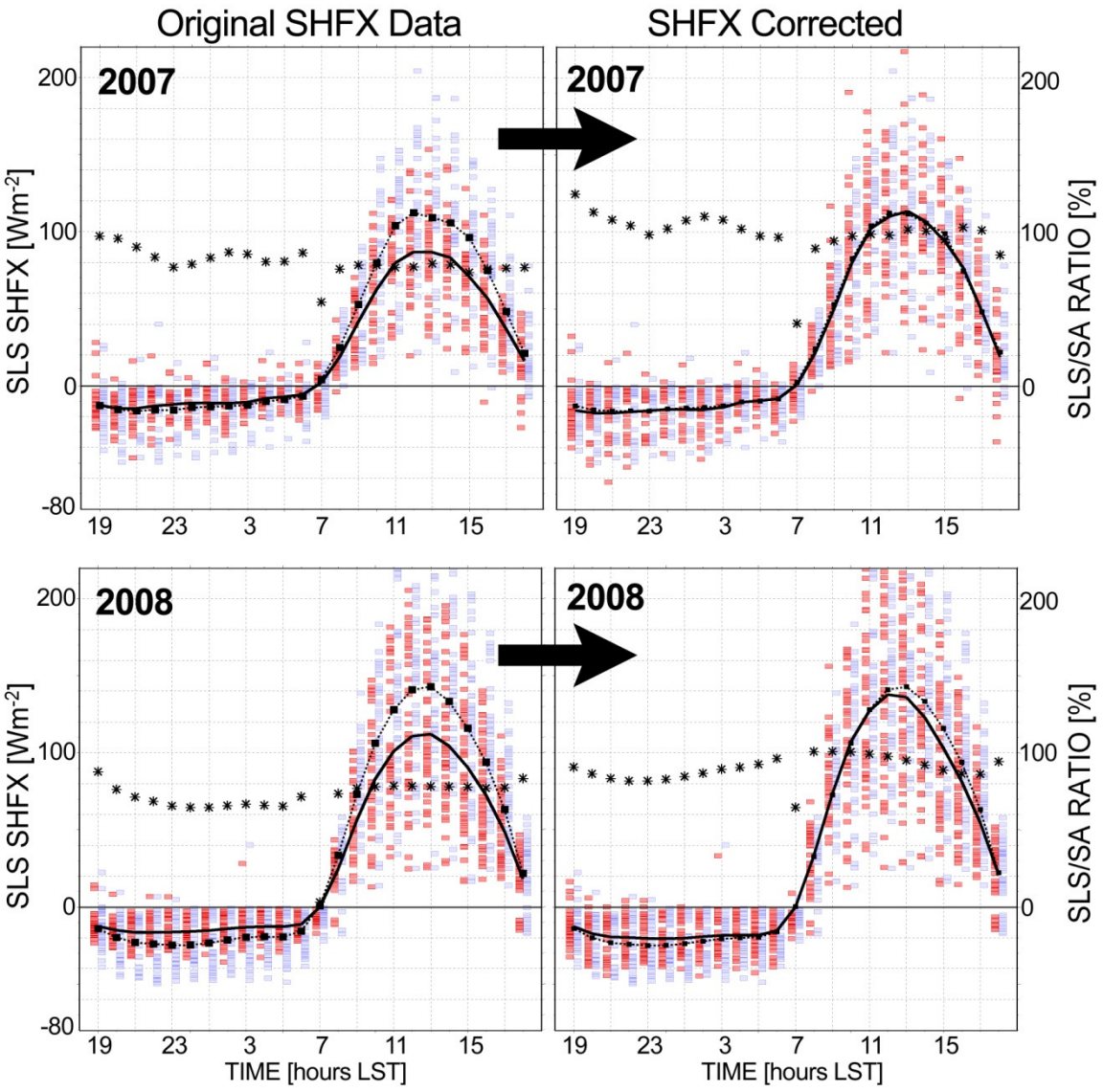

Figure 4.18. Diurnal cycle of SA SHFX (light blue squares and dashed line), SLS SHFX (red squares and thick line) and SHFX ratio (asterisks) before and after l_0 and C_n^2 corrections were applied.

These results are encouraging. Even when expressions 4.3 through 4.5 were determined based on data collected during 2007, they largely improved the agreement with SA data once applied to 2008 data. Lingering discrepancies in the latter suggest that instrument differences may be present. Although instrument-related discrepancies can be

improved by adjusting the corrective expressions following the method described in this chapter, the proposed expressions should be sufficient.

The effect of the corrections on selected diurnal cycles is presented in Figures 4.19 and 4.20. Figure 4.19 shows an inter-comparison of SHFX from SA (light blue squares) and from the SLS (red diamonds) for a selected period during 2007. Original measurements are presented in the lower panel, and corrected SLS measurements in the upper panel. Figure 4.20 is similar but for a selected period during 2008.

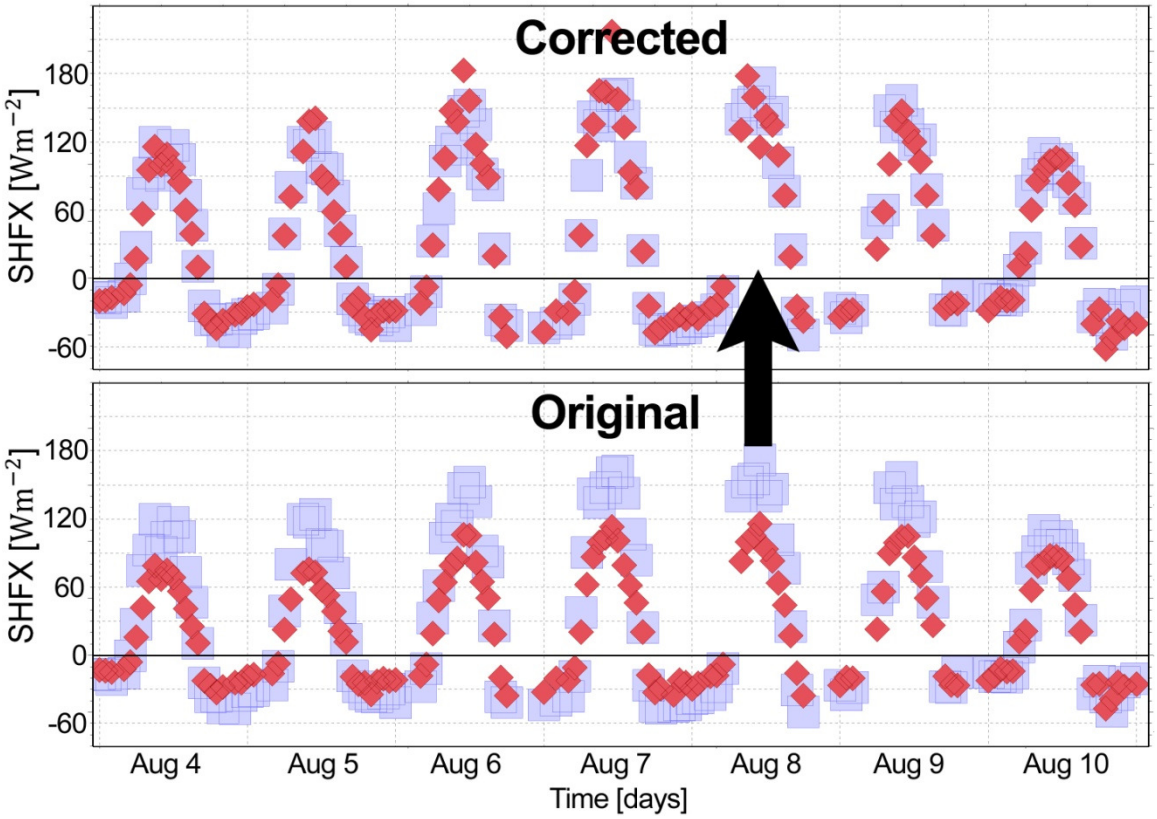

Figure 4.19. Selected diurnal cycles of SHFX before the corrections (bottom) and after the corrections (top). The data corresponds to 2007.

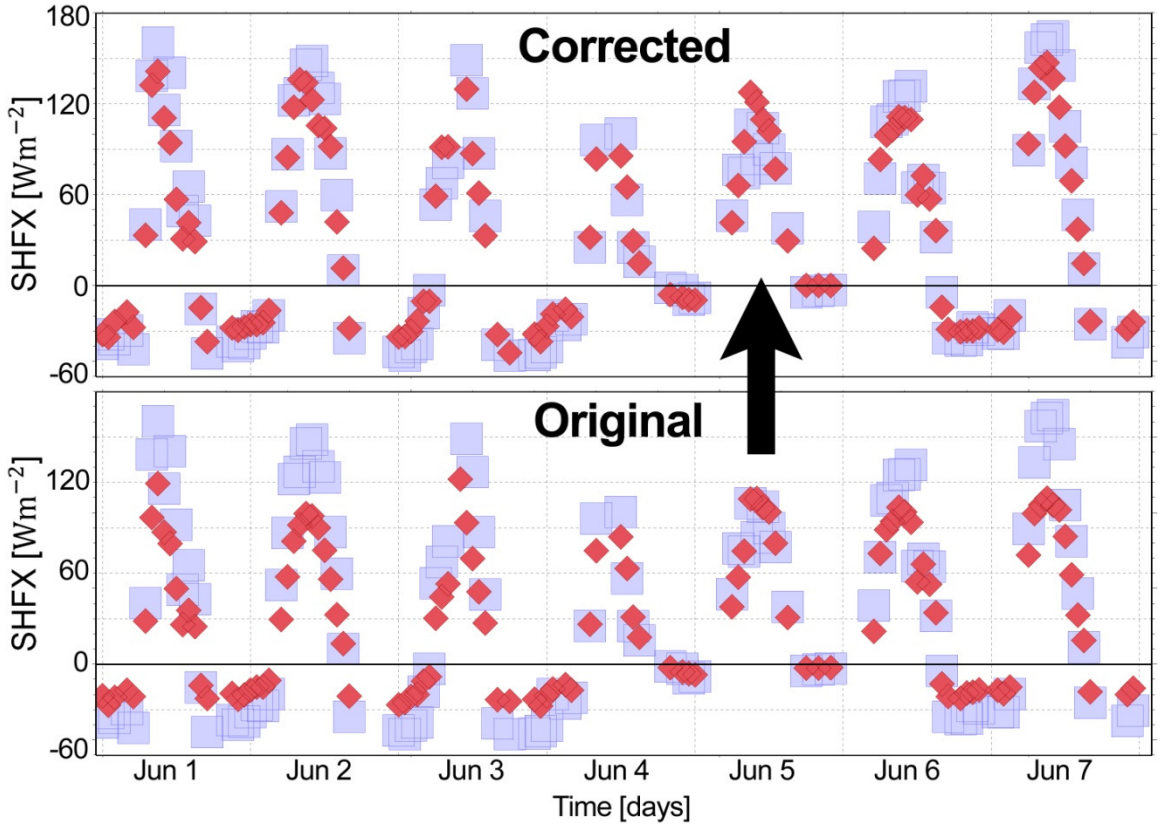

Figure 4.20. Selected diurnal cycles of SHFX before the corrections (bottom) and after the corrections (top). The data corresponds to 2007.

Both figures show that the proposed corrections lead to better agreement between SA and SLS SHFX.

5. ILREUM URBAN CAMPAIGN (IUC) GENERALITIES

5.1. Campaign description.

The ILREUM Urban Campaign (IUC) was conducted in an urban canyon (Núñez and Oke, 1977) located in the campus of the University of Oklahoma in the city of Norman, Oklahoma. The site was located only ~5 kilometers southeast of the sub-urban site and the Norman MESONET site for inter-comparison purposes. Measurements were organized in one ~13 month-long campaign in which the SLS was operated together with 13 SA. A detailed description of the measurement site, the data and the corrections applied follows.

5.1.1. Measurement site.

An urban canyon-like structure was selected based on morphology, location inside an urban environment, closeness to the sub-urban campaigns measurement site and the proper permission from the authorities. The urban canyon selected was located inside the campus of the University of Oklahoma, in the southern tier of the city of Norman, Oklahoma at 35°11'55" N, 97°26'34"W and at 353 mASL. The measurements were made in the Cross Center Building Complex, which consisted of four east-west oriented buildings each measuring $\sim 80\ m$ long. Building height was $h \sim 12\ m$, width $bw \sim 14\ m$ and separation or canyon width $W \sim 45\ m \sim 3.5\ h$. A birds-eye view sketch of the site is presented in Figure 5.1, where buildings (white), ground cover (paved surfaces, grass and trees), instrument masts with SA (black dots) and the SLS (tripods and pink beam) are indicated.

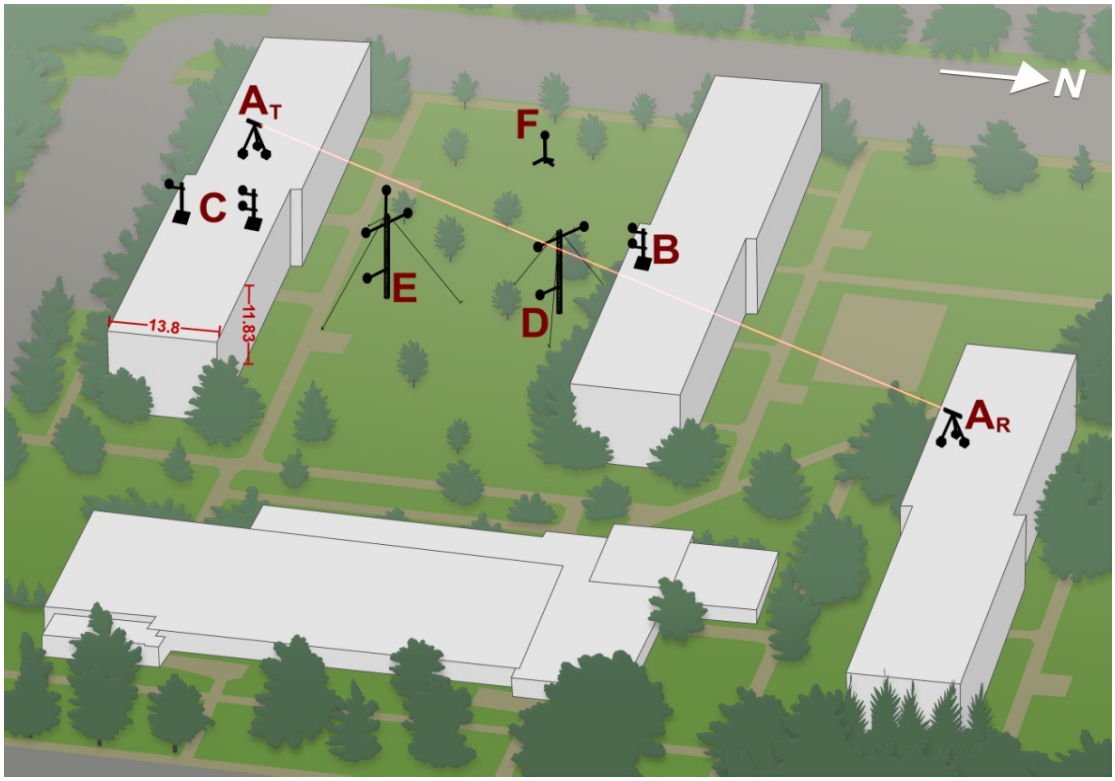

Figure 5.1. Birds-eye view sketch of the measurement site showing instrument placement.

Most instruments were installed across the canopy to measure the cross-canopy distribution of TT. Installed infrastructure included two instrument towers and one ground mast in the canyon, and three roof masts in the surrounding rooftops. The SLS was operated across a similar plane and above the UC. Limitations on path length required measuring SLS fluxes over two urban canyons, however most SA were placed near the widest canyon due to its ideal geometry.

The canyons and buildings were east-west oriented, ideal to maximize the amount of measurements made under cross-canopy flow since Central Oklahoma is characterized by extensive periods with southerly flow close to the ground (Crawford and Hudson, 1973). The only limitation was that the surface was covered with grass and a few small trees, not a typical ground cover for an urban canyon, usually which usually contains a

paved road (Núñez and Oke, 1977). Site selection was also constrained by the appropriate permission from authorities. Permissions were ready by the Spring of 2009 and all instrumentation became operational by July 2009, when the official campaign started.

Describing the fetch that surrounds a measurement site is essential because a large part of the SHFX advected into the domain are generated in this region. Accordingly, a map of the measurement site is presented in Figure 5.2.

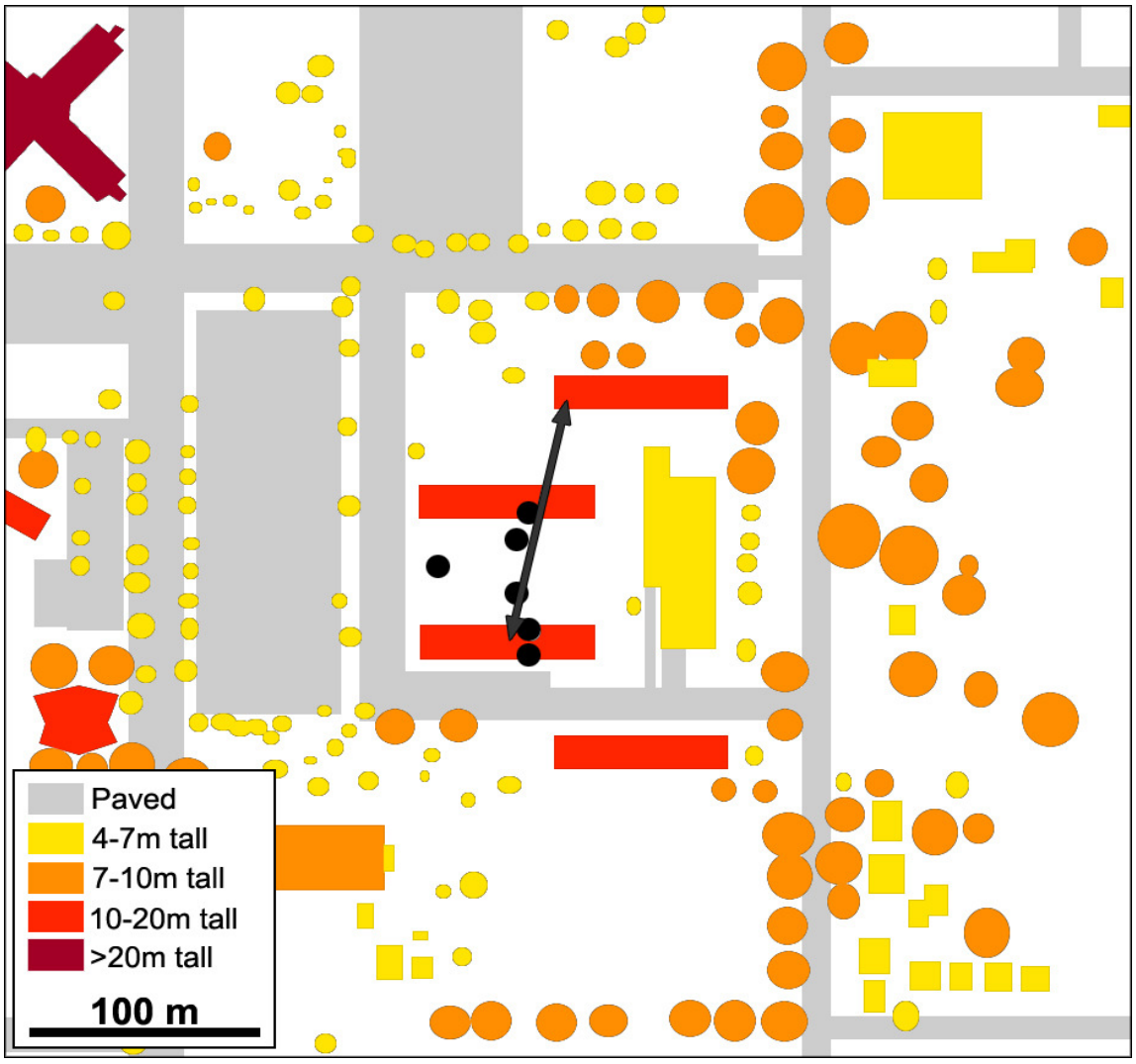

Figure 5.2. Map of the measurement site showing paved surfaces (gray) and the placement and height of objects taller than 4 m (yellows, oranges and reds). Sonic anemometers appear as black dots and the scintillometer as a dark gray arrow.

The map in Figure 5.2 highlights the location of paved surfaces (gray), objects of increasing height (yellow, orange, red, burgundy) and instrument masts (black dots for SA and a dark gray arrow for the SLS). The Cross Center building complex can be depicted as the four red buildings near the center. It is important to highlight the road immediately south of the southernmost building. Flow advected from this region was characterized by higher values of SHFX than when advected from the northern tier. This shows the differences present in the URSL that arise from flow interaction with the different arrangements of surfaces present in the UC. The large tower located to the extreme northwest, one of a set of three, placed the site under its wake during periods with strong northwest winds. This affected the calculation of d_0, an essential parameter to achieve a representative calculation of dimensionless height z'/L.

Photographs of the measurement site are presented in Figure 5.3.

Figure 5.3. Photos of the measurement site and instrumentation.

Panel A shows the SLS transmitter and the array of six SA located near the path. The photograph was taken from the SLS receiver. Panels B and C show different views taken from the central courtyard. The south tower is visible in both pictures. Panel C shows the ground mast, which was powered with solar panels and a battery.

5.1.2. Data collection and data sets.

The data collected included SA velocity and temperature measured at 10 Hz. Turbulence data from the SLS were measured simultaneously but at 1-minute intervals. The data collection process was made automatic. SA data were transmitted wirelessly to a computer whereas SLS data were transmitted via a cable to the same computer. Once available, data were stored automatically in a server. SA masts and the SLS transmitter were powered using solar panels and batteries. Only the towers and the SLS receiver were powered with local energy sources. Short-lived interruptions of the data collection were experienced during heavy rainfall, storms and infrequent power outages.

Data collection started in July 2009 and ended in August 2010. The first instruments set operational were SA placed in roof and the ground mast in early July, followed by the towers and the SLS by early August. Problems with the SLS transmitter occurred after only one day of operation and the instrument had to be sent for repair. This lead to an unplanned duration of only four months with SLS data between late March and July of 2010. SLS data analysis in Chapter 6 thus concentrates in this period.

A summary of instrument placement and data collection periods is presented in Table 5.1, and can be visualized as well in Figure 5.4. SA F (or F1) was the only SA not aligned on the plane where the rest of the measurements were made.

Table 5.1. Instruments operated during the ILREUM Urban Campaign.

Mast	Sensor	Sensor Type	Location	Height above urban surface (m)	Height above earth's surface (m)	Period of operation
AT	AT	SLS transmitter	Roof south courtyard	2	14	Mar2010 - Jul2010
AR	AR	SLS receiver	Roof of northernmost building	2	14	Mar2010 - Jul2010
B	B1	RMYoung SA	Roof north of courtyard	1.5	13.5	Jul2009-Aug2010
B	B2	RMYoung SA	Roof north of courtyard	3	15	Jul2009-Aug2010
C	C1	RMYoung SA	Roof south of courtyard	3	15	Jul2009-Aug2010
C	C2	RMYoung SA	Roof south of courtyard	1.5	13.5	Jul2009-Aug2010
C	C3	RMYoung SA	Roof south of courtyard	3	15	Jul2009-Aug2010
D	D1	RMYoung SA	Northern fourth of courtyard	3	3	Jul2009-Aug2010
D	D2	CSAT3 SA	Northern fourth of courtyard	9	9	Jul2009-Aug2010
D	D3	CSAT3 SA	Northern fourth of courtyard	9	9	Jul2009-Aug2010
E	E1	RMYoung SA	Southern fourth of courtyard	3	3	Jul2009-Aug2010
E	E2	RMYoung SA	Southern fourth of courtyard	15	15	Jul2009-Aug2010
E	E3	CSAT3 SA	Southern fourth of courtyard	9	9	Jul2009-Aug2010
E	E4	CSAT3 SA	Southern fourth of courtyard	9	9	Jul2009-Aug2010
F	F	RMYoung SA	West end of courtyard	2.5	2.5	Jul2009-Aug2010

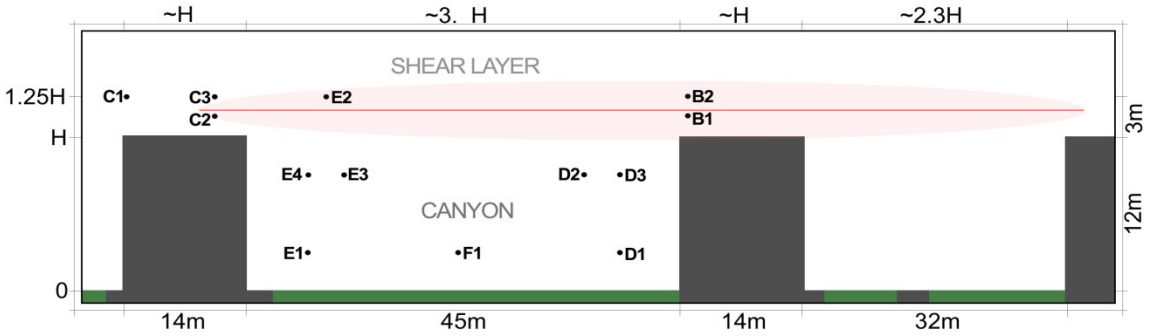

Figure 5.4. Cross-section of the measurement site looking west. Instrumentation is shown according to the

5.2. Corrections applied to the data.

As discussed in section 2.3.2, several assumptions made over the homogeneous and stationary SL fail in the URSL. As a result, several corrections to data from the SLS become necessary. This section describes the corrections applied to the raw SLS data collected during the IUC. The number of corrections was reduced to the essential ones, to minimize the introduction of noise into the datasets. Three sets of corrections were thus explored: corrections to raw SLS measurements determined during the sub-urban campaigns, the determination of appropriate values for d_0 and flux sign determination.

5.2.1. Corrections to raw SLS measurements.

All SLS measurements are subject to errors associated with the instrument itself. Some errors can be improved via the modification of MOS coefficients as suggested by Roth et al. (2006) or by correcting problems in other sections of the algorithm (Oscar Hartogensis and Bram Van Kesteren, personal communication 2011). The corrective expressions determined in Chapter 4 were used here, since they provided very good agreement between SA and SLS data once applied to SLS measurements made under ideal conditions.

Problems with l_0 and wind speed were addressed with expressions 4.14 and 4.15. SLS limitations on the measurement of weak scintillations were then corrected by applying expression 4.16 to C_n^2 measurements. Once both l_0 and C_n^2 were corrected, the algorithm was run to calculate ε and C_T^2. To calculate SL scales in the urban environment, the next procedure in the algorithm, using z' was necessary and a reliable value of d_0 needed to be calculated. This step is the most critical step of the algorithm as will be discussed in the following and in Chapter 6, since SLS fluxes are highly sensitive to z'.

5.2.2. The critical role of zero-plane displacement height.

In rough environments, the mean flow does not necessarily penetrate downward to the very bottom of the RSL. This is particularly true when the flow is perpendicular to the roughness elements. Accordingly, the origin of the vertical axis must be displaced in the vertical by a distance d_0, as explained in section 2.3.2. This allows to apply SL theory assumptions above the new height z'. In the URSL, however, large heterogeneity, lack of stationarity, and the absence of a constant flux layer limits MOS applicability. Yet, using z' is necessary and can lead to SLS fluxes that agree well with SA ones (Roth et al., 2006).

The determination of d_0, however, can be a non-trivial procedure. There are two common approaches: micrometeorological or anemometric and morphometric or geometric (Grimmond and Oke, 1999). Micrometeorological methods use field observations of wind to solve for d_0 using different expressions valid in the SL. An example is the method used by Rotach (1994), where d_0 was determined based on temperature variances scaled by friction temperatures σ_T^2/T_*. The following expression, verified by Tillman (1972) was used:

$$\frac{\sigma_T^2}{T_*} = -C_1\left(C_2 - \frac{z-d_0}{L}\right)^{-1/3} \tag{5.1}$$

where C_1 ~ 0.95 (Wyngaard et al., 1971) and C_2 is larger than 2.5 but can be as large as 3.5 (Tillman, 1972, Beljaars et al., 1983 and De Bruin et al.,1988). d_0 is calculated by minimizing the root-mean-square difference between observations and predictions made using equation 5.3. Although this method was based on ISL similarity theory, Rotach (1994) showed that the results agreed well with those from a morphological approach based on empirical relationships when applied inside the URSL.

Large heterogeneity in urban areas yet poses limitations in the estimation of d_0 using micrometeorological approaches. The problem arises from the failure of SL theory assumptions in the URSL and from the dependence of d_0 on the characteristics of the roughness elements (Roth et al. 2006). A logarithmic wind profile cannot always be attained. Morphometric methods are thus preferred because they are based upon the characteristics of the roughness elements.

The simplest morphometric approaches associate d_0 with a simple representation of the level of roughness. Monin and Yaglom (1971) and Garratt (1992), for example, indicated that for very rough surfaces d_0 ~ 2/3 h_r under neutral conditions, where h_r is the average height of the roughness elements.

An example of a more complex morphological approach is that of Bottema (1995). The approach uses planar areas of buildings and trees and average object height to calculate d_0 via

$$\frac{d_0}{h_r} = \left(\frac{\sum A_{rb} + \sum (1-p) A_{rt}}{A_T}\right)^{0.6} \tag{5.2}$$

where A_{rb} is the area of the buildings, A_{rt} is the area of the trees, A_T is the total area and p is the porosity of the trees. The average height of the roughness elements h_r is also considered. The porosity coefficient varies from 0.6 in winter to 0.2 in the summer. A more complete description and examples of methods used to determine d_0 can be found in Grimmond and Oke (1999).

Equation 5.2 was used to determine d_0 for the urban measurement site. This method produces values that are dependent on wind direction, since the fetch varies upon direction. Object height and area were determined using the map in Figure 5.5, which

was broken into twelve angular sectors each of 30 degrees. A fixed value of tree porosity of 0.3 was used. This value corresponds to springtime. SLS measurements started in April 1, when most of the leaves of the local trees are already out. Finally, a centered mean was applied to the data for smoothing.

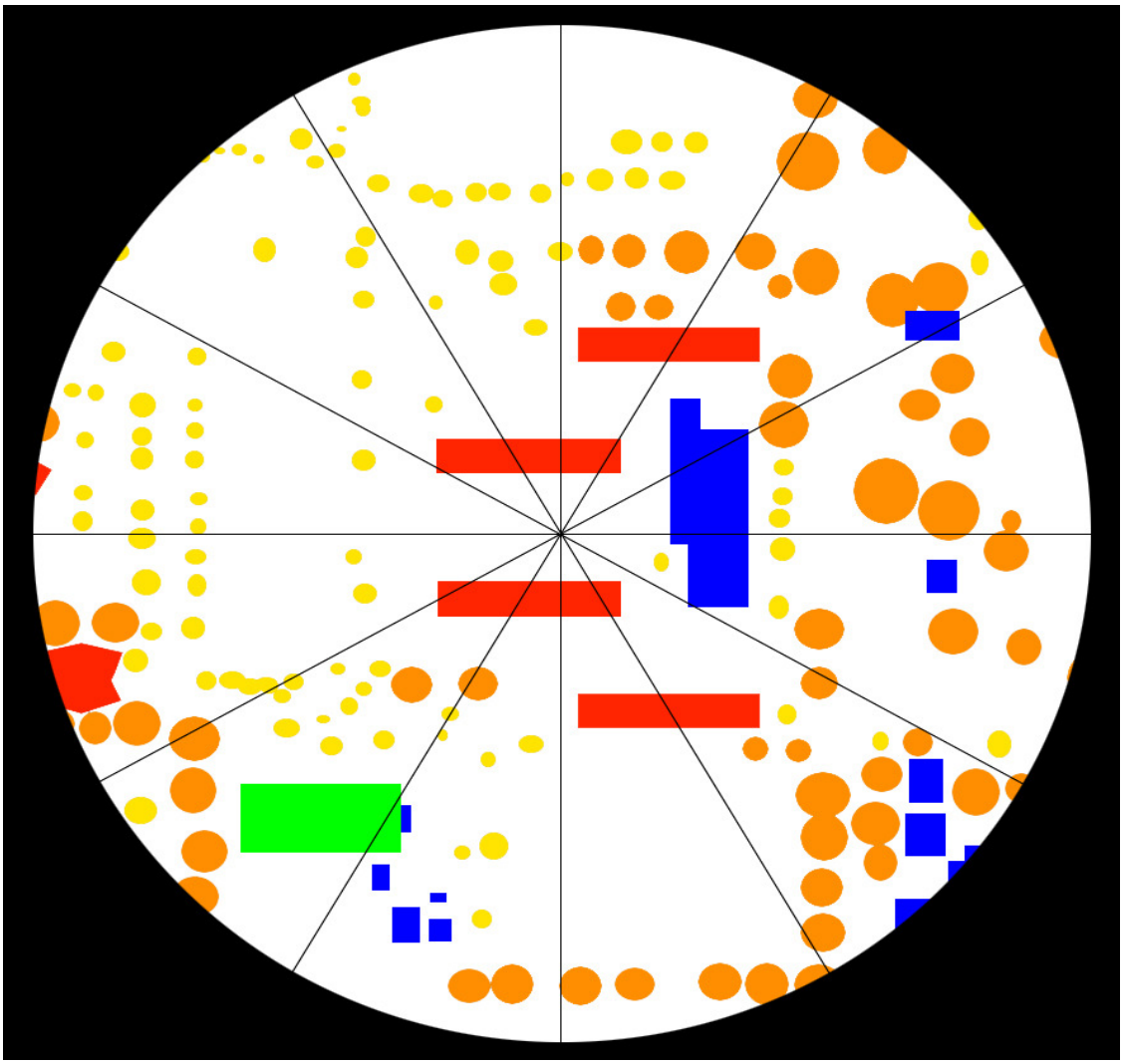

Figure 5.5. Map of the measurement site that was divided in 12 sectors to calculate zero-plane displacement height from building and tree planar areas and heights.

The values of d_0 obtained for the IUC are presented in Figure 5.6. d_0 distribution illustrates the east-west orientation of the canyon, with lower values when the flow is

parallel to the canyon. Values range from ~6.5 to ~8.5 m. Minor asymmetries present can be explained by the effect of trees and buildings scattered in areas that surround the Cross Center Building Complex. These results did capture the change of d_0 based on canyon morphology and also the simple rough approximation of $d_0 \sim 2/3\ h_r$. Furthermore, feasible values of SHFX were obtained once the calculated values of d_0 were considered in the SLS algorithm for the calculation of SHFX from scintillations. Some limitations were, however, identified for some wind directions which indicate that the values of d_0 were too small, and a larger domain was needed. For some wind directions, however, no value of d_0 (i.e. from 0 to h) produced satisfactory results, which indicates that SLS measurements were inapplicable for certain wind directions. This will be discussed with more detail in Chapter 6.

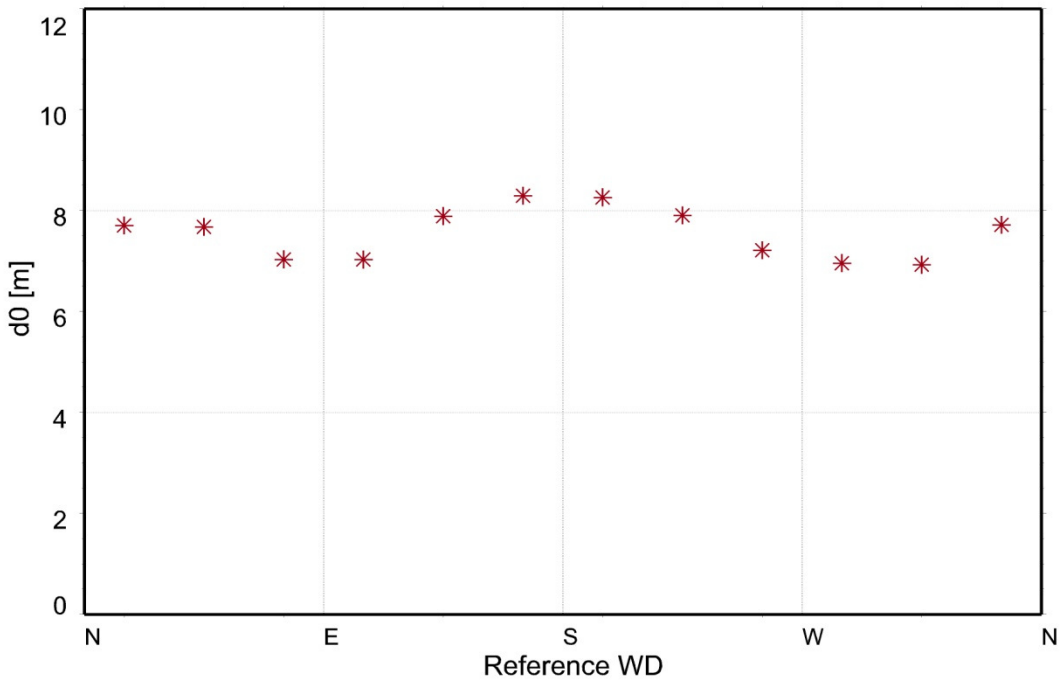

Figure 5.6. d_0 as a function of WD.

5.2.3. Flux sign determination.

As discussed in section 2.2, one of the limitations of scintillometry is the inability of scintillometers to determine the direction of the fluxes. This is why an SLS needs to be operated together with an instrument platform that can provide a measurement of stability. The common procedure has been to place a SA near the center of the path (e.g. Roth et al, 2006). This approach is generally more than sufficient in homogeneous environments, where flow and turbulence vary very little within the SLS path. In the urban environment, however, the situation is different. Large horizontal heterogeneity present in the URSL can lead to regions of opposite stratification along the SLS path, especially near neutral conditions. For example, during some stable nights the heat release from buildings can lead to slightly positive nocturnal SHFX when those over the canyon are negative.

A set of questions thus arises: What is the optimal way to calculate the SHS SHFX sign? If a weighted average of the sonic anemometers operated along the path is the answer, what are the weights that should be considered for each SA? These weights probably depend on stability and wind direction: what is the dependence? What is the solution when not all of the SA along the path operate simultaneously? Some of these questions will be addressed with the results presented in Chapter 6.

6. ANALYSIS OF IUC MEASUREMENTS

Chapter 6 discusses the results found during the IUC. Section 6.1 addresses general flow characteristics. Section 6.2 addresses cases measured during periods with southerly flow. Emphasis was placed on southerly reference WD to investigate TT under cross-canopy flows, since southerly winds the most common WD in Central Oklahoma (Crawford and Hudson, 1973) and more observations were available. Section 6.3 moves into the analysis of TT under different WD. Section 6.4 investigates physical properties behind SHFX distribution.

SA data are presented using the different symbols and colors introduced in Figure 6.1. The analysis is focused on SA data from three levels. Above-canyon data measured at 15-m or $\frac{5}{4}h$ is displayed using orange, green and red asterisks. Upper-canyon data measured at 9-m or $\frac{3}{4}h$ is presented using blue and brown squares for the south and north walls. Lower-canyon data measured at 3-m or $\frac{1}{4}h$ is presented with small blue and brown asterisks, also for the south and north walls.

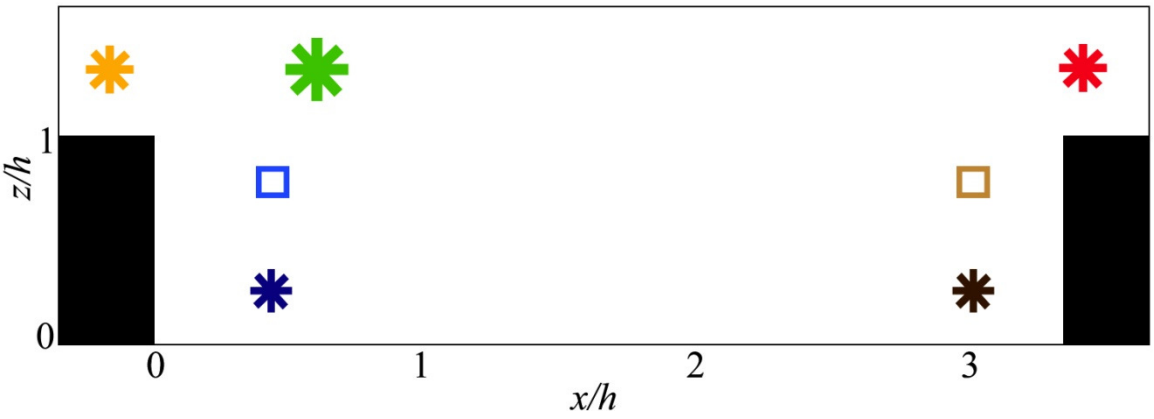

Figure 6.1. Plotting symbols used to represent SA data.

6.1. Characteristic flow.

The characteristics of UC flows are mostly determined by the interactions between the mean flow and the different roughness elements. In the case of an urban canyon, flow modification by the buildings is highly dependent on WD and WS of the reference flow (hereafter, WD_{REF} and WS_{REF}). Flows that are parallel to urban canyons produce in-canyon symmetrical gradients with respect to the canyon facets. Complexity increases under other WD_{REF}. Perpendicular WD_{REF} are of particular interest and will be the analysis foci.

Flows perpendicular to urban canyons produce a rotor or region of recirculation in the upstream section. Recirculation morphology is a function of canyon width W (section 2.4.3) and WS_{REF} (detailed later in this section). From the types of flows described by Oke (1987), the wake interference flow regime prevailed given the urban site morphology. This regime is characterized by a recirculation region that extends from wall to wall, but allows a small region of ventilation in the upper downstream end of the canyon. The latter does reach the ground. A schematic example of this canyon flow regime is presented in Figure 6.2 after Harman et al. (2004) and Oke (1987).

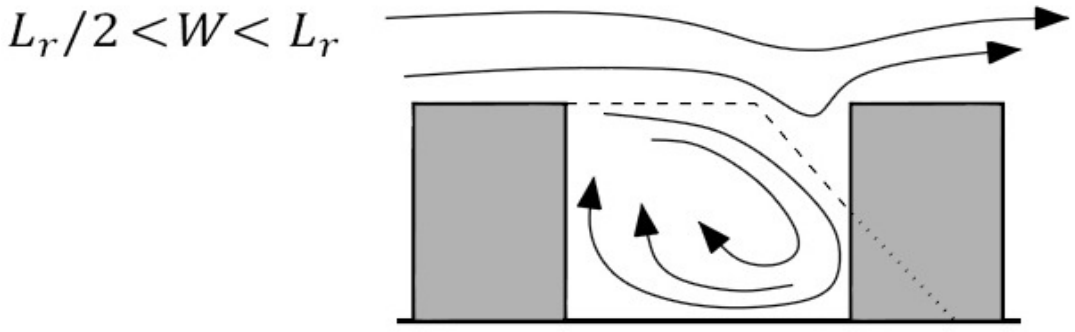

Figure 6.2. Schematic representation of the wake interference flow regime.

IUC observations averaged over periods of northerly and southerly flow are presented in Figure 6.3 and show the prevalence of the wake interference flow regime.

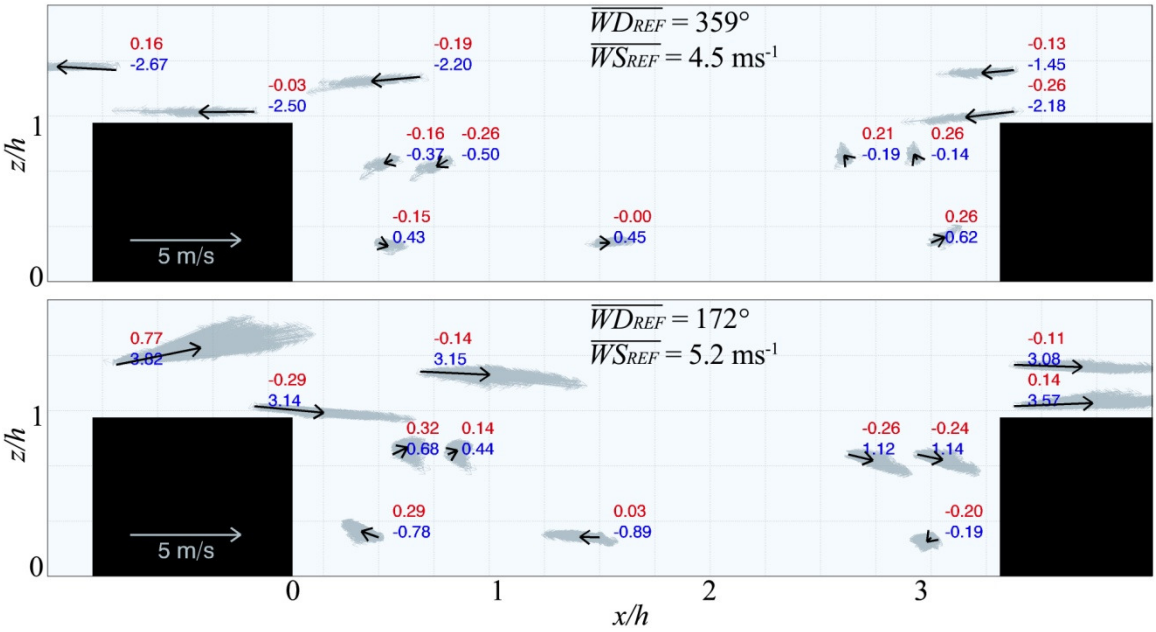

Figure 6.3. Winds measured at the IUC site during selected periods with $\overline{WD_{REF}}$ from the north (top) and from the south (bottom).

Figure 6.3 is a cross section of the measurement site looking west, and shows individual (gray) and average (black) wind vectors for a selection of cases with $\overline{WD_{REF}}$ (i.e. 10-m MESONET winds) that are perpendicular to the canyon. Numbers are mean vertical velocities $\bar{w}$ (red) and mean meridional velocities $\bar{v}$ (blue) expressed in ms^{-1}. Flow enters the canyon along the top and leads to general downward motion along the downstream section and upward motion constrained to the upstream end. In-canyon velocities are more than three times smaller than those measured above the canyon. The downstream section is the exception, where enhanced mixing produces larger velocities. Vectors on the upper upstream end suggest that the recirculation morphology varies. To explore these and other characteristics of in-canyon flows, SA velocities are compared against reference data in the following.

In-canyon flows are analyzed using data from the south tower, selected due to the availability of measurements at three different levels. The tower is located upstream under $\overline{WD_{REF}}$ from the south, and downstream under $\overline{WD_{REF}}$ from the north. Figure 6.4 explores how mean vertical velocities $\overline{w}$ behave as a function of $\overline{WS_{REF}}$.

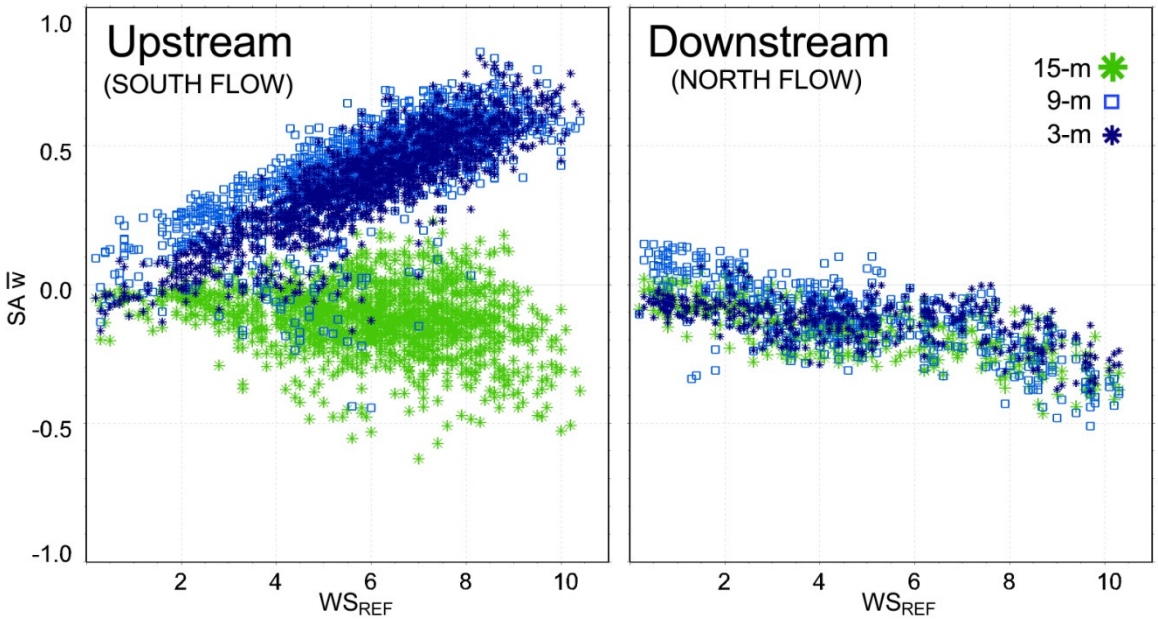

Figure 6.4. SA $\overline{w}$ as a function of $\overline{WS_{REF}}$. 15-m, 9-m and 3-m are presented with green asterisks, light blue squares and small blue asterisks, respectively.

The data show that $\overline{w}$ in and over the canyon are functions of $\overline{WS_{REF}}$. The relationship is not perfectly linear and deviations from linearity are associated with interactions between the flow and the buildings. Scatter is also present due to the complex interactions with the urban area, and the distance to the Norman MESONET or reference site, located 4.5 km to the northeast.

The differences between upstream and downstream ends of the canyon are remarkable. Above- and in-canyon $\overline{w}$ behave very differently in the upstream end. Flow above the canyon sinks into it for all WS, with a few measurements that show upward

motions, in particular when $\overline{WS_{REF}} > 5$ ms^{-1}. Upward motion prevails inside the canyon, especially in the upper end. The differences between the flow at 3 and 9 m suggest that the shape of the region of recirculation changes with $\overline{WS_{REF}}$. Under weak $\overline{WS_{REF}}$ rising motion is larger at 9 m and sinking motion occasionally takes place in the lower canyon. This suggests that the center of recirculation is located higher and descends into the canyon as $\overline{WS_{REF}}$ increases.

In the downstream end, flow primarily sinks and shows very similar behavior at all levels due to turbulent mixing of momentum as the flow progresses along the canyon top. Sinking motion remains smaller than 0.3 ms^{-1} until $\overline{WS_{REF}}$ >8 ms^{-1}, when downward velocities increase linearly to 0.4 ms^{-1} when $\overline{WS_{REF}}$~10 ms^{-1}. A small region of rising motion develops in the upper canyon when $\overline{WS_{REF}}$<2 ms^{-1}. This confirms that the rotor is smaller under weak WS and that the depth of the region of ventilation decreases when $\overline{WS_{REF}}$>5ms^{-1}. A scheme that illustrates the change in the size of the recirculating region is presented in Figure 6.5.

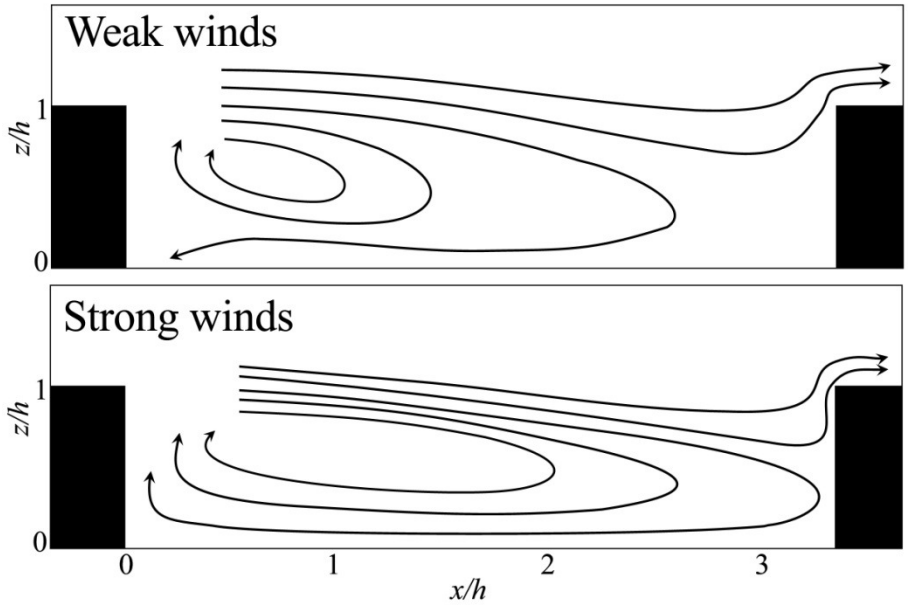

Figure 6.5. Scheme that suggests changes on the recirculation region with $\overline{WS_{REF}}$.

The behavior of WS as a function of $\overline{WS_{REF}}$ is presented in Figure 6.6.

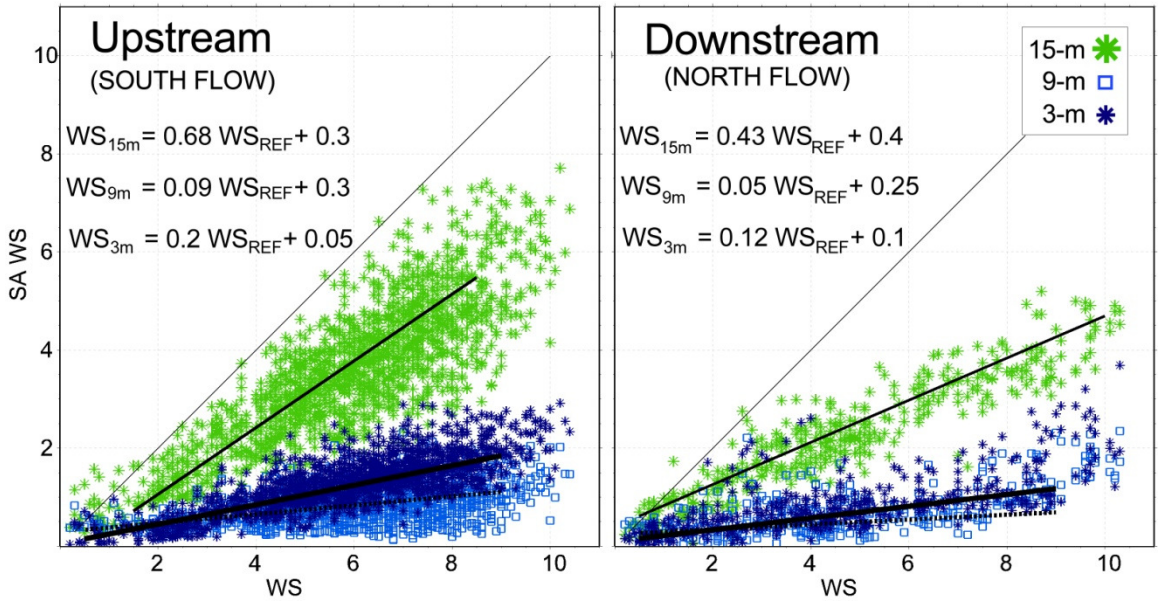

Figure 6.6. SA $\overline{WS}$ as a function of $\overline{WS_{REF}}$. 15-m, 9-m and 3-m are presented with green asterisks, light blue squares and small blue asterisks, respectively.

Figure 6.6 suggests that the relationship between canopy WS and $\overline{WS_{REF}}$ is close to linear, especially within the 2 ms^{-1} $< \overline{WS_{REF}} <$ 9 ms^{-1} range. It also shows how WS decrease inside the canyon, and in a different manner in the upstream and downstream sections. An interesting finding is that WS at 3 m were larger than WS at 9 m, especially near the upstream end. The cause is the closeness of 9 m SA to the center of the region of recirculation. In the downstream end WS at both in-canyon levels exhibit similar magnitudes again associated with more efficient mixing of momentum. WS above the canyon are smaller in the downstream end due to enhanced mixing with low-momentum in-canyon air, as the flow progresses along the canyon top.

Linear fits are also presented to relate canopy flows to reference flows. The slopes show that in-canyon WS were 5-20% of $\overline{WS_{REF}}$. Above the canyon, flow decelerates due

to turbulent mixing from ~70% of $\overline{WS_{REF}}$ to ~ 45% of $\overline{WS_{REF}}$ in the downstream end. Since $\overline{WS_{REF}}$ was measured at 10-m and away from the urban site

Linear fits were also established as a function of canyon top winds measured over the upstream side (i.e. at $5h/4$) and are presented in Figure 6.7. Establishing relationships to estimate in-canyon WS is important as WS plays an important role in the parameterization of SHFX inside the canyon (e.g. equation 2.45; Kusaka et al., 2001; Barlow et al, 2004).

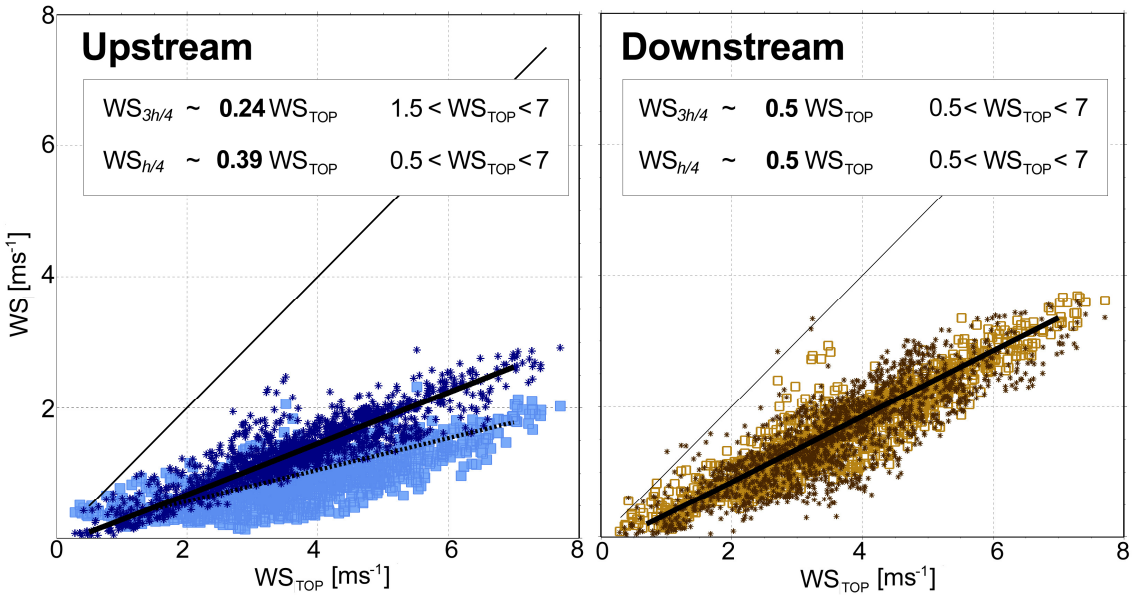

Figure 6.7. In-canyon WS as a function of above-canyon WS ($WS_{5h/4}$=WS_{TOP}).

WS in all regions inside the canyon with the exception of the upper upstream end can be expressed as linear functions of above-canyon WS ($WS_{5h/4}$=WS_{TOP}). Figure 6.7 shows that in-canyon WS decrease along the recirculation region. WS in the downstream end are ~50% smaller than above the upstream canyon and have similar magnitudes at both levels. The main difference is WD, where the lowest level exhibits larger zonal components. WS in the lower downstream end are ~40% smaller than above the upstream

canyon. And decrease more in the upper upstream section, however the latter relationship is not linear.

WD is explored as a function of $\overline{WD_{REF}}$ in Figure 6.8. It shows the region of recirculation under cross-canopy $\overline{WD_{REF}}$, and how it transitions into along-canyon WD at all levels when $\overline{WD_{REF}}$ becomes parallel to the canyon. Under other $\overline{WD_{REF}}$, in-canyon WD is determined by the small deviations from cross-canopy WD.

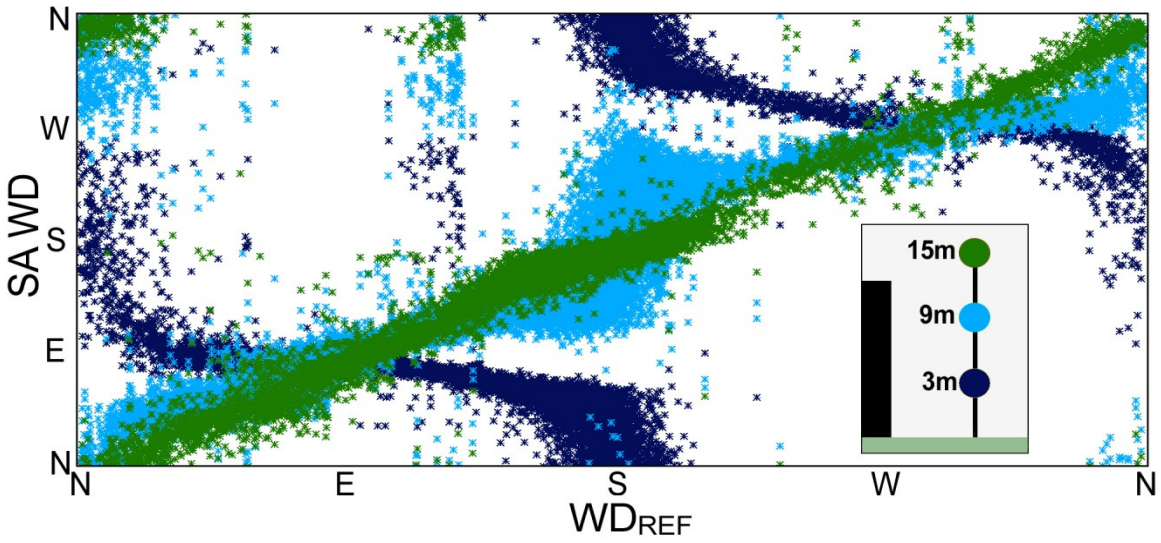

Figure 6.8. SA WD at different levels as a function of reference WD.

For example, when a small easterly component is present in $\overline{WD_{REF}}$, WD inside the canyon exhibit larger easterly components, especially closer to the ground. The canyon funnels the flow and the primary exit region becomes the downstream lateral end of the canyon. A schematic example is provided in Figure 6.9, which shows how under SSE $\overline{WD_{REF}}$ the flow circulates inside the canyon but ultimately exits along the western end. Darker arrows indicate foreground wind vectors (eastern end of the canyon) and lighter colors indicate background vectors (western end of the canyon). Arrow length suggest WS.

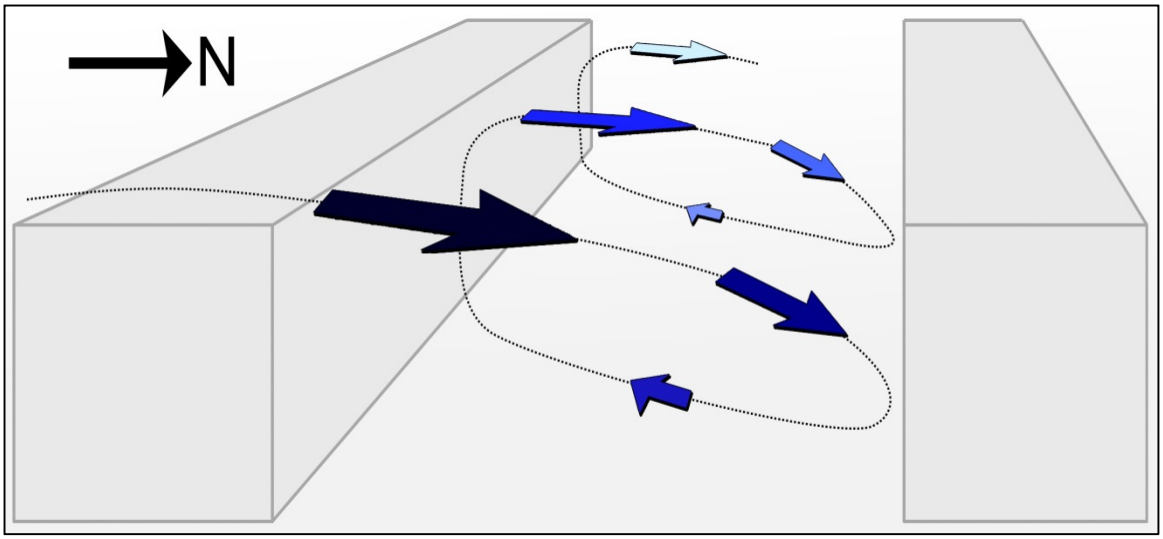

Figure 6.9. Scheme of in-canyon circulations during period with SSE $\overline{WD_{REF}}$.

6.2. Selection of interesting cases under southerly flow.

Selected diurnal cycles of SHFX under different flow and stabilities are here presented. Timeseries consist of complete diurnal cycles of five minute averages that start at 06 LST, or near sunrise time. Each figure contains five panels. The uppermost panel shows SHFX from three SA located above the canyon and the SLS. The second panel from the top shows SHFX from four SA located inside the canyon and from the SLS. A scheme with the location of the SA analyzed in the two upper panels and the symbols used in the plots is provided in Figure 6.1. The third panel shows reference WS and WD measured at the Norman MESONET site and at a height of 10-meters. The fourth panel shows solar radiation (yellow), periods with precipitation (green marks at the top) and stability (red for unstable and blue for stable). Stability was calculated using height above ground z and L calculated from SA data. The last panel shows MESONET air temperatures measured at 1.5 (light blue) and 9 meters (dark blue) and their difference (black).

6.2.1. Clear skies and moderate southerly winds.

Figure 6.10 illustrates a diurnal cycle measured under clear skies and moderate southerly winds.

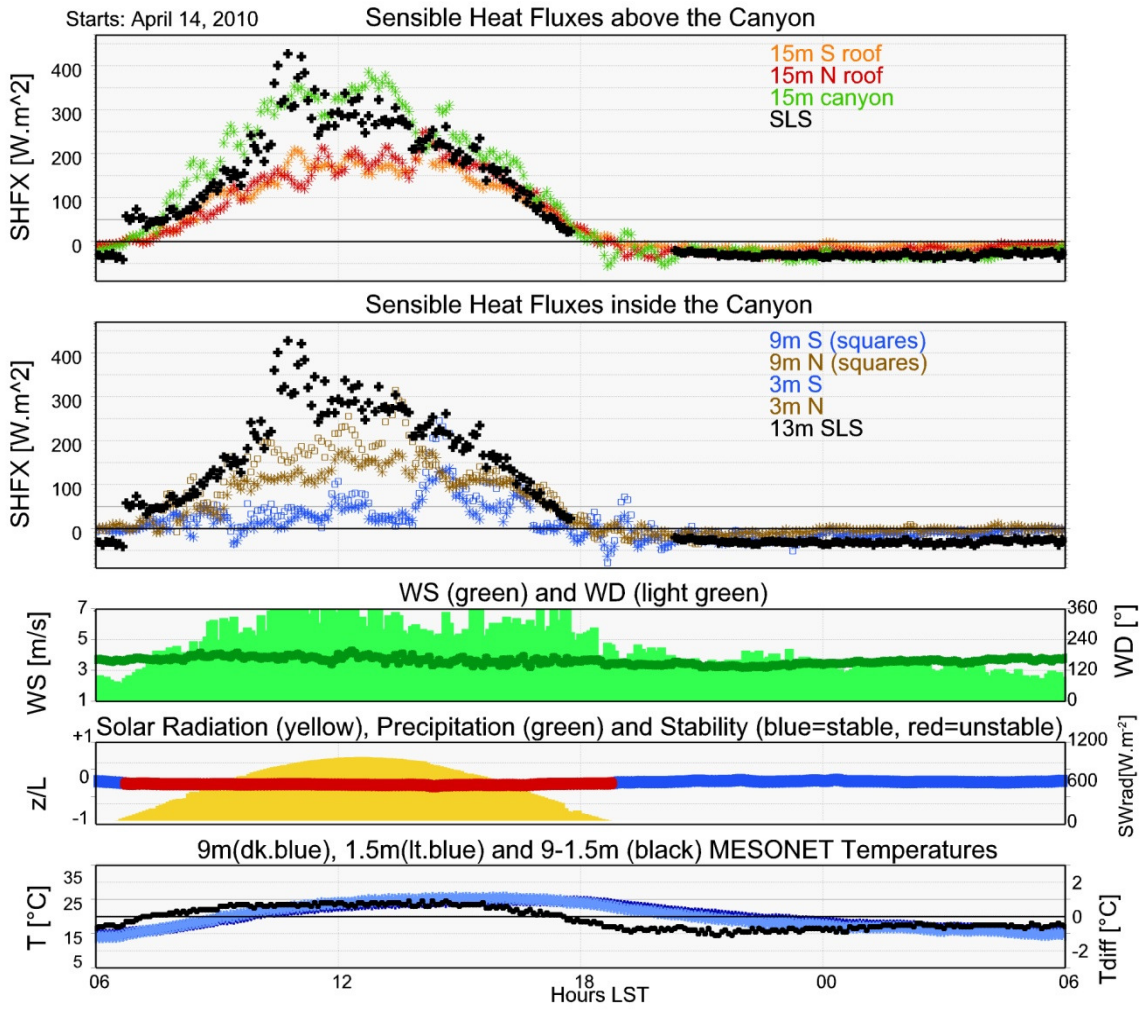

Figure 6.10. Diurnal cycle under moderate southerly winds and clear skies.

Clear skies are evidenced by the almost perfect sinusoidal behavior of the solar radiation curve. Wind direction was nearly constant with the slight diurnal oscillation between SSW flow during daytime and SSE flow at night. This oscillation is common in Central Oklahoma and is related to enhanced mixing with overlying westerly flow during

daytime followed by BL decoupling at night. The diurnal cycle of WS also reflects the effects of turbulent mixing with overlying higher-momentum air. Daytime values (4-7 ms^{-1}) were higher than nighttime ones (2-4 ms^{-1}). Skies were clear which reflects in the almost perfect sinusoidal behavior of the solar radiation curve. These weather conditions lead to the expected unstable/stable regimes during daytime/nighttime.

SHFX behaved in accordance to the diurnal cycle of solar radiation, but differences were observed between masts. The portion of the canopy that behaved the closest to the diurnal cycle of solar radiation were the rooftops (red and orange curves), with the exception of a slight delay on the occurrence of SHFX maxima, associated with the release of heat stored by the buildings. Above the canyon-top (green curve) the behavior is slightly different. The fluxes are not only larger in magnitude but the peak in SHFX occurs earlier in the day, which is confirmed by SHFX measured by the SLS (black crosses). The early peak in SHFX is associated with the peak in WS measured during the late morning. The measurement of larger values of SHFX inside the canyon is associated with increased turbulent mixing over the canyon than at the same height but above rooftops. This process is caused by the penetration of high-momentum air from the shear layer, which will be discussed with more detail later in the document.

SHFX inside the canyon exhibit a slightly different behavior but, in general, similar to the simulations and model described by Barlow et al. (2004) and by Harman et al. (2004). SHFX magnitudes are smaller associated with decreased velocities inside of the canyon. Near the downstream wall (north wall in this case) SHFX behavior resembles somewhat that measured over rooftops and over the canyon top. An early afternoon maximum (instead of a morning one) suggests the effects of heat release by the building walls. These effects were enhanced by the orientation of the building walls (i.e. south-

facing), which were exposed to direct sunlight during an extensive period of time. Turbulent mixing with higher momentum air that penetrated the area from the top of the canyon leads to large vertical velocities near the downstream wall that decrease towards the ground. This is reflected not only on the presence of larger SHFX in the higher level, but by the resemblance of the 9-m curve to that measured over the canyon top.

SHFX near the upstream wall (south wall in this case) behave in a different manner. Yet positive during daytime, SHFX magnitudes are much lower than those observed over the rest of the canopy. This is also consistent with the findings described by Barlow et al. (2004) and by Harman et al. (2004). The low magnitudes are associated with the presence of low-momentum flow in this section of the canopy, associated with a region of recirculation that develops near the upstream wall.

6.2.2. Partly cloudy skies.

Figure 6.11 shows a similar case but measured under variable cloudiness. All SHFX measured over the canopy (top panel) and those near the upper downstream wall (brown squares, second panel) behaved in close agreement with the diurnal cycle of incoming solar radiation. The behavior of in-canyon SHFX near the upstream wall, yet consistent in the vertical, was different to the rest of the canopy. In some instances upstream wall SHFX decreased once those measured by the other masts increased; in other instances their behavior was similar. Flux magnitudes, however, remained low and the fluxes became occasionally negative with values that oscillated between -50 and +50 $W.m^{-2}$. Flux reversal suggest the periodic occurrence of vertical temperature gradient reversals. These are associated with the advection of relatively warm air from the rooftop

region over relatively cool in-canyon air. Furthermore, local temperature gradients that lead to enhanced variability of SHFX are favored by the presence of scattered clouds.

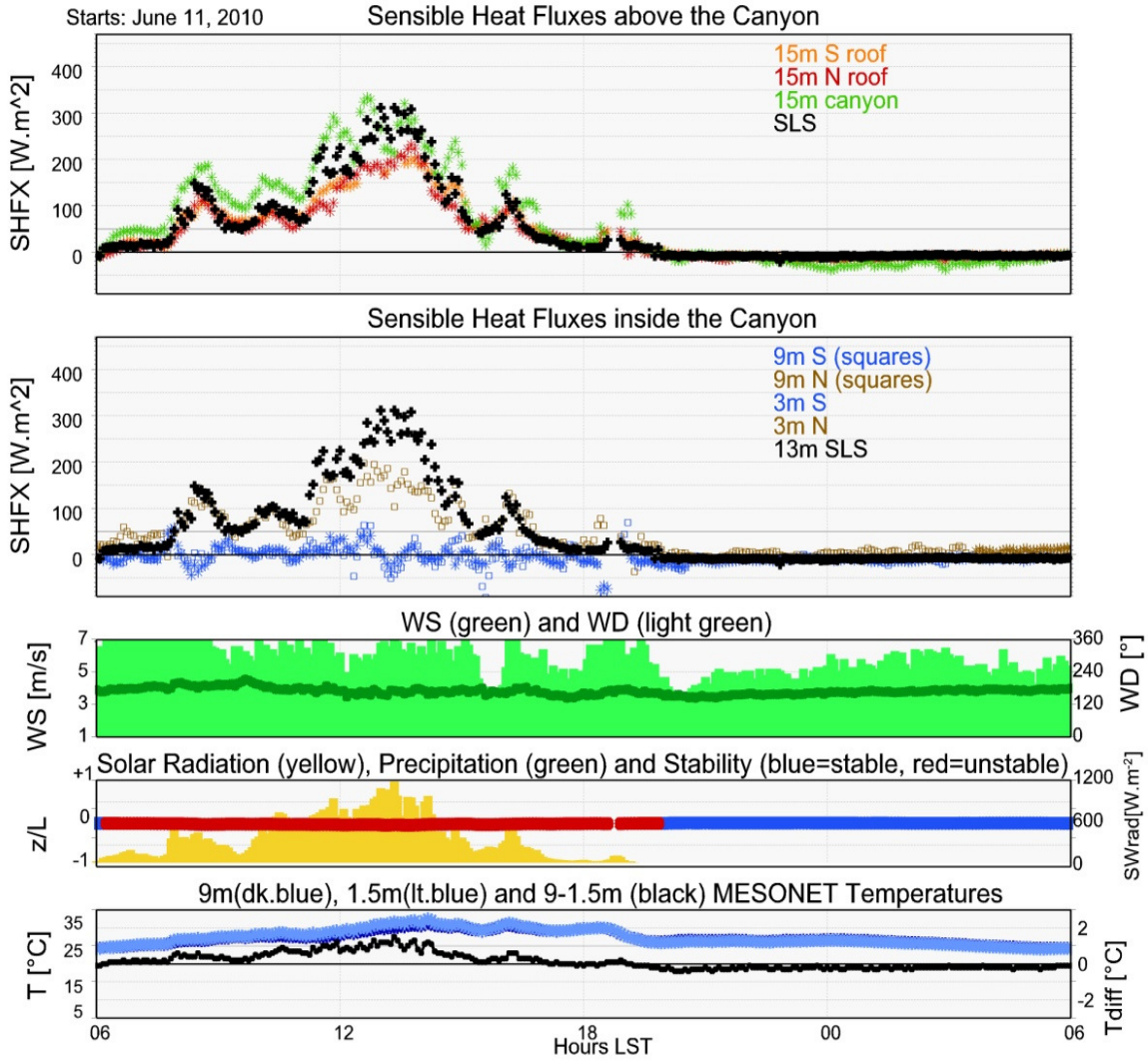

Figure 6.11. Diurnal cycle under moderate southerly winds and partly cloudy skies.

Daytime SLS SHFX behaved in close agreement with those measured above rooftops and above the canyon top. Again, their magnitude laid in between that of rooftop SHFX and that of canyon-top SHFX.

6.2.3. Effect of increasing wind speeds.

Figure 6.12 shows data collected during two consecutive days in which the only remarkable difference was an increase in wind speed during daytime. The response of SHFX varied upon location within the canopy. Above rooftop level, the increase was larger over the canyon top (~80-100%) than over rooftops (~50-70%). An even larger increase was observed in SLS SHFX (~100-120%). These results reflect enhanced turbulent mixing with high momentum air located in the shear layer present in all regions. The increases are larger over the canyon, however, since shear layer air is also brought downwards into the canyon in the form of transient high-momentum injections (Harman et al. 2004). The increase is the largest in SLS data since the sampled region extends further into the shear layer.

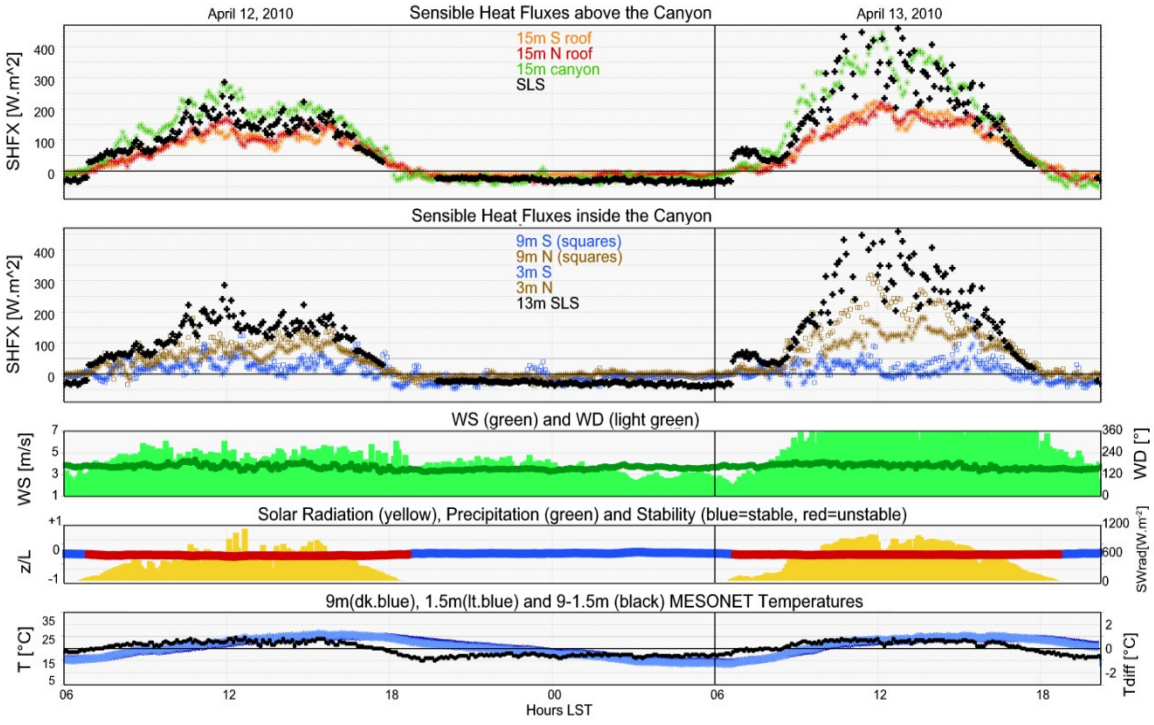

Figure 6.12. Consecutive days with similar weather conditions aside from different daytime wind speeds.

Inside the canyon, the increase also was different depending on the location. The largest increase was observed on the downstream end, especially away from the surface (brown squares) with values in the order of 100-120 %. Similar percentual increases to those observed near the shear layer (i.e. SLS data) support the findings from Harman et al. (2004) that state that high-momentum shear layer air penetration into the canyon is mostly concentrated towards the downward end. Shear layer flow that enters the canyon progresses downward into the lower canyon and mixes with lower-momentum air. This produces a decrease in velocities which constrains the increase in lower-canyon SHFX. SHFX near the downstream end remain virtually unchanged.

6.2.4. Windy and cloudy environment.

Figure 6.13 shows a diurnal cycle under strong southerly winds and cloudy skies. These conditions lead to stability stratification that approaches neutrality. All measured SHFX, except those from the upstream section of the canyon behaved in agreement with the diurnal cycle of solar radiation. SLS SHFX magnitudes were closer to the SHFX measured in the roof than to those measured over the canyon, which suggests the possibility that the effects from the roofs dominate during periods with strong winds and weak solar radiation rates.

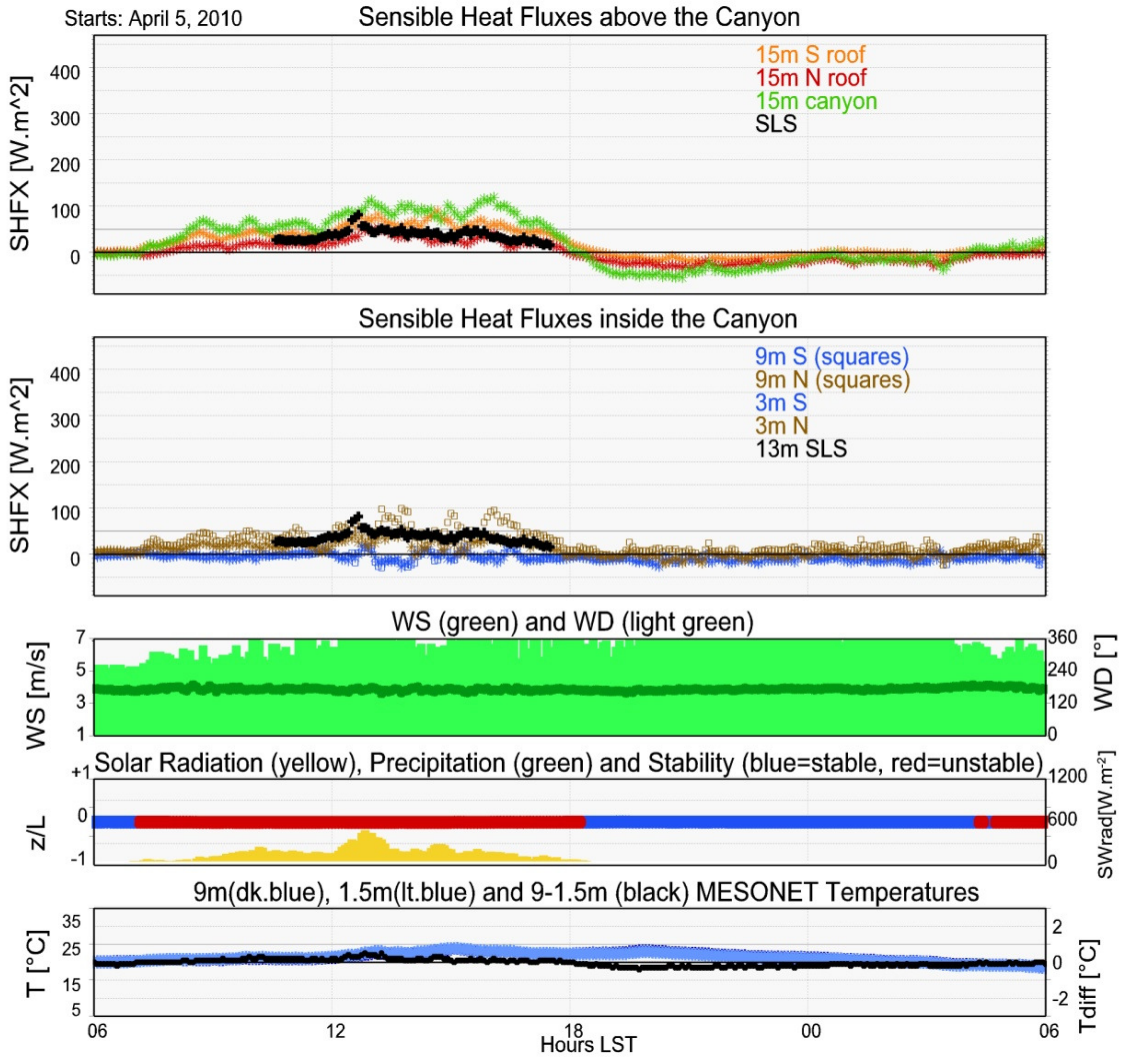

Figure 6.13. Diurnal cycle under strong southerly winds and cloudy skies.

6.3. Turbulent transfer under other wind directions.

6.3.1. Northerly flow.

Figures 6.14 and 6.15 summarize four cases under northerly reference flow. The cases shown in Figure 6.14 were collected under moderate winds and clear skies (a), and under weaker winds under partly cloudy skies (b). The former is associated with larger daytime SHFX due to larger surface heating and larger vertical velocity fluctuations. The cases in Figure 6.15 were both collected under windy conditions and allow to explore the effects of solar radiation under similar wind regimes. Figure 6.15b shows particularly distinct behaviors between platforms and larger SHFX magnitudes. This is a response to a combination between strong winds and large solar heating since this was the only panel with clear skies during springtime, when solar zenith angles are maximized. Furthermore, the data were collected after a frontal passage, which is associated with larger daytime SHFX due to the presence of a cool air mass over a relatively warm surface.

Both figures show SHFX behavior that is almost a mirror of what occurs under reference southerly winds. Discrepancies can be attributed to asymmetries caused by (i) solar radiation angles and associated shades and (ii) interactions between the flow and the roughness elements located upwind. Also, all figures confirm that SHFX over the canyon nearly double or triple in magnitude those located inside the canyon with the exception of the upper downstream end. As suggested by Oke (1987) and Barlow et al. (2004), the ventilation region is located near the downstream end of the canyon. High SHFX from above-canyon air mix with in-canyon air which leads to larger magnitudes than those found in other portions of the canyon.

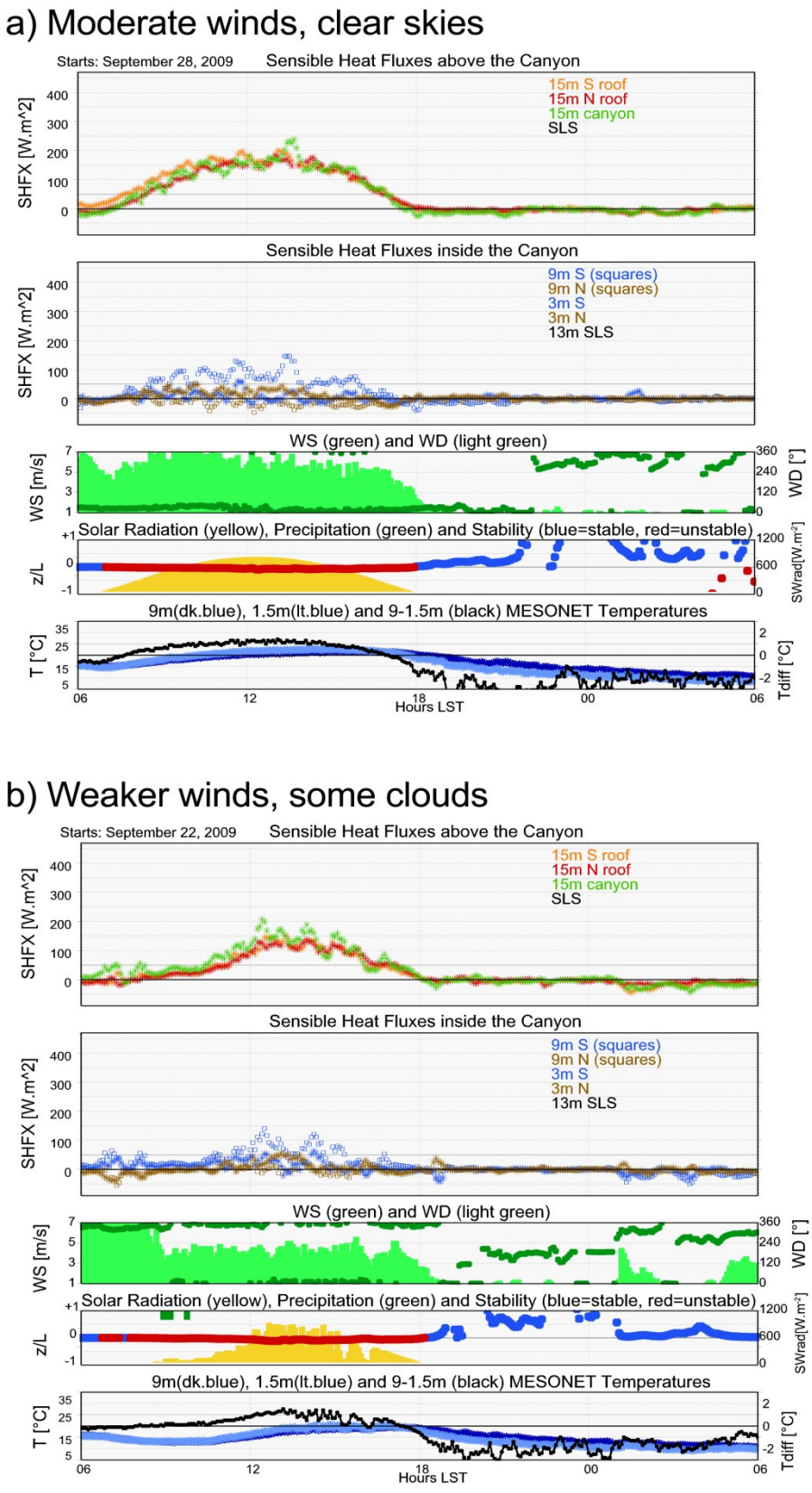

Figure 6.14. Selected diurnal cycles measured under northerly flow.

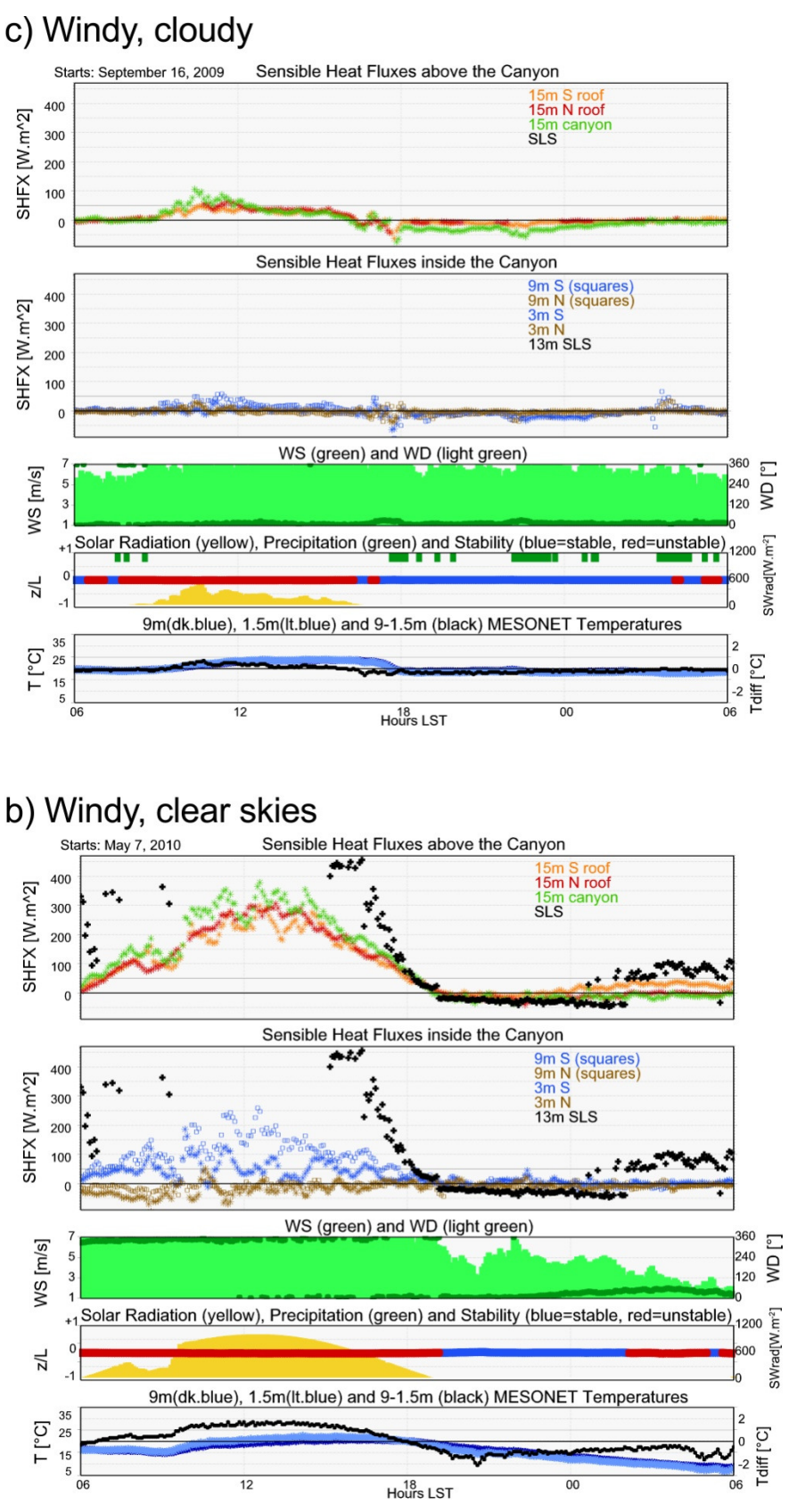

Figure 6.15. Selected diurnal cycles measured under northerly flow.

There is also a WS dependence of canyon-top relative to rooftop SHFX. In general, canyon-top fluxes are larger than those measured over rooftops. The main physical mechanism behind this difference is advection of larger SHFX from the shear layer downwards into the canyon, as observed under southerly flow conditions as well. Differences between the upstream and downstream rooftops also exist. They do not become clear until WS and solar radiation become both large (e.g. Figure 6.15b). During these situations, SHFX over the downstream roof become smaller due to the effects of ventilation from the canyon: lower SHFX in-canyon air is both advected and mixed-in into the downstream rooftop region.

SHFX advected into the canopy under northerly flow conditions were smaller than those advected under southerly flows of similar speed. These differences can be partly attributed to the characteristics of the fetch that surrounds the measurement site. SHFX are smaller under northerly flows because they are advected from a relatively urbanized area, characterized by lower momentum and more homogeneous vertical temperature gradients than those advected from the less urbanized southern tier. Large SHFX (i.e. larger than 300 Wm^{-2}) are only observed during the post frontal case,

The variability of SHFX measured over canyon-top and downstream rooftop was larger than over the upstream roof. This reflects the effects of turbulent mixing between shear layer air and that in the upper portion of canyon and its downstream advection by the flow (i.e. the upstream roof mast is located close to the edge of the canyon, so it feels mostly the effects of the northern rooftop). This link can be verified by a closer behavior of SHFX in this section of the canyon when compared against the values measured over the upstream roof.

The behavior inside the canyon was, again, almost a mirror of that observed under southerly flow cases. The largest SHFX were observed near the downstream wall and away from the ground. They were smaller in magnitude but behaved similarly to those measured over the downstream roof. SHFX in the lowest part of the canyon were particularly sensitive to a combination of large solar radiation rates and strong wind speeds. With the exception of panel d, the downstream lower portion of the canyon exhibited very low SHFX magnitudes and in some instances, negative values (-20 to +50 $W.m^{-2}$). In the upstream section of the canyon sensible heat fluxes magnitudes were generally very small (< 50 $W.m^{-2}$) and, in some instances, negative. The latter was particularly true in panel d. This suggest the development of a temperature inversion with warmer air being likely advected away from the northern roof.

SLS data was available during this period but SHFX were too large. This is associated with an underestimation of d_0 for the northern quadrant, which should have larger values after the flow interacts with the tall buildings present in the northern campus and central Norman urban area. This suggests that SLS measurements cannot necessarily be relied upon for all wind directions, when made too close to the canopy, issue that will be discussed with more detail in section 6.5.

6.3.2. Non-perpendicular wind directions.

Figure 6.16 illustrates cases measured under non-perpendicular reference flow conditions. Panel a illustrates a case with angled reference flow, from the NE; and panel b a case with westerly or along-canyon flow. Scintillometer data will, again, not be discussed in this section. It is important, however, to point out that problems with the underestimation of d_0 are also present for NE winds.

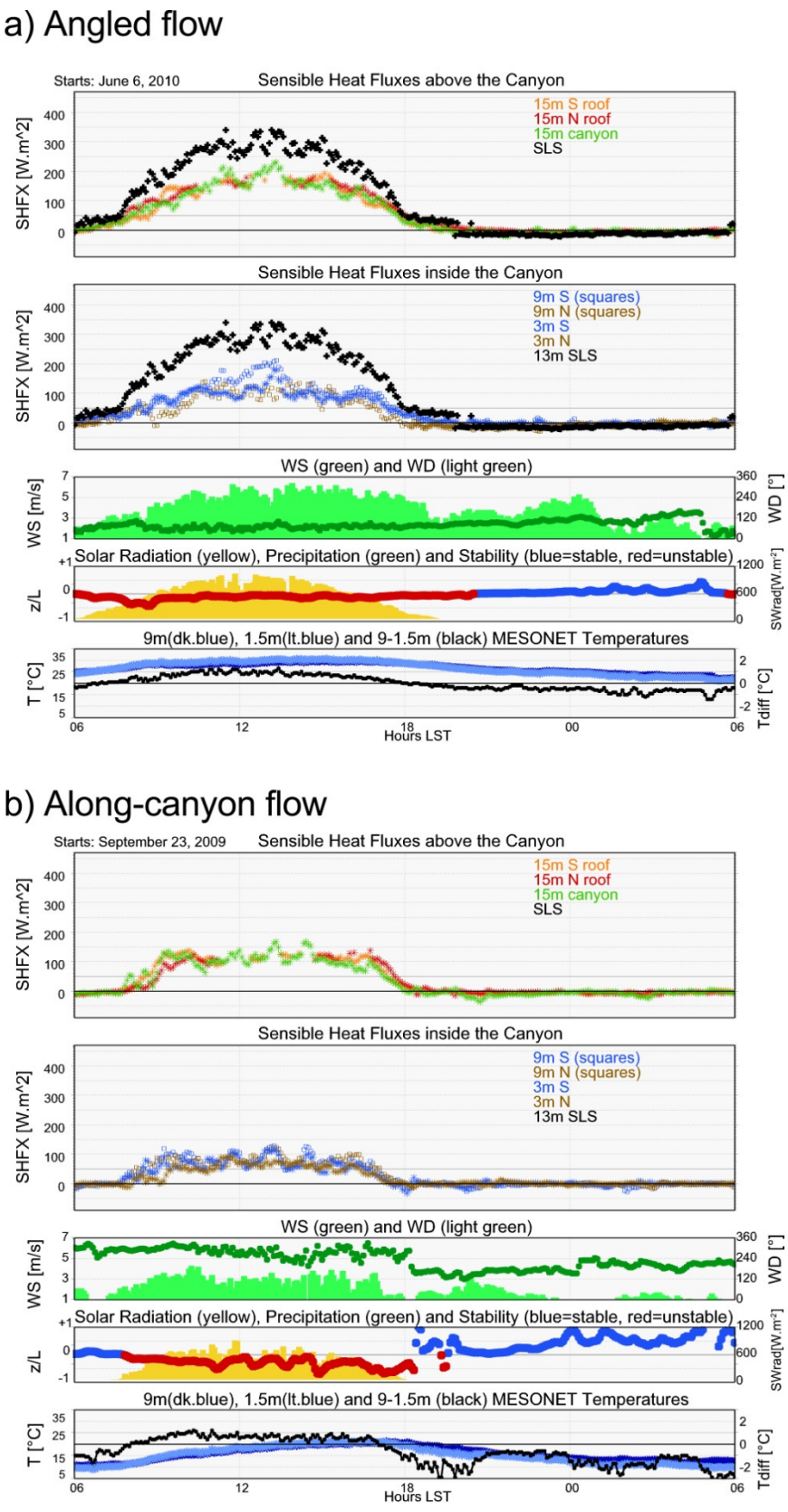

Figure 6.16. Non-perpendicular flows.

Results suggest that under non-perpendicular reference flow cases, SHFX over rooftops and canyon-top exhibit similar magnitudes and behavior. In contrast with what was observed under southerly flow conditions, canyon-top fluxes were not larger in magnitude. Parallel flows are associated with smaller vertical velocity fluctuations due to reduced interactions with the roughness elements along a given streamline. Accordingly, the downward transport of high-momentum air found in the shear layer is not as large as during cross-canopy flow conditions. Inside the canyon, SHFX are smaller and comparable in magnitude in all sections of the canyon.

6.4. Sensible heat fluxes upon wind speed and solar radiation.

The behavior of SHFX with WS and solar radiation is here explored. A cross section with four selected southerly flow cases is presented in Figure 6.17. The numbers plotted are, in order of increasing size, SHFX in Wm^{-2}, WS in ms^{-1} and SHFX scaled by WS in $Wm^{-1}s^{-1}$. Colored circles represent SHFX and both their size and darkness are proportional to SHFX magnitude. The length of horizontal bars indicate WS.

Under periods of strong radiation, the largest SHFX were measured at the canyon-top. These were followed by the roofs, downstream canyon, lower canyon and finally the upstream section. It is important to note that the canyon is characterized by vegetation instead of a paved surface, so SHFX should be smaller than those expected over standard canyons. When solar radiation is small, the distribution of SHFX inside the canyon is a function of WS, with higher values in the upstream section when WS are weak.

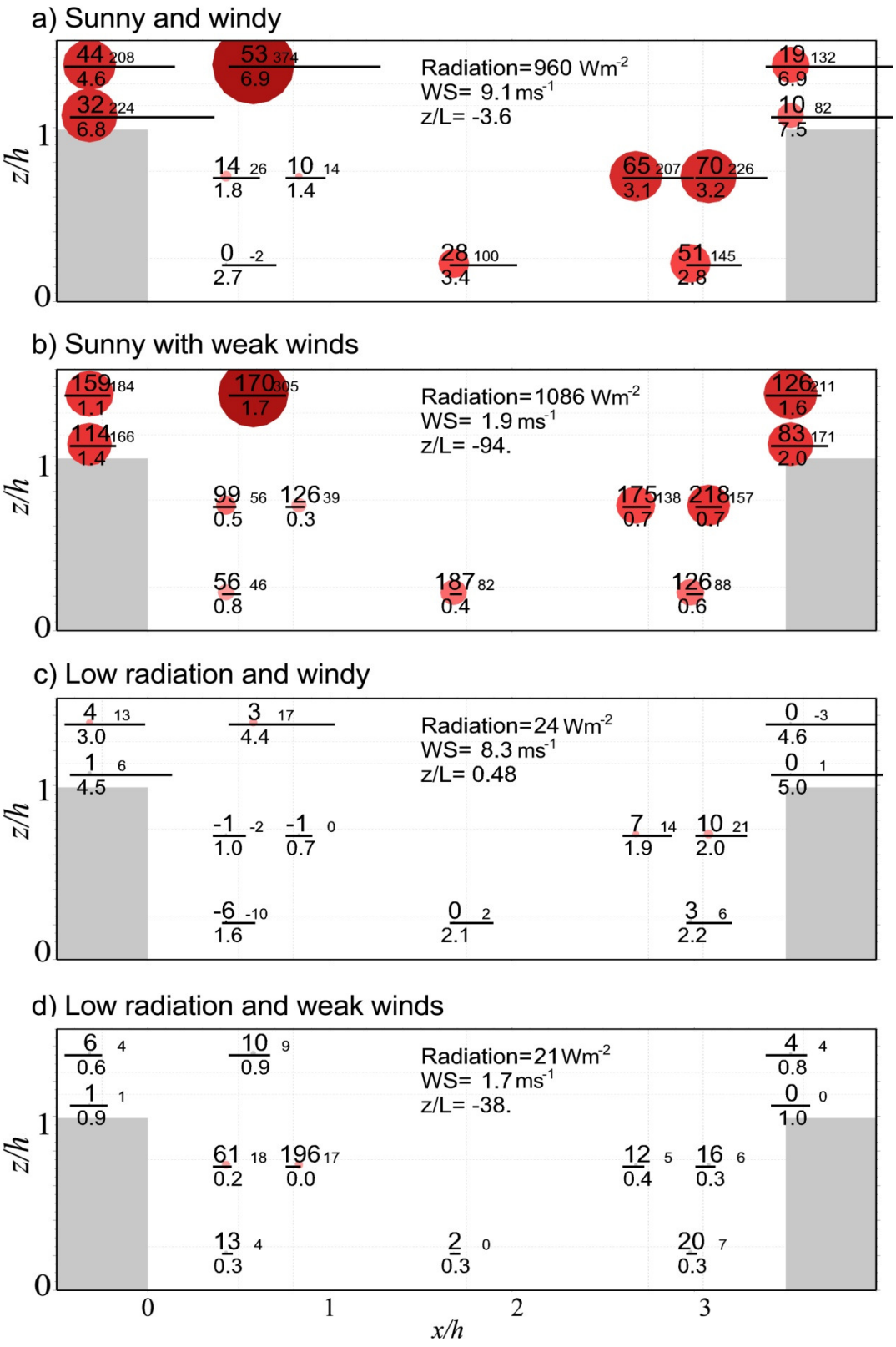

Figure 6.17. SHFX, WS and SHFX scaled by WS under contrasting WS and solar radiation scenarios.

Panels a and b, measured under periods of strong radiation, are first analyzed. Fluxes are larger in the shear-layer associated with higher velocities, especially above the canyon where higher-momentum air is advected from above. SHFX in the downstream roof are smaller, especially under cases with very strong winds where enhanced turbulent mixing diffuses vertical gradients. Inside the canyon, the behavior is very similar to that described by Barlow et al. (2004) and Harman et al. (2004), with larger SHFX in the downstream wall and very small values in the upstream section. The upstream/downstream differences for this case increase with WS.

The expressions used in Harman et al. (2004) based on the bulk aerodynamic formulation allow to relate a flux measurements with aerodynamic resistances via:

$$F_X = \Delta\bar{X}/r_X \tag{6.1}$$

which, combined with equations (2.45) and (2.46) yields to the following proportionality relationships inside the canyon (6.2) and in the shear layer (6.3):

$$F_H \sim \Delta\bar{T}\,\langle\bar{U}(z)\rangle \tag{6.2}$$

$$F_H \sim \Delta\bar{T}\,u_*^2\,/\Delta U \tag{6.3}$$

Equation (6.2) suggests that the parameterized in-canyon flux of sensible heat F_H is proportional to the local vertical temperature gradient $\Delta\bar{T}$ and to the spatially-averaged WS at a given level $\langle\bar{U}(z)\rangle$. SHFX normalization by WS allows to infer the distribution and contribution of in-canyon vertical temperature gradients in SHFX values.

SHFX/WS (large numbers) were the largest near the upper downstream, followed by the canyon top. This is expected since advection plays an important role and brings large values of SHFX and momentum from the shear-layer region into the canyon.

Furthermore, the north side of the canyon receives direct solar radiation, which plays a role in the enhancement of vertical temperature gradients. The next facet in terms of large SHFX/WS values is the upstream roof followed by the downstream one. The latter exhibits smaller values due to gradient diffusion along the canyon top from turbulent mixing, and from ventilation. The upstream canyon showed the smallest SHFX/WS. These, however, varied largely upon WS which suggests that $\Delta\bar{T}$ in this section of the canyon are largely dependent on WS. Larger values are present during periods of weak winds, when mixing is smaller and vertical gradients are generally maintained. When WS become large, gradients diffuse and in some occasions even revert (e.g. panel c) when warmer air from the rooftop is advected over a cooler canyon.

The cases measured under small solar radiation rates (panels c and d) show a similar behavior and more sensitivity to WS. The distribution suggests the presence of a warmer layer near the center of the region of recirculation.

The behavior of SHFX under different WD combined with different atmospheric conditions is explored in figures 6.10 through 6.12. Accordingly, all variables presented are plotted as a function of reference WD. Upper/lower panels present data collected under high/low WS. Left panels show SHFX, central panels vertical velocity variance $\overline{w'w'}$ and right panels temperature variance $\overline{T'T'}$. Green is still used for canyon top data, orange for data from the south rooftop and red for data from the north rooftop.

a. Fluxes under strong solar radiation.

Figure 6.18 displays observations collected under periods with strong incoming solar radiation (> 600 W.m^{-2}). These periods are associated with strong surface heating and the consequent development of local temperature gradients between the diverse

surfaces present in the urban canopy. They are also associated with the middle of the day when the boundary layer is well developed. Strong solar radiation is associated with convective boundary layers, which are characterized by enhanced turbulent mixing and vertical extent. Interaction with high-momentum flow from above leads to relatively large values of momentum inside the BL, which are brought downwards by turbulent mixing and lead to larger wind velocities near the surface.

Figure 6.18 shows that the behavior of sensible heat fluxes is clearly a function of WD. This results from different interactions with the diverse roughness elements located around the measurement site. A nearly symmetrical plot would be expected if the fetch around the central courtyard were homogeneous. The only asymmetries would be related to the canyon-top anemometer placement, which was closer to the south than to the north wall. The surrounding fetch is, however, not homogeneous and the effect of surrounding elements is visible. Asymmetries that increase as a function of WS suggest the influence of large roughness elements located far away. An example can be seen in Figure 6.10 under strong W and NW flow. All measured variables show relatively large values for W and NW flow. These are caused by the wake of the OU Dormitories large building complex and by the presence of extensive parking lots in this direction. Wake turbulence is evidenced by large values of velocity variance $\overline{w'w'}$. Large temperature variance $\overline{T'T'}$ is partly explained by the presence of extensive parking lots to the west and north of the area. These asymmetries are less pronounced under periods with weaker winds when the influence of nearby elements dominates turbulent transfer.

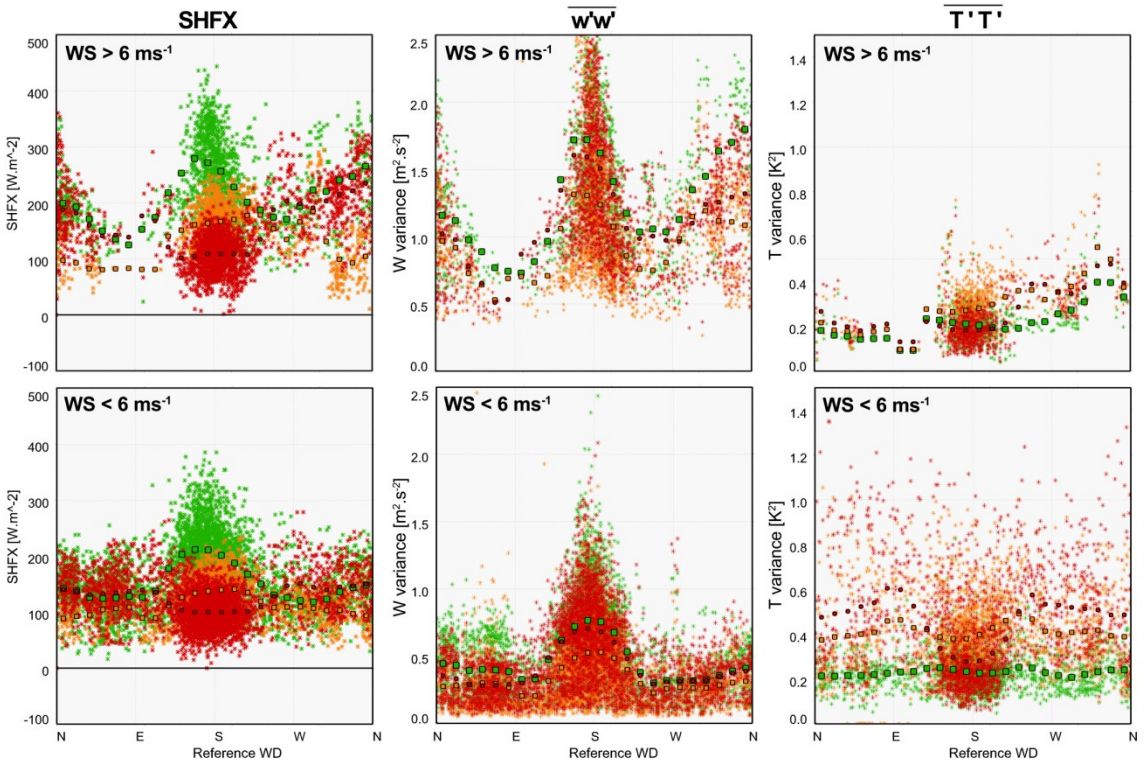

Figure 6.18. Role of WD and WS on sensible heat fluxes (left), vertical velocity variance (center) and temperature variance (right) during periods of strong solar radiation (> 600 W.m^{-2}). Canyon top (green), south roof (orange) and north roof (red) data are presented.

SHFX above the canopy behave differently depending on WD. Only under southerly flow, which is perpendicular to the buildings, canyon fluxes are larger in magnitude than those measured over rooftops. This is not evident under northerly flow periods. A partial explanation is the closeness of the canyon-top sonic anemometer to the southern wall (i.e. located at a distance of about 20% of the canyon width).

Nevertheless, some observations suggest that the effect of the upstream fetch is also important in the generation of differences between southerly versus northerly flow cases. One factor is the presence of enhanced $\overline{w'w'}$ under southerly flow that is present not only over the canyon-top but over both rooftops. This suggests the presence of a stronger shear layer under southerly wind directions associated with a more rural-like

boundary layer. Under northerly wind directions the flow has interacted with the Norman urban area which results in the arrival of a weaker shear layer. These results are also supported by the location of canyon-top SHFX maxima with respect to the south. The maxima under both weak and strong WS cases coincide with the upstream fetch characterized by the smallest roughness elements and paved surfaces (i.e. located to the south-southeast).

Whereas over the canyon SHFX are mostly explained by $\overline{w'w'}$, over rooftops $\overline{T'T'}$ dominates. Temperature effects particularly dominate under weak WS, when gradients are enhanced by weaker turbulent mixing. Under stronger wind speeds, the effects of $\overline{w'w'}$ dominate everywhere. Values of $\overline{T'T'}$, still larger over rooftops than over the canyon, decrease from enhanced mixing.

Under flow regimes that are perpendicular to the canopy, SHFX are larger over the upstream roof and are mostly explained by $\overline{T'T'}$. Whereas $\overline{T'T'}$ over the upstream roof is relatively large and dominated by rooftop thermals, that over the downstream roof is influenced by well-mixed air advected from the canyon.

Fluxes differ under flow regimes that are not normal to canyon orientation. Under parallel flow regimes, SHFX are lower over the canyon-top associated with a decrease in $\overline{w'w'}$. This decrease is also present over rooftops, but a local increase in $\overline{T'T'}$ favors a slight increase on SHFX under these conditions.

b. Weak solar radiation.

All cases with weak solar radiation (50-300 $W.m^{-2}$) are summarized in Figure 6.19. Whereas the effects of $\overline{w'w'}$. remain similar for the most part, the effects of $\overline{T'T'}$.

decrease from decreased surface heating. The effects of canyon shape on $\overline{w'w'}$. are, however, more evident. This can be explained by the arrival of a stronger shear layer from the north compared to the shear layer that arrives when the heating is larger. This behavior reflects the effect friction from thermal turbulence, which causes a decrease in the velocity of the flow over the Norman Urban area. Sensible fluxes are still highest under wind directions perpendicular to canyon orientation, but the differences are smaller than when solar radiation rates and surface heating are large. The effect of surrounding roughness elements is also evident under large WS.

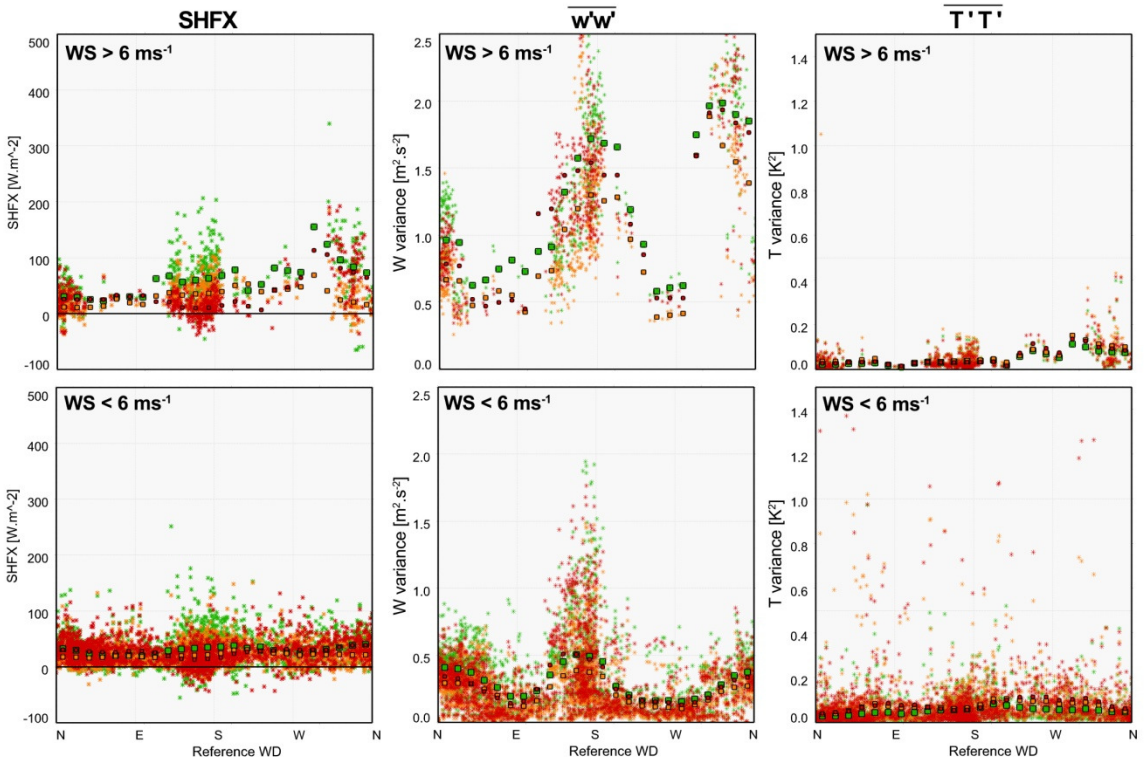

Figure 6.19. Role of WD and WS on sensible heat fluxes (left), vertical velocity variance (center) and temperature variance (right) during periods of low solar radiation (50-300 W.m^{-2}). Canyon top (green), south roof (orange) and north roof (red) data are presented.

7. SUMMARY AND CONCLUSIONS.

A SLS and several SA were used to study the TT of sensible heat in the UC and to explore the reliability of the SLS in such complex environment. To do so, the measurements were organized in two 3-month-long sub-urban campaigns and one 13-month-long urban campaign. The campaigns were all conducted in nearby locations and within 5 kilometers of the Norman MESONET site, for inter-comparison purposes.

The main goal of the sub-urban campaigns was to verify that SLS measurements were reliable. This was done by inter-comparing SLS and SA SHFX measured simultaneously over flat and homogeneous terrain for MOS validity. Some discrepancies were found, and attempts to correct them were made. The first attempt was to test the validity of $\varphi_\varepsilon(\frac{z}{L})$ by comparing SLS measurements with φ_ε derived from SA velocity spectra. Once corrections were established, however, their impact on SLS SHFX was minimal. Further analysis and discussion with Bram Van Kesteren and Oscar Hartogensis (personal communication, 2011) indicated that most of the discrepancies originated higher up in the algorithm and were associated with limitations in the representation of the refractive index spectrum proposed by Hill (1978). This spectrum, still the most reliable nowadays, has limitations on the DR that arise from the difficulty of measuring at such high frequencies. These limitations affect mostly l_0 and eventually SLS sensible heat fluxes. The analysis showed that the discrepancies are stability and WS dependent, and that can be overcome by the use of the corrective expressions for l_0 proposed in 4.15 and 4.16. The application of these corrections improved SLS fluxes positively.

Some discrepancies were also found in SLS C_n^2 data. These occur very close to neutrality, when scintillations are too small to be measured correctly by the SLS and

overestimation occurs. These could also be overcome with the corrective expression proposed in 4.17. The application of both corrections to l_0 and C_n^2 together lead to excellent agreement between SLS and SA fluxes. Looking into the Hill spectrum and discrepancies on the variance measurements themselves is still recommended.

Once ready to operate over the urban environment, additional considerations were necessary for SLS data reliability. The most critical was the determination of appropriate values for d_0 and z', which showed to have a strong effect on the calculation of SLS turbulent fluxes. This limitation is again tied to the applicability of MOS in scintillometry that has a large impact since MOS relies on functions of z'/L. The estimation of d_0 in the urban environment is based on morphological approaches instead of micrometeorological ones, since the latter consider the characteristics of the roughness elements. Accordingly, d_0 was estimated using the Bottema (1995) method that is based on building and vegetation planar areas and heights. The method was successful to predict d_0 for some WD and captured the effects of canyon shape on d_0 but especially those of the surrounding environment. For some WD, however, d_0 was underestimated. This was partly due to the need of considering a broader domain for the calculations but also due to limitations associated with MOS applicability. The findings suggest that SAS can be operated immediately over the UC but their data is reliable for only certain WD upon the surrounding fetch. Increasing measurement height is recommended to increase reliability.

Aside from exploring scintillometer measurement applicability, TT of sensible heat in the UC was also investigated. The urban location selected consisted of a street canyon-like structure with dimensions of W~3.5h. Site selection was based on building geometry, east-west canyon orientation and the feasibility of attaining the proper permissions for instrument installation and operation. A site limitation was the ground

cover, which consisted of grass and scattered small trees instead of pavement. This type of surface cover is usually associated with smaller values of lower-canyon diurnal SHFX than those expected over pavement since a larger percentage of the available energy is usually partitioned into latent heat flux.

An idealized sketch that represents a cross section of the urban canyon sampled is presented in Figure 7.1, and will be referred to in the following.

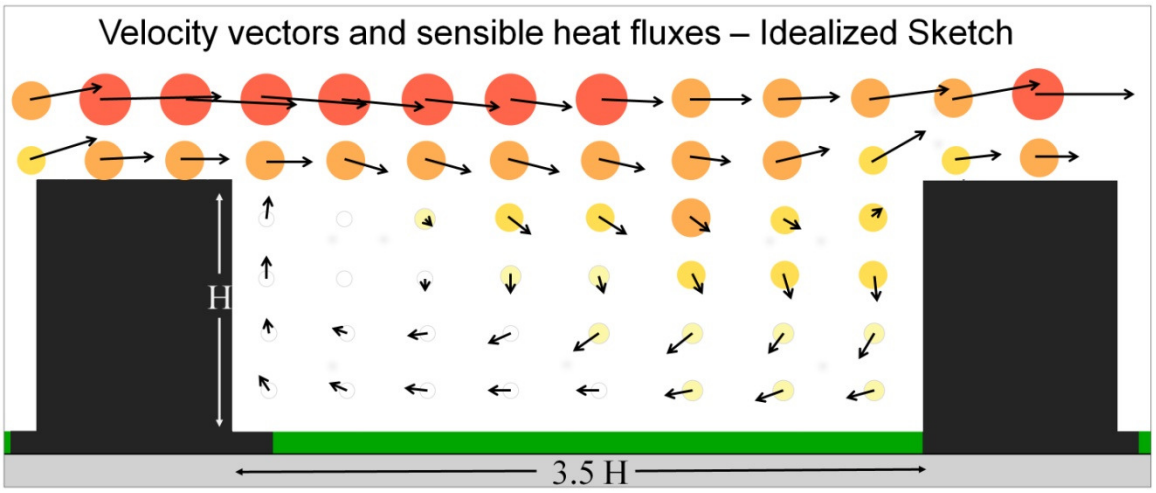

Figure 7.1. Schematic representation of average wind vectors (arrows) and average daytime sensible heat fluxes (circles). Magnitudes are represented with arrow and circle size.

Velocities measured during the urban campaign confirmed the presence of a shear layer above the UC that separates in-canopy low-momentum air from larger velocities found above. Turbulent mixing in this layer largely modulates the circulations inside and downstream from the canyon. Under perpendicular reference flow conditions, a region of recirculation develops and covers most of the canyon with the exception of the downstream end where ventilation occurs. The region of ventilation remained away from the ground most of the time. This type of in-canyon flow regime was classified by Oke (1987) as Wake Interference Flow Regime. The primary region for flow entrance was

through the canyon-top where the largest downward vertical velocities occurred in the windward end. The data also suggested that the primary exit regions were located in the eastern and western ends of the canyon, and that central canyon WD were for the most part regulated by the direction of the reference flow.

SHFX showed a distinct distribution and behavior that were functions of WD, WS and stability; but also highly modulated by the geometry of the canyon and the surface cover. Advection and diffusion played an important role and was evidenced by the distribution of SHFX. This was mostly due to small vertical velocity perturbations found in the low-momentum in-canyon air, but was exacerbated by the contrasting surface covers between the roof materials (i.e. characterized by rapid heating and cooling) and the often shaded and moist grass cover from the canyon (i.e. characterized by slower heating and cooling). In some instances, daytime temperature gradients reversed in the upper upstream end of the canyon especially when warm and well mixed rooftop air was advected over relatively cool shaded in-canyon air under strong WS. These large velocity and thermal differences lead to large gradients near the UC top. The scintillometer was placed only a few meters above the strongest gradients, but the data revealed that it may have been operated too close to the surface. These findings suggest that a constant flux layer was not often present at scintillometer height and supports the previous findings that increasing measurement height is largely recommended.

Fluxes inside the canopy exhibit complex two-dimensional distributions with very low magnitudes near the ground and towards the upstream side, and increasing magnitudes towards the upper windward end. The distribution is highly affected by advection by the canyon rotor and by diffusion caused by turbulent mixing. A good example is the diffusion of the large SHFX gradient that forms near the upstream top of

the canyon as the flow progresses along the canyon and mixes with lower-SHFX in-canyon air. This results in weaker gradients and smaller SHFX magnitudes above the canyon downstream end.

As expected, flow interactions are a function of reference WD. Across-canyon flows lead to stronger SHFX over the lee part of the canyon than at a similar height located over rooftops. This was mostly caused by enhanced vertical velocity perturbations from the downward mixing of momentum into this region. Yet SHFX decrease near the downwind end as mixing occurs with cooler and low-momentum in-canyon air.

The effects of surrounding roughness elements was also evident. SHFX were larger above the canyon when flow originated from the southern quadrant, characterized by sub-urban and rural environments; than when the flow originated from the northern quadrant, characterized by larger roughness elements from the Norman urban area. These results suggested that the flow that arrives from the urban quadrant is characterized by smaller vertical gradients due to the effect of larger roughness elements. Incoming velocities were even smaller under the presence of large solar radiation, which evidences the effects of thermal turbulence on flow deceleration.

REFERENCES

Arnfield, J., Herbert, J. M., and Johnson, G. T, 1998: A Numerical Simulation Investigation of Urban Canyon Energy Budget Variations. *Proceedings of 2nd AMS Urban Environment Symposium, Albuquerque, New Mexico, November 2–7, 1998*, American Meteorological Society, pp. 2–5.

Arya, S. P., 1988: Introduction to Micrometeorology, *Academic Press*, 307 pp.

Arya, S. P., 1999: Air Pollution Meteorology and Dispersion, *Oxford University Press*, 320 pp.

Azoulay, E., Thiermann, V., A. Jetter, A. Kohnle and Z. Azar, 1988: Optical measurement of the inner scale of turbulence. *J. Phys. D: Appl. Phys*. 41-44.

Baldocchi, D., 2003: Assessing the eddy covariance technique for evaluating carbon dioxide exchange rates of ecosystems: past, present and future. *Global Change Biology*, **9**, 479-492.

Barlow, J. F., Harman, I. N., and Belcher, S. E., 2004: Scalar Fluxes from Urban Street Canyons. Part I: Laboratory Simulation, *Boundary-Layer Meteorol.* **113**, 369–385.

Barlow, J. F. and O. Coceal, 2009: A review of urban roughness sublayer turbulence. *Technical Report 527. Met Office. Department of Meteorology, Reading University, UK*. 68 pps.

Boddy, J. W. D., R. J. Smalley, N. S. Dixon, J. E. Tate, and A. S. Tomlin, 2005: The spatial variability in concentrations of a traffic-related pollutant in two street canyons in York, UK - Part I: The influence of background winds. *Atmospheric Environment*, **39**, 3147-3161.

Berger, B. W., K. J. Davis, C. Yi, P. S. Bakwin, and C. Long, 2001: Long-term carbon dioxide fluxes from a very tall tower in a northern forest: flux measurement methodology. *Journal of Atmospheric and Ocean Technology*, **18**, 529-542.

Beljaars, A. C. M., P. Schotanus and F. T. M. Nieuwstadt, 1983: Surface-layer similarity under non-uniform fetch conditions. *Journal of Applied Meteorology*, **22**, 1800-1810.

Best, M. J., 2005: Representing urban areas within operational numerical weather prediction models. *Boundary-Layer Meteorology*, **114**, 91–109.

Bottema, M., 1995, Aerodynamic roughness parameters for homogeneous building groups - Part 2: Results. *Document SUB-MESO #23, Ecole Centrale de Nantes*, France, 80 pp.

Brock, F. V., K. Crawford, R. L. Elliott, G. W. Cuperus, S. J. Stadler, H. L. Johnson and M. D. Eilts, 1995: The Oklahoma Mesonet: A Technical Overview. *Journal of Atmospheric and Oceanic Technology*, **12**, 5-19.

Brown, M. J., 2000: Urban Parameterizations for Mesoscale Meteorological Models, in Z. Boybeyi(ed.), *Mesoscale Atmospheric Dispersion, Wessex Press*, 448 pp..

Businger, J.A., Wyngaard, J.C., Izumi, Y., and Bradley, E.F., 1971: Flux-Profile Relationships in the Atmospheric Surface Layer. *Journal of the Atmospheric Sciences*, **28**, 181-189.

Ca, V. T., Ashie, Y., and Asaeda, T., 2002: A k − ε Turbulence Closure Model for the Atmospheric Boundary Layer Including Urban Canopy, *Boundary-Layer Meteorology*,**102**, 459–490.

Campbell Scientific, 2010: CSAT3 Three Dimensional Sonic Anemometer. Instruction Manual. *Available online at http://www.campbellsci.com/documents/manuals/csat3.pdf*. 70 pps.

Castro, I. P. and Robins, A. G.: 1977, 'The Flow around a Surface-Mounted Cube in Uniformand Turbulent Streams', *J. Fluid Mech.* **79**, 307–335.

Chen F, Mitchell K, Schaake J, Xue Y, Pan H-L, Koren V, Duan QY, Ek M, Betts A. 1996. Modeling of land-surface evaporation by four schemes and comparison with FIFE observations. *Journal of Geophysical Research*, **101**, 7251–7268.

Chen, F., and J. Dudhia, 2001: Coupling and advanced land surface-hydrology model with the Penn State–NCAR MM5 modeling system. Part I: Model implementation and sensitivity. *Monthly Weather Review*, **129**, 569–585.

Chen, F., H. Kusaka, R. Bornstein, J. Ching, C.S.B. Grimmond, S. Grossman-Clarke, T. Loridan, K. W. Manning, A. Martilli, S. Miao, D. Sailor, F. P. Salamanca, H. Taha, M. Tewari, X. Wang, A. Wyszgrodzki and C. Zhang, 2011: The integrated WRF/urban modelling system: development, evaluation, and applications to urban environmental problems. *Int. J. Climatol.*, **31**, 273–288

Chin H. N., M. J. Leach, G. A. sugiyama, J. M. Leone, H. Walker, J. S. Nasstrom and M. J. Brown, 2005: Evaluation of an Urban Canopy Parameterization in a Mesoscale Model Using VTMX and URBAN 2000 Data. *Monthly Weather Review*, **133**, 2043-2068.

Christen, A., 2005: Atmospheric turbulence and surface energy exchange in urban environments. *Faculty of Science, University of Basel*. 140 pp.

Christen, A., E. van Gorsel, and R. Vogt, 2007: Coherent structures in urban roughness sublayer turbulence. *International Journal of Climatology*, **27**, 1955-1968.

Craig K. J. and R. D. Bornstein, 2002: Urbanization of numerical mesoscale models. *In: Rotach MW, Fisher B, Piringer M(eds) Workshop on urban boundary layer parameterisations. EUR 20355, (ISBN: 92-894-4143-7),* **119**, 17–30

Crawford, K. C., and H. R. Hudson, 1973: The Diurnal Wind Variation in the Lowest 1500 ft in Central Oklahoma: June 1966-May 1967. *Journal of Applied Meteorology*, **12**, 127-132.

De Bruin, H.A.R., Bink, N.J. and Kroon L.J.M., 1988: Surface fluxes under advective conditions. Workshop on "Measurement and parameterization of land-surface evaporation fluxes", 10.-21.10. Banyuls, France.

De Bruin, H.A.R., B. J. J. M. Van den Hurk and W. Koshiek, 1995: The scintillation method tested over a dry vineyard area. *Boundary-Layer Meteorology*, **76**, 25-40.

De Bruin, H. A. R., W. M. L. Meijninger, A. Smedman and M. Magnusson, 2002: Displaced beam small aperture scintillometer test. Part I. The Wintex data-set. *Boundary-Layer Meteorology*, **105**, 129-148.

De Ridder, K., and G. Schayes, 1997: The IAGL land surface model. *Journal of Applied Meteorology*, **36**, 167–182.

Dobre, A., S. J. Arnold, R. J. Smalley, J. W. D. Boddy, J. F. Barlow, A. S. Tomlin, and S. E. Belcher, 2005: Flow field measurements in the proximity of an urban intersection in London, UK, *Atmospheric Environment*, **39**, 4647-4657.

Dupont S. and P. Mestayer, 2006: Parameterization of the Urban Energy Budget with the Submesoscale Soil Model. *Journal of Applied Meteorology and Climatology*, **45**, 1744 – 1764.

Dupont S., T. Otte and J. K. S. Ching, 2004: Simulation of meteorological fields within and above urban and rural canopies with a mesoscale model (MM5), *Boundary-Layer Meteorology*, **113**, 111-158.

Dupont S. and P. Mestayer, 2006: Parameterization of the Urban Energy Budget with the Submesoscale Soil Model, *Journal of Applied Meteorology and Climatology*, **45**, 1744 – 1764.

Dyer A. J., and Hicks B. B., 1970: Flux-gradient relationships in the constant flux layer. *Quarterly Journal of the Meteorological Society*, **96**, 715-721.

Dyer A. J., 1974: A review of flux-profile relationships, *Boundary-Layer Meteorology*, **7**, 363-372.

Eliasson, I., B. Offerle, C. S. B. Grimmond, and S. Lindqvist, 2006: Wind fields and turbulence statistics in an urban street canyon, *Atmospheric Environment*, **40**, 1-16.

Feigenwinter, C., R. Vogt, and E. Parlow, 1999: Vertical structure of selected turbulence characteristics above an urban canopy. *Theoretical and Applied Climatology*, **62**, 51-63.

Feigenwinter, C., and R. Vogt, 2005: Detection and analysis of coherent structures in urban turbulence. *Theoretical and Applied Climatology*, **81**, 219-230.

Finnigan J. J. 2004. A Re-evaluation of long-term Flux Measurement Techniques. Part 2: Coordinate Systems. *Boundary-Layer Meteorology*, **113**, 1-41.

Finnigan J. J., R. Clement, Y. Malhi, R. Leuning and H. A. Cleugh, 2003: A re-evaluation of long-term flux measurement techniques. Part I: Averaging and coordinate rotation. *Boundary-Layer Meteorology*, **107**, 1-48.

Foken, T., 2003: Angewandte Meteorologie. *Springer, Berlin*, 289 pp.

Foken, T., 2006: Micrometeorology. *Springer, Berlin*, 306 pp.

Garratt, J. R., 1980: Surface influence upon vertical profiles in the atmospheric surface layer. *Quarterly Journal of the Royal Meteorological Society*, **106**, 803-819.

Garratt, J. R., 1992: The atmospheric boundary layer. *Cambridge Press*, 316pp.

Glickman, T.S., 2000: Glossary of Meteorology. *2d ed. American Meteorological Society*, 855pp.

Green, A. E., K. J., McAneney and M. S. Astill, 1994: Surface-layer scintillation measurements of daytime sensible heat and momentum fluxes. *Boundary-Layer Meteorology*, **68**, 357-373.

Grimmond, C. S. B. and Oke, T. R., 2000: Aerodynamic Properties of Urban Areas Derived from Analysis of Surface Form. *Journal of Applied* Meteorology, **38**, 1262–1292.

Grimmond, C.S.B., Salmond, J.A., Oke, T.R., Offerle, B. and Lemonsu, A., 2004: Flux and turbulence measurements at a densely built-up site in Marseille: Heat, mass (water and carbon dioxide), and momentum. *Journal of Geophysical Research*, **109**, 2-19.

Grimmond, C. S. B., 2006: Progress in measuring and observing the urban atmosphere. *Theor. Appl. Climatol.*, **84**, 3-22.

Harman, I. N., J. F. Barlow and S. E. Belcher, 2004: Scalar fluxes from urban street canyons. Part II: Model. *Boundary-Layer Meteorology*, **113**, 387-409.

Hartogensis, O. K., 2006: Exploring Scintillometry in the Stable Atmospheric Surface Layer. *WUR Wageningen UR. Promotors: Holtslag, Prof dr A.A.M., co-promotors: De Bruin, Dr H.A.R. Wageningen*, 228 pp.

Hill, R.J., 1978: Models of the scalar spectrum for turbulent advection. *Journal of Fluid Mechanics*, **88**, 541-562.

Hill, R.J. and Clifford, S.F., 1978: Modified spectrum of atmospheric temperature fluctuations and its application to optical propagation. *J. Opt. Soc. Am.*, **68**, 892-899.

Hill, R.J. and Lataitis, R.J., 1989: Effect of refractive dispersion on the bichromatic correlation of irradiances for atmospheric scintillation. *Applied Optics*, **28**, 4121-4125.

Hill, R.J., 1992: Review of optical scintillation methods of measuring the refractive-index spectrum, inner scale and surface fluxes. *Waves in Random Media*, **2**, 179-201.

Hill, R.J., 1997: Algorithms for obtaining atmospheric surface-layer fluxes from scintillation measurements. *J. Atmos. Oceanic Tech.*, **14**, 456-467.

Hoedjes, J.C.B.; Chehbouni, A.; Ezzahar, J.; Escadafal, R.; Bruin, H.A.R. de, 2007: Comparison of large aperture scintillometer and eddy covariance measurements: Can thermal infrared data be used to capture footprint-induced differences? *Journal of Hydrometeorology*, **8 (2)**, 144 - 159.

Högström, U.L.F., 1988: Non-dimensional wind and temperature profiles in the atmospheric surface layer: a re-evaluation. *Boundary-Layer Meteorology*, **42**, 55-78.

Holt, T. and J. Pullen, 2007: Urban Canopy Modeling of the New York City Metropolitan Area: A Comparison and Validation of Single- and Multilayer Parameterizations. *Monthly Weather Review*, **135**, 1906-1930.

Johnson, G. T., Oke, T. R., Lyons, T. J., Steyn, D. G., Watson, I. D., and Voogt, J. A., 1991: Simulation of Surface Urban Heat Islands under Ideal Conditions at Night, Part 1: Theory and Tests Against Field Data, *Boundary-Layer Meteorology*, **56**, 275–294.

Kaimal, J. C., and Wyngaard, J.C., 1990: The Kansas and Minnesota experiments. *Boundary-Layer Meteorology*, **50**, 31-47.

Kaimal and Finnigan, 1994: Boundary Layer Flows: Their Structure and Measurements. *New York, Oxford University Press.* 289 pp.

Kanda M., Takayanagi Y., Yokoyama H. and Moriwaki R., 1997: Field observation of the heat balance in an urban area. *J Japan Soc Hydrol Water Resour* , **10**, 329–336 (in Japanese)

Kanda, M., R. Moriwaki, M. Roth and T. Oke, 2002: Area-averaged sensible heat flux and a new method to determine zero-plane displacement length over an urban surface using scintillometry. *Boundary-Layer Meteorology*, **105**, 177-193.

Kanda, M., R. Moriwaki, and F. Kasamatsu, 2006: Spatial variability of both turbulent fluxes and temperature profiles in an urban roughness layer. *Boundary-Layer Meteorology*, **121**, 339-350.

Klein, P., and J. V. Clark, 2007: Flow variability in a north American downtown street canyon. *Journal of Applied Meteorology and Climatology*, **46**, 851-877.

Kleissl, J., J. Gomez, S. H. Hong, J. M. H. Hendrickx, T. Rahn and W. L. Defoor, 2008: Large Aperture Scintillometer Intercomparison. *Boundary-Layer Meteorology*, **128**, 133-150.

Kusaka, H., H. Kondo, Y. Kikegawa, and F. Kimura, 2001: A simple single-layer urban canopy model for atmospheric models: Comparison with multi-layer and SLAB models. *Boundary-Layer Meteorology*, **101**, 329–358.

Kusaka H, Kimura F. 2004. Coupling a single-layer urban canopy model with a simple atmospheric model: impact on urban heat island simulation for an idealized case. Journal of the Meteorological Society of Japan 82: 67–80.

Lacser, A. and Otte, T. L.: 2002, 'Implementation of an Urban Canopy Parameterization in MM5', *Preprints, in Fourth Symposium on Urban Environment, American Meteorological Society, Norfolk, VA*, pp. 153–154.

Lagouarde J. -P., M. Irvine, J. -M. Bonnefond, C. S. B. Grimmond and N. Long, et al., 2006: Monitoring the Sensible Heat Flux over Urban Areas using Large Aperture Scintillometry: Case Study of Marseille City During the Escompte Experiment. *Boundary-Layer Meteorology*, **118**, 449-476.

Lee, X., W. Massman and B. Law, 2004: Handbook of Micrometeorology: a guide for surface flux measurement and analysis. *Kluwer Academic Publishers, Dordrecht, The Netherlands*, 250 pp.

Lee, S.-H. and S.-U. Park, 2008: A Vegetated Urban Canopy Model for Meteorological and Environmental Modelling. *Boundary-Layer Meteorology*, **126**, 73-102.

Lemonsu, A., Grimmond, C. S. B. and Masson, V., 2004: Modeling the Surface Energy Balance of an old Mediterranean city core. *Journal of Applied Meteorology*, **43**, 312-327.

Lemonsu, A., G. Pigeon, V. Masson and C. Moppert, 2006: Sea-town interactions over Marseille: 3D urban boundary layer and thermodynamic fields near the surface. *Theor. Appl. Climatol.*, **84**, 171–178.

Liu Y, Chen F, Warner T, Basara J., 2006: Verification of a mesoscale data-assimilation and forecasting system for the Oklahoma city area during the Joint Urban 2003 Field Project. *Journal of Applied Meteorology*, **45**, 912–929.

Longley, I. D., M. W. Gallagher, J. R. Dorsey, M. Flynn, and J. F. Barlow, 2004: Short-term measurements of airflow and turbulence in two street canyons in Manchester. *Atmospheric Environment*, **38**, 69-79.

Louka, P., S. E. Belcher, and R. G. Harrison, 1998: Modified street canyon flow. *Journal of Wind Engineering and Industrial Aerodynamics*, **74-6**, 485-493.

Louka, P., S. E. Belcher, and R. G. Harrison, 2000: Coupling between air flow in streets and the well-developed boundary layer aloft. *Atmospheric Environment*, **34**, 2613-2621.

Martilli, A., A. Clappier and M. Rotach, 2002: An urban surface exchange parameterisation for mesoscale models. *Boundary-Layer Meteorology*. **104**. 261-304.

Mascart, P., Noilhan, J., and Giordani, H., 1995: A Modified Parameterization of Flux-Profile Relationship in the Surface Layer Using Different Roughness Length Values for Heat and Momentum, *Boundary-Layer Meteorology*, **72**, 331–344.

Masson, V., 2000: A physically-based scheme for the urban energy budget in atmospheric models. *Boundary-Layer Meteorology*, **98**, 357–397.

McAloon, C. M., 2001: An examination of sensible heat flux using the gradient-profile technique at ten Oklahoma MESONET sites. *Master Thesis submitted to the School of Meteorology, University of Oklahoma*, 91 pp.

McPherson, R. A., C. A. Fiebroch, K. C. Crawfors, R. L. Elliott, J. R. Kilby, D. L. Grimsley, J. E. Martinez, J. B. Basara, B. G. Illston, D. A. Morris, K. A. Kloesel, S. J. Stadler, A. D. Melvin, A. J. Sutherland, H. Shrivastava, J. D. Carlson, J. M. Wolfinbarger, J. P. Bostic and D. B. Demko: Statewide Monitoring of the Mesoscale Engionment: A Technical Update on the Oklahoma Mesonet. *Journal of Atmospheric and Oceanic Technology*, **24**, 301-321.

Meijninger W. M. L., O. K. Hartogensis, W. Kohsiek, J. C. B. Hoedges, R. M. Suurbier and H. A. R. De Bruin, 2002: Determination of area-averaged sensible heat fluxes with a large aperture scintillometer over a heterogeneous surface – Flevoland Field. *Boundary Layer Meteorology*, **105**, 37-62.

Meijninger W. M. L., F. Beyrich, A. Lüdi, W. Koshiek and H. A. R. De Bruin, 2006: Scintillometer-based turbulent fluxes of sensible and latent heat over a heterogeneous land surface - A contribution to Litfass-2003. *Boundary-Layer Meteorology*, **121**, 89-110.

Menut, L.: 1997, Etude expérimentale et théorique de la couche limite Atmosphérique en agglomération Parisienne (Experimental and Theoretical Study of the ABL in Paris Area), *Ph.D. Thesis, University Pierre et Marie Curie, Paris, France*, 200 pp.

Mestayer, P., Durand, P., Augustin, P., Bastin, S., Bonnefond, J-M, Bénech, B., Campistron, B., Coppalle, A., Delbarre, H., Dousset, B., Drobinski, P., Druilhet, A., Fréjafon, E., Grimmond, S., Groleau, D., Irvine, M., Kergomard, C., Kermadi, S., Lagouarde, J-P, Lemonsu, A., Lohou, F., Long, N., Masson, V., Moppert, C., Noilhan, J., Offerle, B., Oke, T., Pigeon, G., Puygrenier, V., Roberts, S., Rosant J-M, Saïd, F., Salmond, J., Talbaut, M., and Voogt, J., 2005: The Urban Boundary Layer Field Experiment over Marseille UBL/CLU-ESCOMPTE: Experimental Set-up and First Results. *Boundary Layer Meteorology*, **114**, 315-365.

Mills, G. M., 1993: Simulation of the Energy Budget of an Urban Canyon – 1. Model Structure and Sensitivity Test, *Atmospheric Environment*, **27B**, 157–170.

Monin, A. S. and A. M. Obukhov, 1954: Basic laws of turbulence mixing in the atmosphere near the ground, *Tr.-Akad. Nauk. S. S. S. R. Geophiz. Inst.*, No. 24.

Monin A. S., Yaglom, A. M., 1971: Statistical Fluid Mechanics, Vol.1. *MIT Press, Cambridge, USA*, 769 pp.

Moriwaki, R., and M. Kanda, 2006: Flux-gradient profiles for momentum and heat over an urban surface. *Theoretical and Applied Climatology*, **84**, 127-135.

Novikov, E.A., 1961: The energy spectrum of incompressible turbulent flow. *Dokl. Akad. Nauk. SSSR*, **139**, 331-333.

Nunez, M. and Oke, T. R.: 1977, 'The Energy Balance of an Urban Canyon', J. Appl.Meteorol. 16, 11–19.

Offerle, B., C. S. B. Grimmond and T. R. Oke, 2003: Parameterization of Net All-Wave Radiation for Urban Areas. *Journal of Applied Meteorology*, **42**, 1157-1173

Offerle, B., I. Eliasson, C. S. B. Grimmond, and B. Holmer, 2007: Surface heating in relation to air temperature, wind and turbulence in an urban street canyon. *Boundary-Layer Meteorology*, **122**, 273-292.

Oikawa, S., and Y. Meng, 1995: Turbulence Characteristics and Organized Motion in a Suburban Roughness Sublayer. *Boundary-Layer Meteorology*, **74**, 289-312.

Oke, T. R., 1976: The distinction between canopy and boundary-layer urban heat islands. *Atmosphere*, **14**, 399-410.

Oke, T. R., 1987: Boundary-Layer Climates, *Routledge, 2nd edition, Methuen, New York*, 435 pp.

Okamoto, S., Nakaso, K., and Kawai, I., 1993: Effect of Rows of Two-Dimensional Square Ribs of Flow Property along Plane Wall, *JSME Int. J. Series B. – Fluid Therm. Engin.* **36**, 121–129.

Otte, T. L., A. Lacser, S. Dupont and J. K. S. Ching, 2004: Implementation of an Urban Canopy Parameterization in a Mesoscale Meteorological Model. *Journal of Applied Meteorology*, **43**, 1648-1665.

Panofsky H.A., and Dutton, J.A., 1984: Atmospheric Turbulence: Models and Methods for Engineering Applications, *Wiley, New York*.

Petersen, R. L.: 1997, 'A Wind Tunnel Evaluation of Methods for Estimating Surface Roughness Length at Industrial Facilities', *Atmospheric Environment*, **31**, 45–57.

Porson, A., and I. Harman, 2009: How Many Facets are Needed to Represent the Surface Energy Balance of an Urban Area? *Boundary-Layer Meteorology*, **132**, 107-128.

Randow, C. von; Kruijt, B.; Holtslag, B., 2006: Exploring eddy covariance and scintillometer measurements in the Amazon rain forest In: Integrated land ecosystem-atmosphere processes study. *Proceedings of the 1st iLEAPS science conference, Helsinki (Finland), January 21-26, 2006. - Helsinki (Finland) : Yliopistopaino*, - p. 290 - 291.

Raupach, M. R., 1979: Anomalies in flux-gradient relationships over forest. *Boundary Layer Meteorology*, **16**, 467-486.

Raupach, M. R. and Legg, B. J., 1984: The use and limitations of flux-gradient relationships in micro-meteorology. *Agric. Water Management*, **8**, 119-131.

R. M. Young Company, 2011: Ultrasonic anemometer model 81000. *Available online at http://www.campbellsci.ca/Catalogue/81000_Man.pdf*. 12 pps. Web. August.31.2011.

Rotach, M. W., 1993a: Turbulence Close to a Rough Urban Surface .1. Reynolds Stress. *Boundary-Layer Meteorology*, **65**, 1-28.

Rotach, M. W., 1993b: Turbulence Close to a Rough Urban Surface .2. Variances and Gradients. *Boundary-Layer Meteorology*, **66**, 75-92.

Rotach, M.W., 1995: Profiles of turbulence statistics in and above an urban street canyon. *Atmospheric Environment*, **29**, 1473-1486.

Rotach, M.W., 1999: On the influence of the urban roughness sublayer on turbulence and dispersion. *Atmospheric Environment*, **33**, 4001-4008.

Rotach, M.W., R. Vogt, C. Bernhofer, E. Batchvarova, A. Christen, A. Clappier, B. Feddersen, S.-E. Gryning, G. Martucci, H. Mayer, V. Mitev, T. R. Oke, E. Parlow, H. Richner, M. Roth, Y.-A. Roulet, D. Ruffieus, J. A. Salmond, M. Schatzmann and J. A. Voogt, 2005: BUBBLE - an Urban Boundary Layer Meteorology Project. *Theor. Appl. Climatol.*, **81**, 231-261.

Roth, M. and Oke, T.R., 1995: Relative efficiencies of turbulent transfer of heat, mass and momentum over a patchy urban surface. *Journal of Atmospheric Sciences*, **52 (11)**, 1863-1874.

Roth, M., 2000: Review of atmospheric turbulence over cities, *Q. J. R. Meteorological Society*, **126**, pp. 941-990.

Roth, M., and T. R. Oke, 1993a: Turbulent Transfer Relationships over an Urban Surface .1. Spectral Characteristics. *Quarterly Journal of the Royal Meteorological Society*, **119**, 1071-1104.

Roth, M. and T. R. Oke, 1993b: Turbulent Transfer Relationships over an Urban Surface .2. Integral Statistics, *Quarterly Journal of the Royal Meteorological Society*, **119**, 1105-1120.

Roth, M., J. A. Salmond, and A. N. V. Satyanarayana, 2006: Methodological considerations regarding the measurement of turbulent fluxes in the urban roughness sublayer: The role of scintillometery. *Boundary-Layer Meteorology*, **121**, 351-375.

Roulet, Y.-A., A. Martilli, M. Rotach and A. Clappier, 2005: Validation of an Urban Surface Exchange Parameterization for Mesoscale Models—1D Case in a Street Canyon. *Journal of Applied Meteorology*, **44**, 1484-1498.

Salmond, J. A., M. Roth, T. R. Oke, A. N. V. Satyanarayana, and A. Christen, 2003: Methodological considerations regarding the use of scintillometers in the urban roughness sub-layer. *EGS - AGU - EUG Joint Assembly, Abstracts from the meeting held in Nice, France, 6 - 11 April 2003*.

Schmid, H. P., 1994: Source areas for scalars and scalar fluxes. *Boundary-Layer Meteorology*, **67**, 293–318.

Schmid, H. P., 2002: Footprint modeling for vegetation atmosphere exchange studies: a review and perspective. *Agric Forest Meteorol*ogy, **113**, 159–183

Schmid, H. P., Oke, T. R., 1990: A model to estimate the source area contributing to turbulent exchange in the surfacelayer over Patchy Terrain. *Quart J Roy Meteor Soc*, **116**, 965–988

SCINTEC AG, 2006: Scintec Surface Layer Scintillometer User Manual. *Tübingen, Germany*, 100 pp.

Seaman, N. L., Ludwig, F. F., Donall, E. G.,Warner, T. T., and Bhumralkar, C.M.: 1989, 'Numerical Studies of Urban Planetary Boundary-Layer Structure under Realistic Synoptic Conditions', *J. Appl. Meteorology*, **28**, 760–781.

Shafran, P. C., N. L. Seaman, and G. A. Gayno, 2000: Evaluation of numerical predictions of boundary layer structure during the Lake Michigan Ozone Study. *J. Appl. Meteor.*, **39**, 412–426.

Sorbjan, Z, 1989: Structure of the atmospheric boundary-layer. *Prentice-Hall, New Jersey*, 317 pp.

Stensrud, D. J., 2007: Parameterization Schemes: Keys to Understanding Numerical Weather Prediction Models. *Cambridge University Press*, 488 pp.

Stull, R.B., 1988: An introduction to Boundary Layer Meteorology, *Kluwer Academic Publishers*, London. 666pp.

Stull, R.B., 2000: Meteorology for scientist and engineers, *Brooks/Cole. Belmont, California*, 502 pp.

Taha, H., 1999: Modifying a Mesoscale Meteorological model to Better Incorporate Urban Heat Storage: A Bulk Parameterization Approach. *Journal of Applied Meteorology*, **38**, 466-473.

Taha H, Bornstein R. 1999. Urbanization of meteorological models: implications on simulated heat islands and air quality. International Congress of Biometeorology and International Conference on Urban Climatology (ICB-ICUC) Conference, Sydney, Australia, 8–12 November 1999.

Taha H. 2008a. Urban surface modification as a potential ozone air-quality improvement strategy in California: a mesoscale modeling study. Boundary-Layer Meteorology 127(2): 219–239, DOI:10.1007/s10546-007-9259-5.

Taha H. 2008b. Meso-urban meteorological and photochemical modeling of heat island mitigation. Atmospheric Environment 42: 8795–8809, DOI:10.1016/j.atmosenv.2008.06.036.

Tatarskii, V. I., 1961: Wave Propagation in Random Media, *Dover Publications, New York*.

Tatarskii, V. I., 1971: The effects of the turbulent atmosphere on wave propagation. *Israel Program for Scientific Translations, Jerusalem, NTIS TT 68-50464*, 472 pp.

Tennekes, H., 1973: The logarithmic wind profile. *Journal of Atmospheric Sciences*, **30**, 234-238.

Thiermann, V. and Azoulay, E., 1989: Modeling the structure constant and inner scale of refractive index fluctuations – an experimental investigation. *Proc. SPIE*, **1115**, 124-135.

Thiermann, V. and H. Grassl, 1992: The measurement of turbulent surface-layer fluxes by use of bichromatic scintillation. *Boundary-Layer Meteorology*, **28**, 367-389.

Tillman, J. E., 1972: The indirect determination of stability, heat and momentum fluxes in the atmospheric boundary layer from simple scalar variables during dry unstable conditions. *Journal of Applied Meteorology*, **11**, 783-792.

United Nations, 2009: Percentage of Population Residing in Urban Areas by Major Ares, Region and Country, 1950-2050. *http://esa.un.org/unpd/wup/index.htm*. Web. August.29.2011.

Uno, I., Ueda, H., and Wakamatsu, S., 1989: Numerical Modelling of the Nocturnal Urban Boundary Layer, *Boundary-Layer Meteorology*, **49**, 77–98.

Van de Wiel, B.J.H., Moene A.F., Hartogensis, O.K., De Bruin, H.A.R., and Holtslag, A.M., 2003: Intermittent turbulence in the stable boundary layer over land. Part III: a classification for observations during CASES-99. *Journal of Atmospheric Sciences*, **60**, 2509-2522.

Wallace and Hobbs, 2006: Atmospheric Science, an Introductory Survey. *Elsevier, second edition. Oxford, UK*. 483 pps.

Wang, Ochs, G. R., and Clifford, S. F., 1978: A saturation resistant optical scintillometer to measure C_n^2, *Journal of the Optical Society of America*, **68**, 334-338.

Weiss, A., 2002: Determination of thermal stratification and turbulence of the atmospheric surface layer over various types of terrain by optical scintillometery. *PhD Dissertation submitted to the Swiss Federal Institute of Technology, Zurich*, 151 pp.

Wesely, M. L., 1976: The combined effect of temperature and humidity fluctuations on refractive index. *Journal of Applied Meteorology*, **15**, 43-39.

Wieringa, J., 1993: Representative Roughness Parameters for Homogeneous Terrain, *Boundary-Layer Meteorology*, **63**, 323–363.

Wilczak J. M., S. P. Oncley and S. A. Stage, 2001: Sonic anemometer tilt correction algorithms. *Boundary-Layer Meteorology*, **99**, 127-150.

Wyngaard, J.C., 1973: On Surface-Layer Turbulence, *in D. A. Haugen (ed.). Workshop on Micrometeorology, American Meteorological Society, Boston*, pp. 101-149.

Wyngaard, J.C., 1990: Scalar fluxes in the planetary boundary layer - theory, modeling and measurement. *Boundary-Layer Meteorology*, **50**, pp. 49-75.

Wyngaard, J.C. and Coté, O.R., 1971: The budgets of turbulent kinetic energy and temperature variance in the atmospheric surface layer. *Journal of the Atmospheric Sciences*, **28**, 190-201.

Wyngaard, J.C., Coté, O.R.., and Izumi, Y, 1971: Local free convection, similarity and the budgets of shear stress. *Journal of Atmospheric Sciences*, **28**, 1171-1182.

APPENDIX 1

Dissipation rates of TKE as means for SLS SHFX evaluation

Dissipation rates calculated from sonic anemometer data were explored as a means to evaluate SLS SHFX. The connection is through the non-dimensional dissipation rate function from the SLS algorithm φ_ε, which is computed using an empirical approximation. Unfortunately, the impact of computing a new empirical approximation for φ_ε and applying it to SLS data was not as significant as expected. This lead to the consideration of different approaches described in Chapter 4. It was considered useful, however, to present the methodology in this appendix.

The dissipation rate of turbulent kinetic energy ε describes the flow of energy towards smaller scales within the inertial sub-range (ISR) of energy spectra, where isotropy and a lack of sources and sinks of energy prevail (Kaiser and Fedorovich, 1998). As a result, one of the most reliable methods used to estimate ε is by considering the slope in the ISR of high-temporal-resolution velocity spectra.

Dissipation rates play an important role in several areas within the field of boundary-layer meteorology and turbulence. In bichromatic scintillometry, ε are essential for the calculation of turbulent fluxes from scintillations. In brief, ε are obtained from measurements of l_0 via expression (3.12); they are then combined with C_T^2 and MOS empirical functions of dimensionless height $\varphi_\varepsilon(\zeta)$ and $\varphi_{C_T^2}(\zeta)$ to determine surface layer scales via iterations; finally the latter are used to determine turbulent fluxes of heat and momentum. Since the largest source of uncertainty arises from $\varphi_\varepsilon(\zeta)$ and $\varphi_{C_T^2}(\zeta)$, it is appropriate and recommended to ensure that the empirical functions used by the scintillometer are suitable for the sampling environment. With this goal in mind, $\varphi_\varepsilon(\zeta)$

were computed using sonic anemometer observations collected during ILREUM sub-urban campaigns. These were then compared against $\varphi_\varepsilon(\zeta)$ used in the scintillometer algorithm and against some alternate approximations described in the literature.

The methodology considered to determine $\varphi_\varepsilon(\zeta)$ for MOS evaluation was based on procedures described in Kaimal and Finnigan (1994), Kaiser and Fedorovich (1998), Roth (2000) and Roth and Salmond (2006). Comparisons were established between scintillometer dissipation rates and those computed from sonic anemometer measurements made near the center of the path. In an attempt to assure the validity of MOS, only data from wind directions representative of a homogeneous fetch (140° to 210°) were considered. Steps considered include determination of energy spectra from velocity perturbation timeseries; identification of the inertial sub-range; calculation of normalized dissipation rates; quality-assurance to ignore odd-looking spectra; comparisons against empirical fits used in the scintillometer algorithm as well as others described in the literature and, finally, estimation of appropriate empirical fits for ILREUM data.

a. Determination of energy spectra.

Energy spectra can be calculated from velocity perturbation timeseries. A commonly accepted technique is to work in the natural coordinate system, which implies rotation of velocity data so that the mean flow is aligned with the zonal component of the Cartesian coordinate system. Once zonal velocity perturbations *U'(t)* have been calculated, energy spectra can be computed by applying the Fast Fourier Transform FFT (Kaiser and Fedorovich, 1998 and Kaimal and Finnigan, 1994). The FFT allows to

express finite time series as a function of frequencies *f* instead of time *t*. It can be defined as:

$$FFT[\varphi(n\Delta t)] = \Delta t \sum_{n=0}^{N_{max}-1} \varphi(n\Delta t) exp[-2\pi i(m\Delta f)(n\Delta t)]$$
$$= \Delta t \sum_{n=0}^{N_{max}-1} \varphi(n\Delta t) exp[-2\pi i n m / N_{max}] \quad \text{(A1.1)}$$

where $\varphi(n\Delta t)$ is a finite timeseries, Δt is the sampling interval in seconds, Δf is the frequency interval in Hz and N_{max} is the total number of observations. Indices n and m represent time and frequency space respectively. When calculated, the result of the FFT can be converted into energy $S_u(f)$ by calculating the square of the absolute value of the real part of the spectrum (the first half); and after appropriate scaling as follows:

$$S_u(f) = \frac{2}{N_{max}\Delta t} |FFT(\varphi(n\Delta t))_{real}|^2 \quad \text{(A1.2)}$$

The corresponding range of frequencies can be then calculated via:

$$f_n = \frac{n}{N_{max}\Delta t} \quad \text{(A1.3)}$$

(Kaimal and Finnigan, 1994; Kaiser and Fedorovich, 1998). This method was applied to ILREUM sub-urban datasets. The data was organized into 15-minute-long timeseries sampled at a frequency of 10 Hz (Δt=0.1 s). This lead to N_{max}=9000.

b. Non-dimensional dissipation from spectra.

According to Kolmogorov (1941), the following expression is valid for the ISR of energy spectra expressed as a function of wave number *k*:

$$S_u(k) = \alpha\, \varepsilon^{2/3}\, k^{-5/3} \quad \text{(A1.4)}$$

where α~0.52 is a constant of proportionality found to fall between 0.4 and 0.6; $S_u(k)$ is energy density as a function of k and ε is the dissipation rate of TKE. Once combined with the MOS expression for non-dimensional dissipation φ_ε:

$$\varphi_\varepsilon = \kappa z \varepsilon / u_*^3 \tag{A1.5}$$

one can obtain an expression for φ_ε as a function of energy density and wave number:

$$\varphi_\varepsilon = \frac{\kappa z}{u_*^3} \left[\frac{S_u(k)}{\alpha}\right]^{3/2} k^{5/2} \tag{A1.6}$$

A relationship between wave number and frequency spectra can be established by considering that Taylor's hypothesis is valid. This assumption allows to relate wave number k and frequency f using the mean wind speed $\overline{U}$ as follows:

$$k = \frac{2\pi}{\lambda} = \frac{2\pi f}{\overline{U}} \tag{A1.7}$$

and:

$$S_u(k) = \frac{\overline{U}}{2\pi} S_u(f) \tag{A1.8}$$

The combination of expressions (A1.6), (A1.7) and (A1.8) yields the following expression for φ_ε:

$$\varphi_\varepsilon = \frac{2\pi\kappa z}{U u_*^3} f^{5/2} \left[\frac{f S_u(f)}{\alpha}\right]^{3/2} \tag{A1.9}$$

which allows to determine non-dimensional dissipation directly from frequency spectra. Expression (A1.9) is valid only within the ISR of velocity spectra, under conditions where Taylor's Hypothesis applies. A representative value of φ_ε can be obtained by averaging all calculated values that fall within the ISR, whose limits need to be carefully defined.

c. Inertial sub-range limits.

Defining ISR location in energy spectra can be a non-trivial procedure. In theory, slope in the ISR should approach -2/3 once both frequency and energy density have been normalized into non-dimensional quantities. In reality, however, this is not strictly the case. Slopes can often be larger than -2/3 (Roth et al., 2006) and in some cases spectra shapes can deviate significantly from the expected. Factors that cause these deviations include instrument characteristics, sampling frequency, sampling height and characteristics of the sampling environment itself.

A common practice to define ISR location consists of finding a range of frequencies that leads to: (i) φ_ε approaching 1 near neutrality (i.e. in theory, $\varphi_\varepsilon[0] = 1$) and (ii) spectra shapes that approach those of theoretical spectra. ISR position varies upon datasets and must be determined accordingly (Roth et al. 2006).

The first necessary step is spectra normalization. The method applied to ILREUM spectra, one commonly described in the literature, uses friction velocity u_* and non-dimensional dissipation φ_ε as follows:

$$S'_u(f) = fS_u(f)/u_*^2\varphi_\varepsilon^{2/3} \tag{A1.10}$$

where φ_ε is calculated from the ISR of the spectra itself. Frequency *f* is also normalized into non-dimensional frequency *F* via:

$$F(f) = fz/\overline{U} \tag{A1.11}$$

where $\overline{U}$ is the mean wind speed. This method of is also commonly applied to v' and w' spectra, which were also explored a means to verify that calculations were correct.

One limitation of this method is that values of φ_ε are unknown before normalization. They can only be calculated once the ISR *F* range has been defined. This requires thorough exploration of spectra and associated φ_ε under different definitions of *F* ranges. This analysis was applied to ILREUM data and the results are presented in Figure A1.9. Spectra (left) and corresponding $\varphi_\varepsilon(\zeta)$ (right) are shown for selected *F* ranges. Thick black curves are references calculated from spectra collected during the Kansas experiments (Kaimal and Finnigan, 1994) for stabilities that range between $-2.0 < \zeta < +2.0$. Trials using different ranges are indicated using different colors. Yellow and orange are used for higher frequencies and purples and blues for lower frequencies. Figure A1.9 demonstrates that ISR *F* range definition does affect calculated values of φ_ε in addition to the shape and magnitude of normalized spectra. The results were also compared against ranges suggested by other studies. These ranges, together with the results from this study, are summarized in Table A1.1.

Both Figure A1.9 and Table A1.1 show that for ILREUM data the best results were attained using ranges that fell within the lower end of those described in the literature. Spectra and associated $\varphi_\varepsilon(\zeta)$ plotted in blue and purple produced better results than those plotted using yellow and orange. Differences upon limit selection are caused by slight changes in spectra slope and magnitude that occur under different frequency ranges. Slopes tend to decrease towards higher frequencies, which produce values of $\varphi_\varepsilon(\zeta)$ that are too large. Spectra and associated ISR *F* ranges also differ amongst instrument platforms. The RM-Young sonic anemometers seemed to perform better than the CSAT sonic anemometers, based only upon spectra shape and magnitude. ISR limit definition appears more critical in the latter, where the behavior of spectra slope as a function of frequency deviates more from linearity.

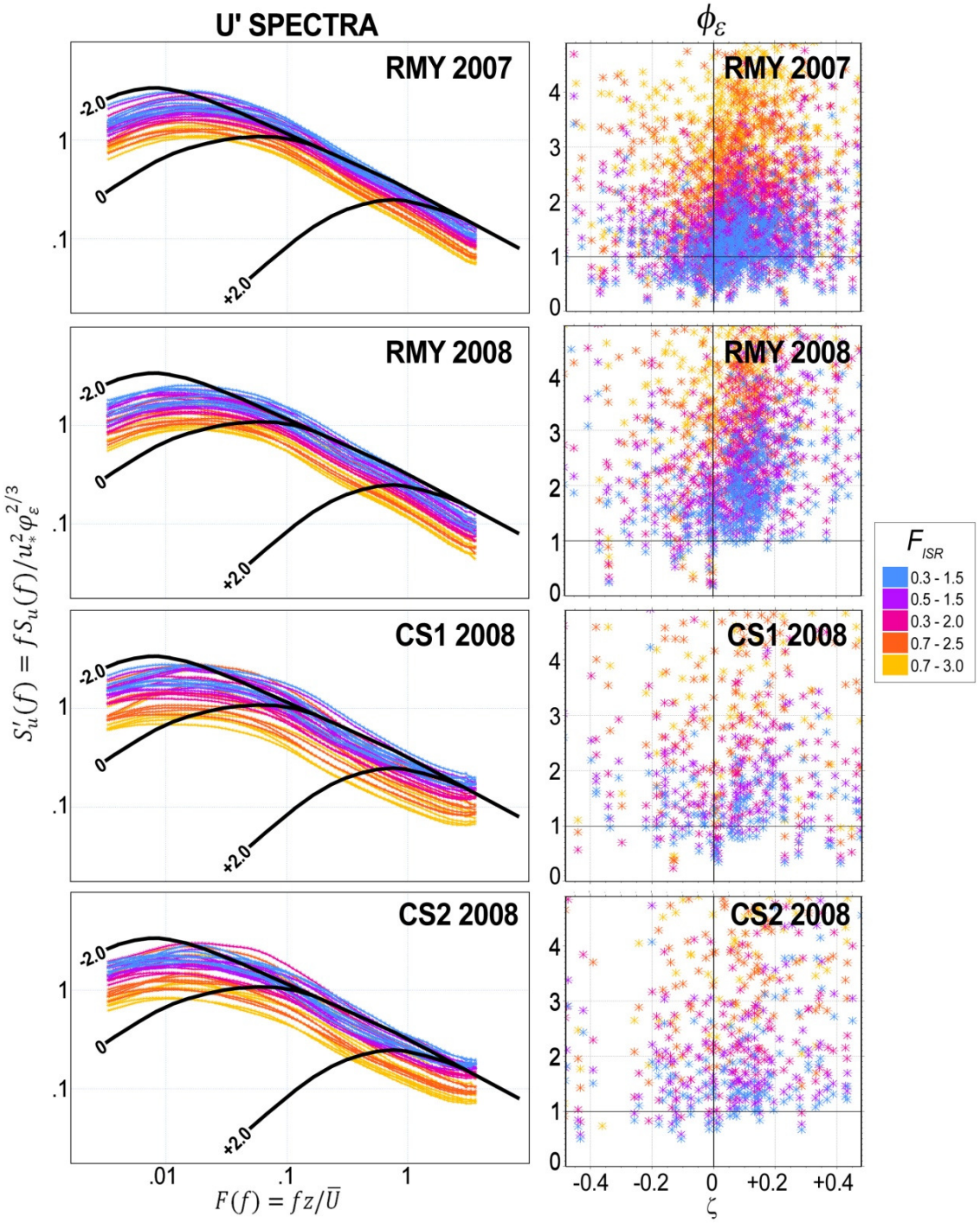

Figure A1.1. Normalized spectra (left) and non-dimensional dissipation rates (right) calculated using different selected ISR definitions.

Table A1.1. Summary of inertial sub-range statistics for suburban studies based on Roth et al. (2006).

Study	z/z_H	Slope	F	Comments
Rotach (1991)	1.55	> -2/3	3	Urban slope for *u*, *v*, and *w*
	1.27	> -2/3	3	
	0.91	> -2/3	3	
	0.71	> -2/3	3.5, 11	
Roth and Oke (1993)	2.62	-2/3	2.5-5	Suburban (slope for *u*,*v*,*w*)
Christen et al. (2004)	2.17	> -2/3	~0.9-9	Urban (slope for *u*)
	1.23	> -2/3	~0.5-5	
	1.01	> -2/3	~0.5-5	
	0.77	> -2/3	~0.6-6	
Roth et al. (2006)	1.32	-2/3	3-6	Urban (slope for *w*)
	1.01	-2/3	4-10	
ILREUM (Present study)		>-2/3	0.3-1.5	Sub-urban, RMY 2007 (*u*)
		>-2/3	0.1-1.2	Sub-urban, RMY 2008 (*u*)
		>-2/3	0.1-1.4	Sub-urban, CS1 2008 (*u*)
		>-2/3	0.6-1.5	Sub-urban, CS2 2008 (*u*)

z - sensor height, z_H - average height of buildings, F - non-dimensional frequency, f - natural frequency

The most remarkable discrepancies with respect to other studies arise in the high end of frequencies. Other studies we able to consider larger frequencies / smaller scales. ILREUM measurements, especially those made with the CSAT sonic anemometers, struggled resolving frequencies larger than F~4. The sampling frequency of 10 Hz was not large enough to capture energy at large values of F. Furthermore, smaller scales are also generally affected by aliasing.

d. Quality assurance and spectral stability dependence.

Before looking into the calculated values for φ_ε, it was appropriate to verify that each energy spectrum looked reasonable in comparison against standard spectra described in the literature. The quality assurance procedure applied to energy spectra was to remove those spectra that showed values out of given bounds. Spectra out of the

following bounds were removed: $F < 0.005$ and $S'_u(f) > 0.25$; $F > 0.009$ and $S'_u(f) > 0.04$; $0.009 > F > 0.105$ and $S'_u(f) < 0.02$; and $2.2 < F < 3.5$ and $S'_u(f) < 0.007$ or $S'_u(f) > 0.025$. Bounds selection was based on careful screening of all raw ILREUM spectra and could vary if another dataset is considered.

Once the final spectra were selected, a final quality checkpoint was to explore their dependence on stability and compare them against theoretical spectra from data from the Kansas Experiments described in Kaimal and Finnigan (1994). Spectra for v' and w' were also plotted as a means to revise that the calculations were correct. These comparisons are summarized in Figure A1.2. Thin colored curves represent all selected ILREUM spectra stratified by stability ranges. Reds and yellows are used for unstable conditions whereas blues are used for stable conditions. Thick black curves represent findings from the Kansas experiment.

The results in Figure A1.2. indicate that ILREUM spectra generally fall within the expected range. Spectra tended to collapse as expected within the inertial sub-range. Shape dependence on stability was also evident but not as clearly as expected. Spectra calculated using v' and w' do show a more clear tendency for a shift of the energy peak towards larger frequencies as stability increases. This trend, yet existing, is much less clear in u' spectra. Overall, spectra look reasonable and were consider suitable for the calculation of $\varphi_\varepsilon(\zeta)$.

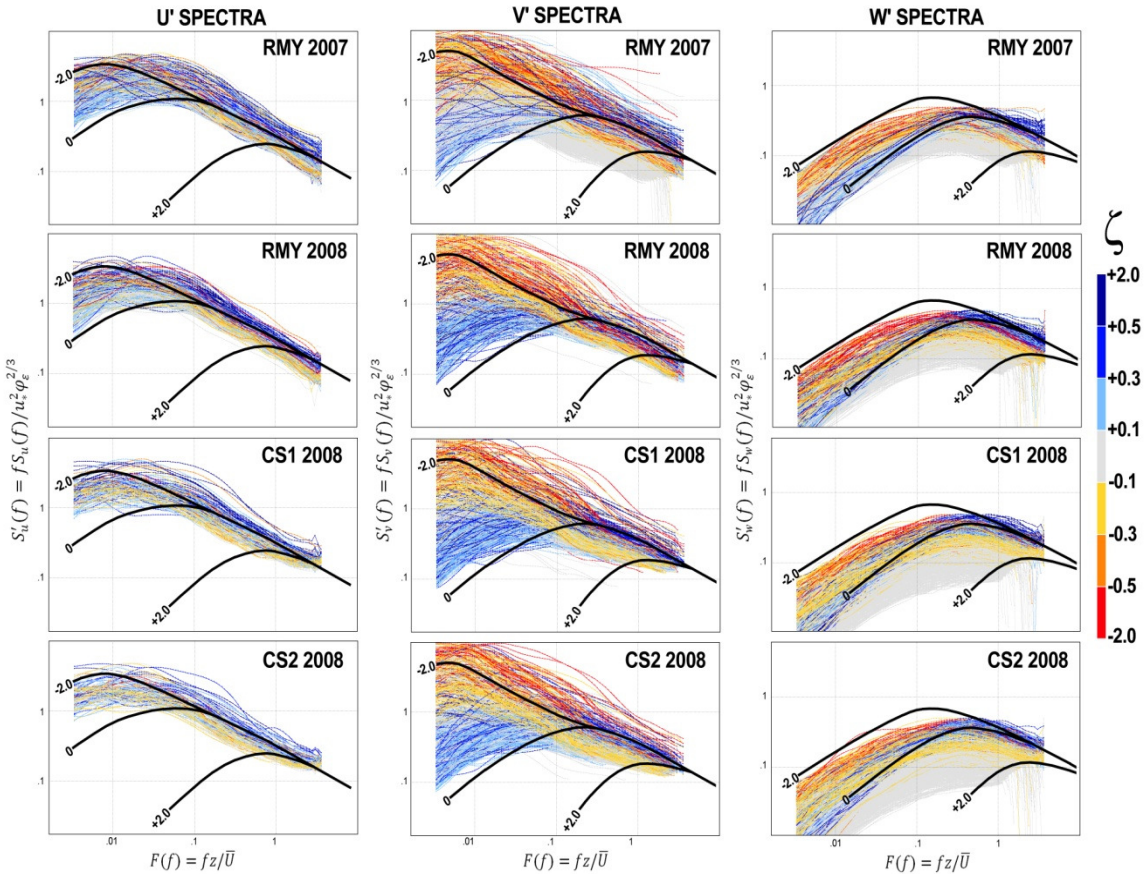

Figure A1.2. Spectra for u', v' and w' of the four sonic anemometers operated near path center. Spectra are stratified for different stability categories (color scale). Theoretical spectra for different stabilities (Kaimal and Finnigan, 1994) are provided with thick black curves.

e. Empirical fits.

The values of $\varphi_\varepsilon(\zeta)$ calculated from spectra were plotted as a function of stability and compared against different empirical fits described in the literature in Figure A1.3.

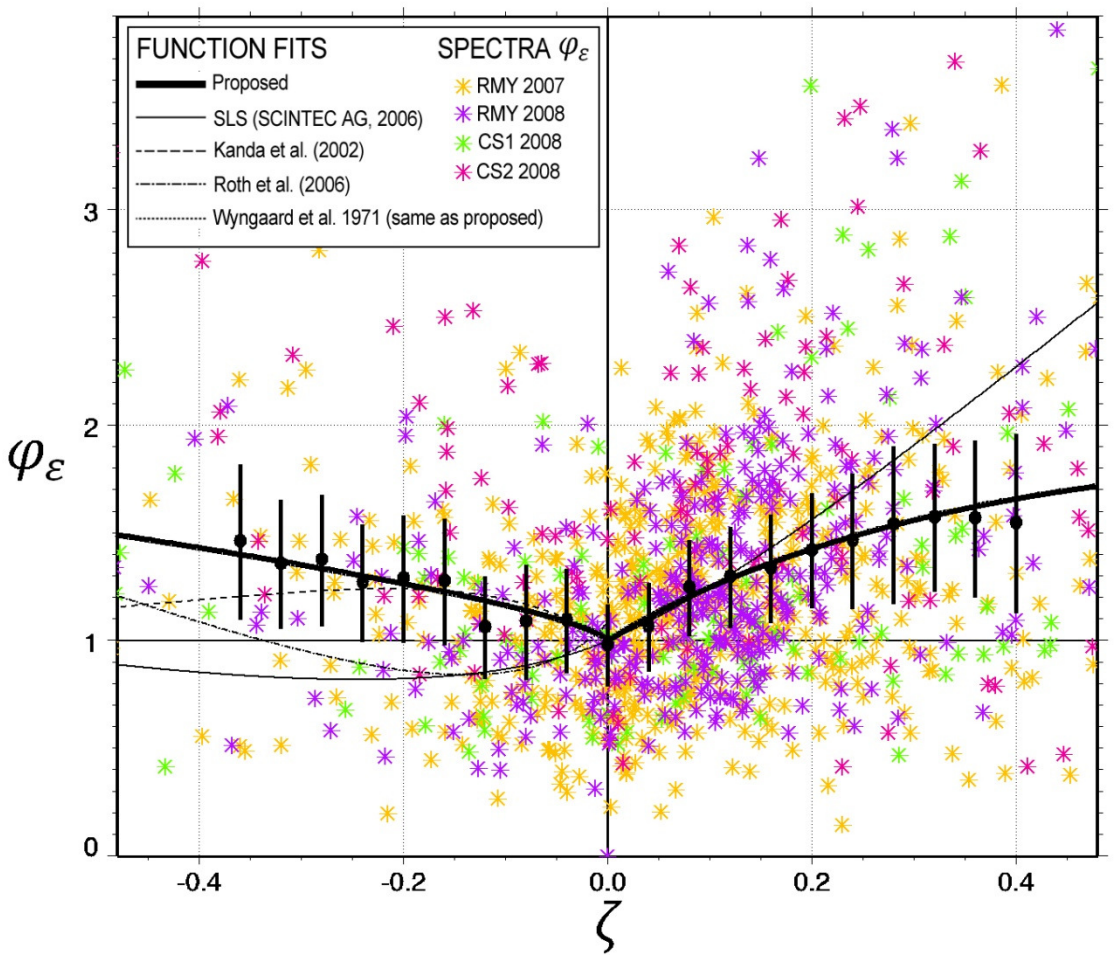

Figure A1.3. Distribution of $\varphi_\varepsilon(\zeta)$ from spectra compared against various proposed empirical fits.

Values of $\varphi_\varepsilon(\zeta)$ derived from ILREUM data are displayed using asterisks. Different colors represent different instrumentation platforms, as indicated in the figure. ILREUM data was also organized in bins which are plotted using solid circles and vertical lines that represent standard deviation. Empirical fits described in the literature are plotted with thin lines: solid for the functions used in the scintillometer algorithm after (SCINTEC AG, 2006); dashed for those presented by Kanda et al. (2002) and by Roth et al. (2006) both from urban areas and dotted for the function proposed by Wyngaard et al. (1971). The fits proposed based on ILREUM data are presented using thick black lines. Since ILREUM results follow closely the functions described by

Wyngaard et al. (1971), these were selected as appropriate. Please note that the function proposed by Wyngaard et al. (1971) is invisible due to overlap. A summary of the different empirical fits explored and plotted in Figure A1.3 is presented in Table A1.2.

Table A1.2. Empirical fits for $\varphi_\varepsilon(\zeta)$ explored and plotted in Figure A1.11.

Unstable stratification			
Empirical fit		**Source**	**Comments**
$\varphi_\varepsilon(\zeta) = \left(1 + 0.5|\zeta|^{2/3}\right)^{3/2}$	$(-2 < \zeta < 0;\ \kappa$=0.35)	Wyngaard et al. (1971)	Rural
$\varphi_\varepsilon(\zeta) = (1 - 10.5\zeta)^{-1} - \zeta$	$(-3 < \zeta < 0)$	Kanda et al. (2002)	Urban
$\varphi_\varepsilon(\zeta) = (1 - 3\zeta)^{-1} - \zeta$	$(\zeta < 0)$	Thiermann (1990). Thiermann and Grassl (1992) and SCINTEC AG (2006)	Function used in SLS algorithm. Determined using tower data.
$\varphi_\varepsilon(\zeta) = (0.93 - 5.4\zeta)^{-1.1} - 2\zeta$	$(-2 < \zeta \leq -0.001)$	Roth et al. (2006)	Urban
$\varphi_\varepsilon(\zeta) = \left(1 + 0.5|\zeta|^{2/3}\right)^{3/2}$	$(-0.4 < \zeta < 0)$	Proposed	
$\varphi_\varepsilon(\zeta) = (1 - 7\zeta)^{-1} + 4.5\zeta - 4.5\zeta^2$	$(-0.4 < \zeta < 0)$	Proposed	Without CS1-2008
Stable stratification			
Empirical fit		**Source**	**Comments**
$\varphi_\varepsilon(\zeta) = (1 + 4\zeta + 16\zeta^2)^{1/2}$	$(\zeta > 0)$	Thiermann and Grassl (1992) and SCINTEC AG (2006)	Function used in SLS algorithm
$\varphi_\varepsilon(\zeta) = (1 + 6\zeta - 4\zeta^2)^{1/2}$	$(0 < \zeta \leq 0.4)$	Proposed	
$\varphi_\varepsilon(\zeta) = (1 + 5.5\zeta - 4\zeta^2)^{1/2}$	$(0 < \zeta \leq 0.4)$	Proposed	Without CS1-2008

Figure A1.11 shows general agreement between the values derived from ILREUM data and the fits described in the literature. Nevertheless, their impact on SLS data was minimal.